Applications and Implications of Rhenium-Osmium Isotopic Systematics and Highly Siderophile Elements Abundances in Crude Oils and the Younger Dryas Sediments

by

Nan Sun

A dissertation submitted to the Department of Earth and Atmospheric Sciences

College of Natural Sciences and Mathematics

in partial fulfillment of the requirements for the degree

Doctor of Philosophy

in Geology

Chair of Committee: Alan Brandon

Committee Member: Qi Fu

Committee Member: Yongjun Gao

Committee Member: Steven Forman

University of Houston

May 2021

Dedication

This dissertation is dedicated to my late Father

Jin Sun

孙 进

Acknowledgements

First, I would like to express the deep and sincere gratitude to my advisor, Dr. Alan Brandon for his continuous support and encouragement through my Ph.D. research. From teaching me the analytical skillsets to work in a lab, to writing scientific papers, to presenting at conferences, most importantly, to critically thinking as a scientist, the whole journey has shaped me to become a better researcher. I will always remember the famous quote “Be one with the Beam!” and be motivated by his passion and dedication to science.

In addition, I would also like to thank the committee members, Dr. Qi Fu, Dr. Gao Yongjun and Dr. Steven Forman. Dr. Fu has graciously shared his laboratory with me to conduct the experiments and been providing persistent guidance in trouble-shooting obstacles in lab work and valuable advice on research. Many thanks to Dr. Gao for his detailed instruction and support in measuring half of the data in this dissertation. Dr. Forman, who is also a collaborator on two projects from my Ph.D. who has contributed many insightful perspective and discussion, thank you for the deep involvement in my research. I would also like the thank the other two collaborators, Dr. Mike Waters and Dr. Kenny Befus for providing data, samples, ideas and massive support to the work.

Last but not the least, I would like to thank my husband, Jiachao Liu, of whom I am very proud, for his constant support and encouragement to achieve my goals and pursue my career. My dearest mother, brother and late father, who have given me unconditional love and support along the way, without whom I could have never arrived at this exciting point of my life and for whom I am forever grateful.

Abstract

The Re-Os isotopic system is a powerful geochronological and tracing method due to their distinct characteristics in different components of the Earth. The Earth's mantle and extraterrestrial materials broadly to have a near-chondritic $^{187}Os/^{188}Os$ ratio of 0.12, whereas that of the Earth's crust increases to > 1. This large difference has enabled the Re-Os isotope system to be applied to igneous and metamorphic rocks, and also organic-rich sedimentary rocks and petroleum products. Highly siderophile element (HSE) abundances due to their affinity to metals relative to silicates are enriched in the core and chondrites relative to silicate Earth. The Earth's crust has < 0.1 % of HSE abundances compared to extraterrestrial bodies which makes HSE sensitive indicators of a meteoritic contribution delivered in terrestrial settings. Thus, this study has investigated the application of Re-Os isotope system and HSE abundances in two different systems, a petroleum system from Tarim Basin, China and the Younger Dryas sediments from Texas, USA. The two study subjects utilize similar analytical means to constrain the timing of oil generation or alteration in the evolution of Tarim Basin and to trace the origin of the geochemical anomalies at Younger Dryas cooling period.

This dissertation firstly presents Re and Os isotope data from whole oils and asphaltene fractions of a suite of crude oil samples from Tarim Basin. An Early Permian age 286.74 ± 2.34 Ma with mean square of weighted deviates (MSWD) = 2000 six oils is consistent with Tarim Flood Basalt age of 291 ± 4 and 272 ± 2 Ma from U–Pb zircon dating. This study indicates that using Re-Os isotope system, the timing and signature of hydrothermal intrusion into Tarim Basin have been recorded. In the second and third chapters, newly discovered $^{187}Os/^{188}Os$ ratios and HSE abundances from Hall's Cave, and the Debra L. Friedkin sites, Texas are reported. Between the

two sites, unradiogenic Os peaks are identified above, at, and below the Younger Dryas boundary layer. In addition, the HSE abundances at both study sites resemble volcanic gas aerosols instead of previously confirmed impactites. Thus, distant and episodic volcanic eruptions are plausible mechanisms for the geochemical anomalies.

Table of Contents

List of Tables

List of Figures

Introduction

The Re and Os isotopic system has been widely used in the planetary research to determining crystallization ages of early solar system asteroids and the formation of iron meteorites (Luck et al., 1980; Luck and Turekian, 1983; Horan et al., 1992; Smoliar et al., 1996; Shen et al., 1996; Brandon et al., 2000). Rhenium and Os are highly siderophile elements that preferentially enter the liquid iron core during early differentiation (Hart and Ravizza, 1996; Pearson et al., 2004; Reisberg et al., 2004), making them a powerful system in dating and understanding geological processes such as core-mantle formation and ore genesis (Hirt et al., 1963; Foster et al., 1996; Markey et al., 1998; Stein et al., 2001; Morelli et al., 2010). Another geochemical attribute is that Re is a moderately incompatible element whereas Os is highly compatible and partitions into melts sparsely (White, 2007). Therefore, during mantle melting, Re is partitioned into melts and subsequently enriched in the crust, whereas Os is prone to remain in the solid mantle phase. This results in distinctly different Re and Os concentrations in the crust and mantle. Specifically, the crust has a much higher average Re/Os ratio ~ 6 than the value of the mantle which is ~ 0.08 (Morgan, 1986; Esser and Turekian, 1993; Pearson et al., 1995; Meisel et al., 1996; Park et al., 2012). As radioactive isotope ^{187}Re decays to ^{187}Os with a half-life of 423 billion years (Linder, l989), the crust which has relative Re enrichment to Os, produces a higher ^{187}Os/^{188}Os ratios of > 1 compared to that of the mantle, ~ 0.12 (Allègre and Luck, 1980; Esser and Turekian, 1993).

In recent years, the application of Re and Os system has extended to organic-rich sedimentary rocks and petroleum systems (Selby and Creaser, 2005; Selby et al., 2007; Rooney et al., 2012; Cumming et al., 2012; Lillis and Selby, 2013; Georgiev et al., 2016). Rhenium and

Os are organophilic elements and sensitive to redox conditions during the deposition of the sedimentary rocks (Colodner et al., 1993; Levasseur et al., 1998; Poirier, 2006; Yamashita et al., 2007; Sai et al., 2020). Organic-rich sediments is an important crustal reservoir of Re and Os with concentrations of up to ~450 ppb of Re and ~30 ppb of Os (Cohen et al., 1999; Cohen et al. 2004). This is more than two orders of magnitude higher than average continental crust for Re ~198 ppt and for Os ~31 ppt (Esser and Turekian, 1993; Park et al., 2012). The origin of Re and Os in petroleum materials is can be traced back to their source rock systematics and/or the formation water which has direct contact with the system (Rooney et al., 2012; Cumming et al., 2012; Mahdaoui et al., 2015). Hydrous pyrolysis experiments show that organic rich sedimentary rocks release Re and Os to the generated oil during thermal maturation (Rooney et al., 2012; Cumming et al., 2014). Subsequently, the produced oil inherits the Os isotopic signatures of the source rock. To investigate the impact of basin fluids on the Re and Os composition within the oil, researchers have conducted oil-water contact experiments (Mahdaoui et al., 2015; Hurtig et al., 2019). Mahdaoui et al. (2015) have found that under different temperatures, Re and Os are transferred from water in variable mounts to oil and possibly the formation water could be a main source for the Re and Os in the crude oil (Mahdaoui et al., 2015). Hurting et al. (2019) found that the oil-water interaction could reset the crude oils with low ASPH contents and petroleum systems with low water to oil ratios limits the potential for resetting the Re-Os geochronometer due to the kinetic barrier for Re transfer at such water-oil interfaces (Hurtig et al., 2019). However, the primary Re-Os isochron age can be recorded in the crude oil fractions, with initial Os isotopic ratios changing with respect to the water composition (Hurtig et al., 2019).

The residence of Re and Os in crude oils are found to be within the insoluble asphaltene fraction > 90% as opposed to solution maltene fractions (Selby et al., 2007). As a result, the Re-Os isotope compositions are mostly dominated by the asphaltene fraction in whole oil. Thus, in recent years, asphaltene has become an important candidate to whole crude oils to obtain the Re-Os isotopic ratios (Selby et al., 2007; Georgiev et al., 2016; Liu and Selby, 2018; Hurtig et al., 2019). The Re-Os isotope system in crude oils has been applied to petroleum systems worldwide (Finlay et al., 2010; Lillis and Selby, 2013; Cumming et al., 2014; Mahdaoui et al., 2015; Georgiev et al., 2020). The results have been used to make constraints on oil generation, migration, and/or secondary alteration to petroleum systems. In Chapter 1 of this dissertation, I applied asphaltene and whole oil Re-Os extraction technique to crude oil samples from Tarim Basin, China. The research is aimed at tracing the origin of the Os isotopic ratios in the crude oils carrying mantle-derived signature and exploring its link to hydrothermal activity near Tarim Basin.

As discussed above, the Re-Os isotopic system behaves differently in crustal and mantle materials, resulting in an average $^{187}Os/^{188}Os$ ratio of the crust of ~1 and that of the mantle is near chondritic, ~0.12 (Allègre and Luck, 1980; Esser and Turekian, 1993). This difference in $^{187}Os/^{188}Os$ ratios has made Os isotopes a sensitive indicator for investigating whether the crustal materials have been mixed with mantle or extraterrestrial components. However, depending solely on $^{187}Os/^{188}Os$ ratios, the origin for the unradiogenic Os cannot be pinpointed to the right source. Thus, HSE (Os, Ir, Ru, Pt, Pd, Re) are usually combined with $^{187}Os/^{188}Os$ ratios in exploring the trigger mechanisms for the unradiogenic $^{187}Os/^{188}Os$ in terrestrial materials (Tagle and Hecht, 2006). The HSE are transition elements in the periodic table and have an affinity for metals relative to silicates. In the process of core formation, ~99.8% of the terrestrial HSE budget (Puchtel, 2016)

was sequestered into the core. Theories on HSE abundances in the silicate Earth are best explained by addition of 0.3–0.8 % of chondritic materials to Earth after the core formation via late accretion (Chou et al., 1983; Morgan et al., 1985; Morgan et al., 1986). The level of HSE in the Earth's mantle is less than 1% of the CI-chondritic abundances, and that in the crust up to several orders of magnitude less (Park et al., 2012). This makes HSE a power method for studying extraterrestrial input in impact materials associated with terrestrial craters, as less than 1% of such material is needed to provide a HSE and $^{187}Os/^{188}Os$ signature of impact-signal in terrestrial settings (Palme, 2008).

The Younger Dryas (YD) event occurred from 12.9 to 11.7 ka (Firestone et al., 2007; Kennett et al., 2009a; 2009b) in North America and Europe is marked by abrupt climate cooling contemporaneous with extinctions of Pleistocene megafauna and demise of the Clovis culture (Firestone et al., 2007; Kennett et al., 2009a; 2009b; Wittke et al., 2013). There are two prevailing mechanisms. One is that massive freshwater discharge into the North Atlantic reducing the formation of deep waters and weakening or shutting down of the meridional overturning circulation (Broecker et al., 1985; McManus et al., 2004; Tarasov and Peltier, 2005; Carlson et al., 2007; Wang et al., 2018; Cheng et al., 2020). The second mechanism involves global cooling triggered by one or more bolide impacts or airbursts (Firestone et al., 2007; Kennett et al., 2009a; Wittke et al., 2013). Observed markers that have been used to support the impact origin of the YD event include elevated concentrations of carbon spherules, magnetic grains and spherules, nanodiamonds, and Ir (Firestone et al., 2007; Kennett et al., 2009b; Wittke et al., 2013; Kinzie et al., 2014; Israde-Alcantara et al., 2012; Kinzie et al., 2014). Where found, the suite of impact-related proxies approximately reach peak abundances near or at YD basal boundary layer (YDB). However, reproducibility and viability of such magnetic grains,

spherules, nanodiamonds and Ir enrichments has been questioned and unable to be achieved by other independent research groups (Surovell et al., 2009; Paquay et al., 2009; Daulton et al., 2010). Paquay et al. (2009) reported at least one order of magnitude lower Ir abundances in combination with HSE chondrite-normalized abundance patterns overlapping average continental crust, when compared to Ir abundances found at the same YD sites (Firestone et al., 2007; Paquay et al., 2009). In the second and third chapters of this dissertation, the integrated HSE and $^{187}Os/^{188}Os$ systematics are applied to two well-dated sediment sequences from YD sites in Texas, with the goal of tracing the origins for the sudden climate change that occurred at ~ 12.9 ka.

This dissertation consists of this introductory chapter, three main chapters which will be presented in the format of individual papers (which have been published, or currently in review), and a conclusion chapter. The aim of the main chapters presented here is to demonstrate and expand the utility of the Re-Os isotopic system in crude oils and sediments. In addition, the coupled application of Re-Os and HSE is adopted as a powerful tool in providing support or opposition to the impact hypothesis. This dissertation is presented in the format of scientific papers with three main research chapters written as distinct papers.

Chapter 1. Re-Os Geochronology and Fingerprinting in Heavy Crude Oils from Tarim Basin, China

1.1 Introduction

Rhenium and Os have been found to be enriched in organic-rich sedimentary rocks in comparison to upper continental crust which has average concentrations of 198 parts per billion (ppb) of Re and 31 parts per trillion (ppt) of Os (Esser and Turekian, 1993; Park et al., 2012). The concentrations of Re and Os in petroleum can be typically more than 1 ppb of Re and more than 30 ppt of Os (Barre et al., 1995; Selby et al., 2007). Thus, the application of the Re-Os radiometric system has also been extended to crude oils and different types of kerogens to provide the timing constraints for petroleum events, such as oil generation, migration, thermochemical sulphate reduction (TSR) (Selby, 2005; Selby et al., 2007; Finlay et al., 2010; Rooney et al., 2012; Lillis and Selby, 2013; Cumming et al., 2014).

1.1.1 The Re-Os elemental and isotopic systematics in crude oil

The residence of Re and Os within different fractions of crude oil was first examined by Selby et al. (2007). They separated 17 crude oils into soluble maltene and insoluble asphaltene fractions using n-heptane as the precipitating agent. More than 83% of the whole oil Re and Os reside in the asphaltene fraction, and their abundances scale with the asphaltene content in the oil (Selby et al., 2007). However, of what form Re and Os are in crude oils is still unknown. It has been suggested one of the possibilities is multiple bonding functional groups, for example, metalloporphyrin complexes and heteroatomic ligands (Selby et al., 2007). In addition, Re and

Os are more likely to be bonded to polar compounds as shown by progressive asphaltene sub-fractions precipitation (Mahdaoui et al., 2013; DiMarzio et al., 2018).

Even though how and where Re and Os are located in crude oils is still not well understood, their contents in crude oils primarily reside in asphaltene and this has been experimentally validated (Selby et al., 2007; Georgiev et al., 2016). Approximately > 90% of Re and Os in crude oils are found to be present in the insoluble asphaltene fraction as opposed to solution maltene fraction (Selby et al., 2007). Thus, asphaltene has become an important candidate in Re-Os geochronology and fingerprinting analyses for petroleum systems. In recent years, subsequent relevant work has been focused on providing Re-Os ages in asphaltene fractions (Finlay et al., 2011; Lillis and Selby, 2013; Cumming et al., 2014). Precise Re-Os isochron ages have been successfully obtained for some petroleum systems, corresponding to the timing of oil generation and alteration, and confirmed by basin models ages or Ar-Ar geochronology (Selby, 2005; Finlay et al., 2011; Rooney et al., 2012; Cumming et al., 2014).

1.1.2 The application of Re-Os geochronometer to petroleum systems

1.1.2.1 Timing of source rock deposition

The Re-Os geochronometer in organic-rich sedimentary rocks such as black shale has long been proven to be a powerful dating method for petroleum systems, such as source rock deposition, oil generation, migration and secondary alteration events. This method was developed by Ravizza and Turekian (1989) and later evaluated by Ravizza et al., (1991) and Cohen et al., (1999). In later years, subsequent works have successfully constrained the deposition ages of organic-rich sedimentary rocks (Cohen et al., 1999; Selby and Creaser, 2005;

Selby, 2005; Kendall et al., 2009; Xu et al., 2009; Rooney et al., 2010, 2012). One early successful study to obtain a Re-Os isochron age in sedimentary rocks was achieved by Creaser et al. (2002). A Re–Os isochron age of 358 ±10 Ma was obtained representing the timing of deposition of the Late Devonian Exshaw Formation in the subsurface of the Western Canada Sedimentary Basin, Alberta. This Re-Os isochron age is within uncertainty of the established absolute age for the Exshaw Formation. Another noteworthy outcome from the study done by Creaser et al. (2002) is that hydrocarbon maturation has no significant influence on the Re-Os system in the Exshaw Formation rocks. This indicates that Re-Os geochronometer is applicable regardless of the level of hydrocarbon maturation, making it a useful dating method for petroleum source rocks.

1.1.2.2 Timing of oil generation, migration and alteration

The Re-Os geochronometer has a proven success in yielding reasonable ages for petroleum events using whole oils (Selby, 2005; Sen and Peucker-Ehrenbrink, 2014), as well as asphaltene fractions (Finlay et al., 2010; 2011). Compared to traditional fingerprinting techniques (biomarkers), the Re-Os geochronometer has advantages in dating and tracing secondary alteration processes. Successful and precise results Re-Os isochron ages for petroleum materials is dependent having a closed system since the event that is being dated. However, the natural processes crude oils have gone through include generation, expulsion, migration, and alteration. The complexity in process may result in multiple times of Re-Os system resetting and rehomogenization. Incomplete homogenization of Re and Os could lead to ambiguity as to what events an age represents. For example, Lillis and Selby (2013) studied crude oils from the Phosphoria petroleum system, Bighorn Basin, USA, were able to attain two ages, the main trend oils yield a Triassic age

of 23 ± 43 Ma and the Torchlight trend yield a Miocene age of 9.24 ± 0.39 Ma. The Triassic age 239 ± 43 Ma agrees with the expected time of Phosphoria petroleum generation. The Bighorn Basin underwent major uplift and erosion at about 10 Ma. Thus the obtained Miocene age may represent the timing of the end of TSR caused by reservoir cooling from uplift and erosion.

Secondary alteration processes have different effects on the Re-Os isotopic systematics and geochronology within petroleum samples (Liu, 2017). One advantage of Re-Os dating to traditional biomarker analysis is the ability of staying intact during biodegradation. Aforementioned studies showed different degrees of biodegradation have little effect on Re and Os isotopic systematics (Selby and Creaser, 2005; Selby et al., 2007; Finlay et al., 2011; Lillis and Selby, 2013). When light fractions of hydrocarbons are removed by biodegradation, the Re-Os isotope system is little affected (Selby, 2005; Finlay et al., 2010). Biodegradation preferentially removes the light fractions of crude oil leaving the main carrier of Re and Os, the asphaltene fraction almost intact.

Additionally, Lillis and Selby (2013) found that the TSR event could be recorded by the Re-Os clock and cause the Re-Os correlations to exhibit large data scatter with consequent greater on the age uncertainty and regression MSWD. A Late Triassic age of 211 ± 21 Ma for the main trend oils in the Phosphoria petroleum system when excluding those that have been effected by TSR. It was considered to represent the early stage of oil generation. (Lillis and Selby, 2013). The data scatter of the Re-Os isochron generated for all of the main trend oils was considerably large, having a MSWD of 1596. Lillis and Selby (2013) suggested that the TSR has induced the resetting of Re and Os, which was the reason for the resultant data scatter.

Other Re-Os isotope work on low maturity bitumen and pyrobitumen from the western margin of Xuefeng uplift, southern China, yields an age of 429 ± 140 Ma. This was interpreted as representing the initial crude oil generation age and another age of 69 ± 24 Ma was considered to be the end of gas and pyrobitumen generation, respectively (Ge et al., 2016). Hence, it shows that both TSR and thermal intrusion could have reset the Re-Os isotope systematics of hydrocarbons.

1.1.2.3 Oil-to-source fingerprinting using Os isotope compositions

In addition to determining the timing of petroleum events, Re-Os isotopes have also been applied as a fingerprinting technique for determining the source of petroleum. Oil to source rock correlations are commonly approached by the usage of biomarkers. However, secondary alteration is able to destroy light hydrocarbons from petroleum such as biodegradation, water-washing, or thermal maturity (Selby, 2005; Atwah et al., 2019). Therefore, if solely relying on organic biomarkers, the availability and accuracy issue should be taken into consideration. On the other hand, Re–Os geochronology and Os isotope fingerprinting in petroleum, utilizes the biodegradation-resistant asphaltene fraction of oil (Selby et al., 2007; Cumming et al., 2014). The Os isotope fingerprinting system takes advantage of the initial $^{187}Os/^{188}Os$ composition of organic-rich sediments, which reflects the source rock at the time of petroleum generation and thus provides an alternative inorganic oil-source correlation method (Selby et al., 2007; Finlay et al., 2011).

Cumming et al. (2014) performed Re-Os analysis on samples from the Green River Formation of the Uinta Basin in northwest Utah. Hydrous pyrolysis experiments on the source rock samples indicated that the transfer of Re and Os from source to oil resemble the natural system. This transfer of Re and Os from source to bitumen to oil did not affect source rock Re–Os isotope systematics. This is consistent with the transfer of $^{187}Os/^{188}Os$ ratios without change from source

to petroleum during petroleum generation (Rooney et al., 2012). Hence, petroleum $^{187}Os/^{188}Os$ ratios can be used as a source correlation tool. In addition, these experiments further confirm that Re–Os isotope systematics in source rocks are not adversely affected by petroleum maturation.

1.1.3 Basin fluid interaction effect on crude oil Re and Os system

By thermal maturation of organic-rich sedimentary rocks, Re and Os are transferred from source rocks to crude oils. Formation waters and crude oils usually coexist in petroleum reservoirs, therefore oil-water interaction could influence Re and Os within oils. Contact experiments between natural oils and aqueous solutions show that Re and Os are transferred massively and very quickly from the aqueous solution to the organic phases regardless of temperature or oil composition (Mahdaoui et al., 2015). For a given basin, the formation waters may have homogenized Os isotopic composition and Re/Os ratios. Moreover the water might flow through the reservoir and interact with different phrases then develop different Re and Os characteristics, which end up resetting the Re-Os geochronometer (Mahdaoui et al., 2015). Based on the calculation of the study, basin fluids could be the main source for the Re and Os in crude oils (Mahdaoui et al., 2015). However, this conclusion later was challenged (Wu et al., 2016), as the Re and Os concentrations of basin fluids are typically 4 ppt Re and 70 ppt Os, respectively (Mahdaoui et al., 2015). These concentrations are much lower than those applied in the experiments of Mahdaoui et al., (2015), that were 1 ppb-100 ppm of Re and 1 ppb and 10 ppb of Os. Hurting et al. (2019) have conducted a series of equilibration experiments between different oils and dilute aqueous solutions doped with Re and Os. This study found that the oil-water interaction could reset the Re-Os geochronometer for crude oils with low ASPH contents and systems even with 0.03water to oil ratios. Despite of interference of basin fluids, the primary Re-

Os isochron age information can be preserved in the maltene and asphaltene fractions (Hurtig et al., 2019). Finlay et al., (2010) tested United Kingdom North Sea oils for Re and Os isotopic compositions. In these results, unradiogenic $^{187}Os/^{188}Os$ ratios of ~0.17 to ~0.48 were suggested to have been contaminated by fault-induced mantle fluids. The Re-Os isotope systematics of the oil failed to yield a generation age, but instead traced the crustal scale fluid dynamics and migration.

1.1.4 Research Motivation

There has been continuous and successful application of the Re and Os isotope system to determine the timing of hydrocarbons generation, migration, thermochemical sulphate reduction and/or other secondary alteration processes (Selby et al., 2007; Lillis and Selby, 2013; Cumming et al., 2014; Georgiev et al., 2016; Corrick et al., 2019). The research presented in this chapter is aimed at understanding the Re and Os isotopic systematics in dating and tracing hydrothermal fluid intrusion activities for oil samples from Tarim Basin.

1.2 Geological Setting

The Tarim Basin is located in northwest China. It covers an area of about 560,000 km^2, and is the biggest inland basin in China (Wang et al., 1992; Sun et al., 2008). It is a Paleozoic cratonic basin, overlain in the south and north by a Mesozoic–Cenozoic foreland depressions (Li et al., 1996). The Tarim Basin has several structural units, from north to south. They are the Kuqa Depression, Tabei Uplift, North Depression, Tazhong Uplift, Southwest Depression, Tanan Uplift and Southeast Depression (Figure 1.1). The stratigraphy of the Tarim Basin consists of marine carbonate rocks, shale, and mudstone, continental lacustrine mudstone, shale, and oil

shale and transitional marine and continental mudstone sequences (Figure 1.2) (Lee, 1985). Cambrian–Lower Ordovician strata were deposited in shallow marine to lagoonal environments under reducing conditions throughout the cratonic basin. Middle–Upper Ordovician strata that includes argillaceous limestones and marlstones formed shelf edge and slope environments during a marine transgression (Zhu et al., 2012; Zhan et al., 2016).

The Tabei Uplift is located in between of the Kuqa and North Depressions. It is a northeast trending structural high developed on the pre-Sinian metamorphic basement (Zhu et al., 2012; 2013; Zhan et al., 2016). The Tabei Uplift is composed of an early Paleozoic–early Mesozoic paleo-anticline, and Mesozoic–Cenozoic monoclines that are northward-dipping. The Tazhong Uplift is an early Paleozoic–later Mesozoic uplift (Chen et al., 2000; Liu et al., 2012). The majority of samples in this study are Ordovician or Triassic oils found within the Tabei Uplift. One oil was sampled from a Mid-Cambrian formation in the Tazhong Uplift (Figure 1.2).

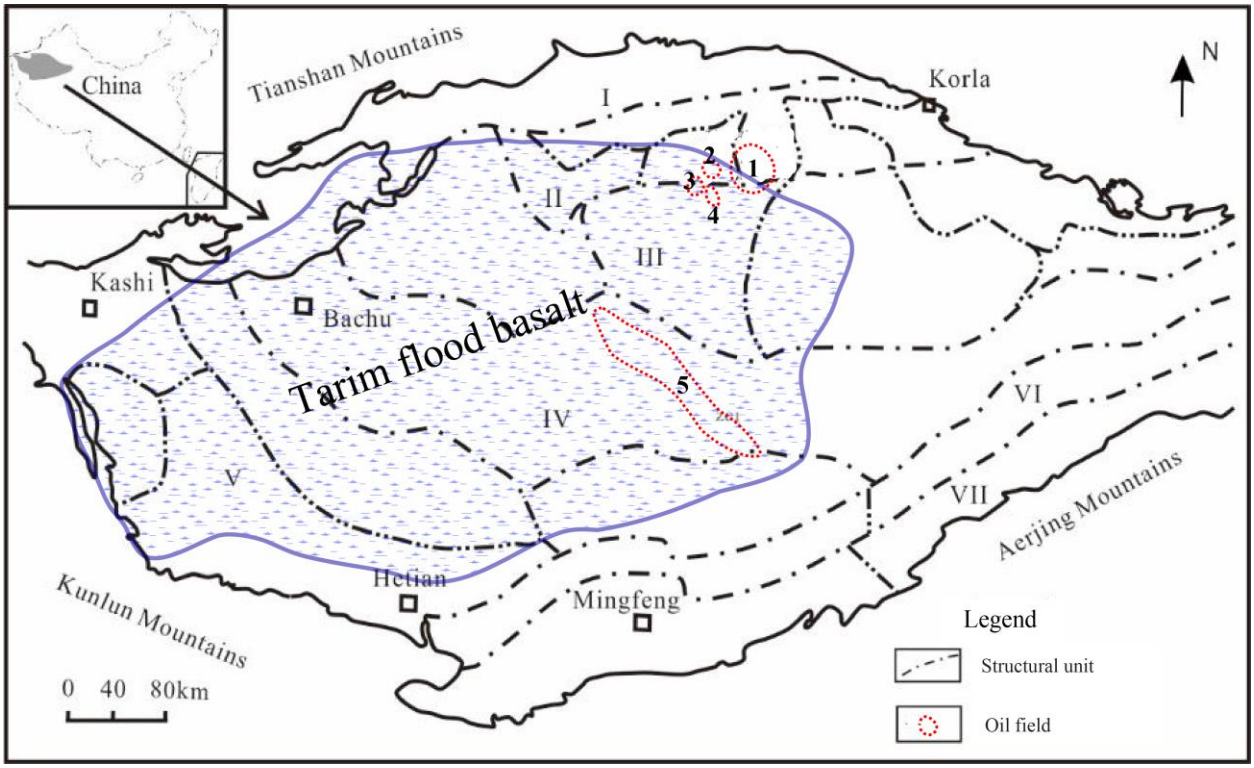

Figure 1.1 Map of Tarim Basin showing tectonic units and locations of sampled oil fields. Purple pattern illustrates the estimated area of the Tarim flood basalt. Structural units are: I. Kuqa Depression, II. Tabei Uplift, III. North Depression, IV. Tazhong Uplift, V. Southwest Depression, VI. Tanan Uplift, VII. Southeast Depression. Oil fields are: 1. Tahe Oil field, 2. Halahatang Oil Field 3. Xincheng Oil Field, 4. Hadexun Oil Field, 5. Tazhong Oil Field (modified after Liu et al., 2008 and Chen et al., 2014)

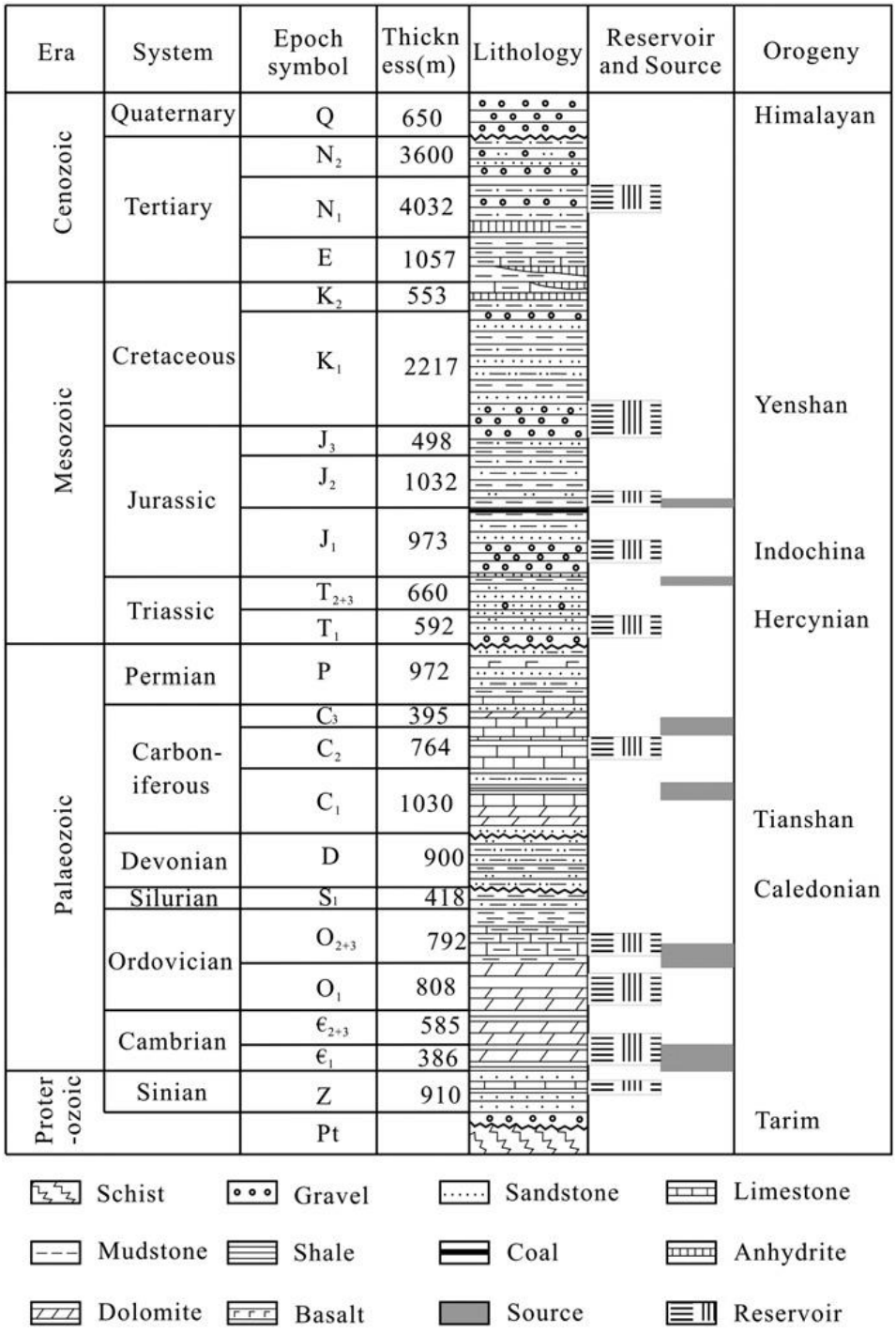

Figure 1.2 The stratigraphic column and locations of petroleum systems in the Tarim Basin (After Liu et al., 2012).

1.3 Early Permian Tarim Flood Basalt

In recent years, large volumes of volcanic and intrusive rocks emplaced in the Early Permian have been discovered within the Tarim Basin and surrounding area (Li et al., 2008; Tian et al., 2010; Pirajno et al., 2011; Yu et al., 2011; Xia et al., 2012; Zhang et al., 2014) (Figure 1.1). The extent of this Early Permian magmatism exceeds and area of 250,000 km^2 along northeast to southwest direction at ~280 Ma (Tian et al., 2010; Xu et al., 2014; Wang et al., 2015). Seismological survey shows most of the basalts are buried under a thick post-Permian sedimentary strata (Yang et al., 2007).

The discovery of the Tarim Flood Basalt has profound implications for the petroleum exploration in Tarim oil fields. Intrusive rocks have low permeability and act as barriers to migration flow that then form traps (Schutter, 2003; Cukur et al., 2010; Gao et al., 2017). Sill and dike networks may also intrude into source rocks, reservoir rocks and other petroleum elements and can interrupt hydrocarbon migration and entrapment (Holford et al. 2012; 2013). During recent exploration in the Tarim Basin, Tian et al. (2010) reported an intersected picrite–basalt–rhyolite suite during industrial drilling in the west of the Tarim Basin. The integrated major and trace element compositions, Sr–Nd isotopes, and seismological data show that the extensive Permian magmatism is characterized by rapid eruption flows (~ 5 Ma) with ocean island basalt (OIB)-type chemical compositions. The Tarim Flood Basalt has an initial $^{187}Os/^{188}Os$ of 0.12-7.48 for peridotites and pyroxenites, whereas the black shale of the basal Cambrian from the northern Tarim Basin has initial $^{187}Os/^{188}Os$ of ~1.08 (Yu et al., 2009; Zhang et al., 2014; Chen et al., 2014).

This research is aimed at applying the Re-Os isotope system to crude oil samples from the Tarim Basin with the purpose of dating and fingerprinting hydrothermal activity with the

reservoir, migration pathways, and other petroleum elements. Thus, in this chapter, the Re and Os isotope compositions within whole oils and the asphaltene fractions from northern Tarim Basin have been examined to explore their dating and correlation by applying the Re-Os isotope geochronometer.

1.4 Sample Preparation and Analytical methodology

Fourteen heavy oils from five oil fields from northern Tarim Basin were provided by the China Petroleum & Chemical Corporation. These were measured for Re and Os abundances and $^{187}Os/^{188}Os$ isotope compositions. One to 2 grams of whole oils were used. These were accurately weighed and then filtered with 0.45-micron PTFE filters attached to a plastic syringe which removed any sediments or clay particles. Next, 40 ml of *n*-heptane was added to the filtered oil and sealed centrifuge tubes. These were then placed on an IKA® KS 3000 i Control Incubating Shaker to thoroughly mix the oil and *n*-heptane for 36 hours. These were then transferred to refrigerator and chilled overnight for the purpose of precipitation of asphaltene. Following this step, the samples were centrifuged for 20 min at 3200 RPM. This resulted in insoluble solid asphaltene accumulating on the bottom of the centrifuge tubes. The solutions were decanted gently. The remaining sample precipitates were air dried at room temperature until the remaining liquid solvent was fully evaporated from each.

Approximately 0.01 - 0.5 g of the separated asphaltenes or whole oils were weighed into borosilicate glass Carius tubes. A mixed ^{185}Re - ^{190}Os spike and reverse aqua regia were added to each, following the digestion protocols of Shirey and Walker (l995). The Carius tubes were sealed, and placed in an oven for 48 hours at 240 °C. During the digestion, Re and Os are oxidized to ReO^{3-} and OsO^{4-} species, respectively. Then the tubes were frozen in dry ice–ethanol

slurry, opened, then thawed to room temperature. The equilibrated sample solutions were processed to separate Os using $CHCl_3$ solvent extraction, then HBr back-extraction, followed by purification via microdistillation (Cohen and Waters, l996; Birck et al., 1997). Rhenium is left in the remaining reverse aqua regia solution after Os extraction with $CHCl_3$. The Re-bearing solution were dried down, then redissolved in HCl. The Re in these solutions were purified via anion column chemistry two times. The purified Os was loaded onto ultra-pure (>99.99%) Pt filaments, and coated with $Ba(OH)_2$ as an activator. Osmium isotopic compositions were measured by isotope dilution using negative thermal ionization mass spectrometry (NTIMS) on a ThermoElectron TRITON Plus TIMS at the University of Houston (Creaser et al., 1991; Völkening et al., 1991). Rhenium isotopes, ^{185}Re and ^{187}Re, were analyzed by isotope dilution using an inductively coupled plasma triple quadrupole (Agilent technologies 8800 ICP-QQQ) at the University of Houston. The 1.4 ml sample aliquots were placed in the ICP-QQQ, and ran automatically using a NH_3 carrier gas. Raw Re and Os isotope measurements were corrected for mass fractionation, isobaric oxygen interferences and blank. Average procedural blanks were 8 pg for Re and 756 fg for Os with $^{187}Os/^{188}Os = 0.126 \pm 0.005$ (2σ).

1.5 Results

1.5.1 Re and Os content in asphaltene and whole oil

Asphaltene separation was performed on twelve of the fourteen oils for Tabei and Tazhong Uplifts in Tarim Basin. The other two samples were measured for Re and Os compositions on whole oil. The Re abundances range from 0.03 to 27.6 ppb, and Os abundances range from 5.6 to 503 ppt for all samples (Figure 1.3a and Table 1). Rhenium and Os

concentrations from a different series of oils with different percentages of asphaltene are also plotted as Figure 1.3b (Selby et al., 2007). This shows that when asphaltene fraction is at the low level of concentration within the host oil, ~2 %, the Re and Os abundances are also exceptionally low, being ~0.02 ppb and ~20 ppt, respectively (Figure 1.3b). In this study, whole oil analysis includes ZC1 from Tazhong oil field and YM3 from Halahatang oil field. Samples ZC1 and YM3 have 0.03 to 0.52 ppb of Re and 5.6 to 37.5 ppt of Os, respectively. This is similar to the low asphaltene abundant oils in Selby et al. (2007).

Asphaltene fractions in the Tarim Basin crude oils show significant enrichment of Re and Os relative to whole oils. Twelve asphaltenes have Re from 0.08 to 27.6 ppb and Os from 22 to 503 ppt, respectively. These concentrations are higher than those of whole oils above. In Figure 1.3a, the National Institute of Standards and Technology (NIST) Research Material 8505 crude oil is also plotted (Liu and Selby, 2018). The study used 5 different bottles of NIST 8505 oil and performed multiple duplicates on each bottle. A linear trend with R2 = 0.99 between NIST 8505 oils and asphaltenes is observed for Re versus Os concentrations (Figure 1.3). The elemental abundance sums of every pair of asphaltene and maltene separated from the same oil, weighted by their mass percentage, are indistinguishable from the Re and Os contents of whole oil (Liu and Selby, 2018). This shows no significant Re and Os loss during asphaltene separation. For Tarim whole oils due to experimental limitations, the exact weight percentage of asphaltene in the same whole oil was not determined. There is a lack of distinct correlation between Re and Os abundances for Tarim oils. Given that these oils were sampled in different oil fields and different formations, data scatter is anticipated. Two Tahe oils, TP7 and TK211 and XCH4 from Xincheng oil field, with high Os abundances but relative lower Re abundances are main reason for causing the data scatter. The rest samples seemingly follow a lower left to upper

right trending. The whole sample set could be roughly divided into two groups, one group with increasing Os and Re abundances, the second group has rather unchanged Os abundances against increasing Re abundances.

Table 1.1 Rhenium–osmium elemental and isotope data of asphaltenes and whole oils from Tarim Basin. Uncertainties for Re-Os isotopic data are 2σ.

Sample	Tarim Basin Oil Field	Sample weight (g)	δC13 ‰	$^{187}Re/^{188}Os$	±2σ	$^{187}Os/^{188}Os$	±2σ	Re (ppb)	±2σ	Os (ppt)	±2σ	Depth (m)	Formation
TP7[A]	Tahe Oil Field	0.092	-32.85	2.65	0.021	0.195	0.002	0.274	0.001	502.98	1.97	6519.5-6558.21	O_{2yj}
TK211[A]	Tahe Oil Field	0.310	-33.33	1.14	0.005	1.703	0.007	0.081	0.000	415.42	1.65	5431-5499.4	O_{2yj}
TK101[A]	Tahe Oil Field	0.454	-33.65	130.22	0.865	1.295	0.013	4.065	0.011	173.35	1.04	4556-4559	T_2a
AD26[A]	Tahe Oil Field	0.198		239.13	1.357	3.025	0.017	16.794	0.043	466.33	2.65	6410-6418	O_{1-2yj}
TS3-1[A]	Tahe Oil Field	0.231		111.17	0.660	1.689	0.010	6.272	0.016	327.27	1.63	6234-6333	O_{1-2y}
TH10201[A]	Tahe Oil Field	0.196		118.80	0.703	1.716	0.011	8.172	0.021	400.15	2.04	6046.7-6066.1	O_{2yj}
TH10425[A]	Tahe Oil Field	0.185		151.26	1.981	1.483	0.020	4.449	0.012	166.80	1.35	3027-3166	O_{2yj}
Ha15-1[A]	Hadexun Oil Field	0.226		959.23	10.576	3.697	0.041	27.557	0.071	202.90	1.78	6518	O
Ha701[A]	Hadexun Oil Field	0.223		57.23	4.086	0.534	0.039	0.249	0.001	22.06	0.69	6557-6618	O
QG-1[A]	Halahatang Oil Field	0.528		56.67	0.197	0.671	0.003	5.131	0.013	467.29	1.35	5576-5585	T
XCH4[A]	Xincheng Oil Field	0.012		13.56	0.853	0.203	0.015	1.293	0.004	464.10	13.05	6835-6850	O
XCH9C[A]	Xincheng Oil Field	0.142		41.90	3.967	0.213	0.024	0.215	0.001	25.03	1.05	6757-7011	O
ZC1[W]	Tazhong Oil Field	0.186	-33.37	26.43	8.517	0.158	0.065	0.031	0.000	5.60	0.80	6439-6458	$\in_2$
YM3[W]	Halahatang Oil Field	0.206	-32.90	67.33	3.013	0.132	0.008	0.524	0.001	37.51	0.76	7141-7231	O_{2yj}

[A]Sample measured as in Asphaltene form, [W] Sample measured as in Whole oil.

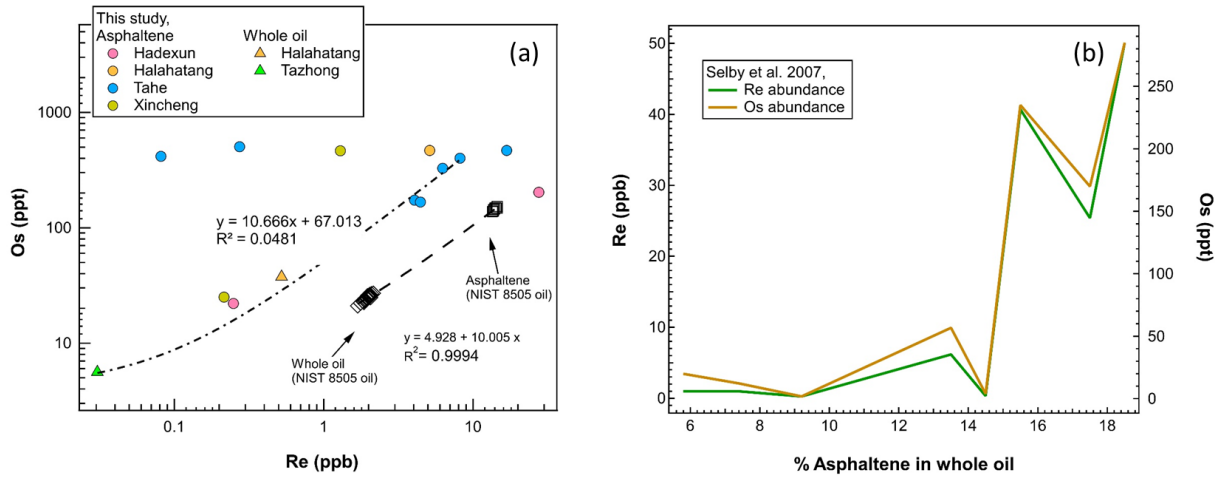

Figure 1.3 Re and Os abundances in asphaltene fraction and whole oil. (a) Tarim Basin crude oils and in comparison to National Institute of Standards and Technology (NIST) Research Material 8505 crude oil (Liu and Selby, 2018), (b) whole oil Re and Os abundances compared to different percentages of asphaltene fraction in the oil samples, data source is from Selby et al., (2007).

For all samples from the Tarim Basin, the $^{187}Re/^{188}Os$ ratio ranges from 1.14 to 959.22, and $^{187}Os/^{188}Os$ is from 0.132 to 3.70 (Table 1.1). Two whole oils show unradiogenic $^{187}Os/^{188}Os$ values of 0.132 and 0.158, respectively. This contrasts to previous oils with very radiogenic values of > 1.27 (Lillis and Selby, 2013; Sen and Peucker-Ehrenbrink, 2014; Georgiev et al., 2016; Liu and Selby, 2018). Three asphaltene samples also have low values of $^{187}Os/^{188}Os$ ratios, 0.19-0.21. One asphaltene from Hadexun oil field and one from Halahatang oil field have slightly higher $^{187}Os/^{188}Os$ ratios of 0.53 and 0.67, respectively. The rest of the asphaltene samples have radiogenic $^{187}Os/^{188}Os$ ratios from 1.29 to 3.70. The most Os radiogenic sample is from Hadexun oil field.

1.5.2 Carbon isotopic compositions of crude oils

The $\delta^{13}C$ data was measured and provided by Dr. Qi Fu at University of Houston. The data were obtained using a Delta V Isotope Ratio Mass Spectrometer (IRMS) from Thermo Scientific, coupled with an elemental analyzer (Costech ECS 4010). Carbon isotope analyses were performed on five oil samples. The samples TP7, TK211 and TK101 are from Tahe Oil Field located at Tabei Uplift. The sample ZC1 is from Tazhong Oil Field and YM3 is from Halahatang Oil Field. Sample ZC1 has $\delta^{13}C$ of -33.37 ‰. Three samples from Tabei uplift have $\delta^{13}C$ values from -33.65 ‰ to -32.85 ‰, consistent with previously reported values, -36 ‰ ~ -31‰ (Jia et al., 2010; Yu et al., 2012). Zhu et al. (2017) reported a large variation ranging from -33.2‰ to -29.8‰ for Paleozoic oils from Tazhong uplift, whereas Tabei uplift oil fields show a narrower range of $\delta^{13}C$, with values of -32.5 ‰ and 30.8 ‰, respectively. Between $\delta^{13}C$ and Re and Os concentrations and $^{187}Re/^{188}Os$ and $^{187}Os/^{188}Os$, no clear pattern can be observed, data points spread in Figure 1.4. The $\delta^{13}C$ variation seems to have no or negligible influence on the distribution of Re and Os isotopic system. However, due to data limitation, the effect of $\delta^{13}C$ values of Re-Os isotopic system will require further investigation.

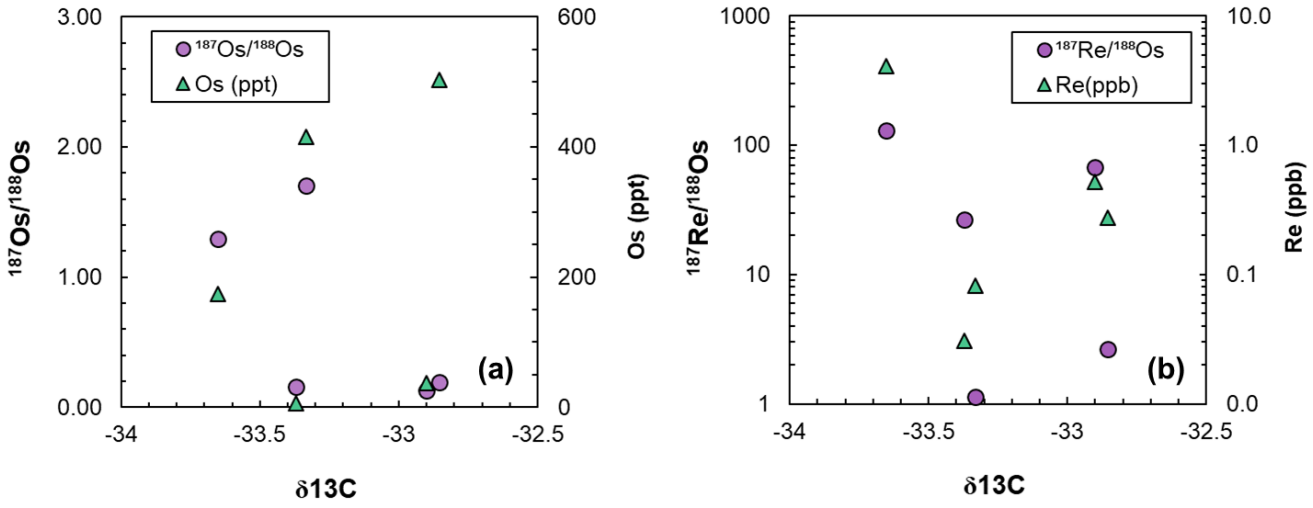

Figure 1.4 The $\delta^{13}C$ values for Tahe, Tazhong and Halahatang Oil Field in Tarim Basin with respect to Re and Os isotopic ratios and concentrations. (a) $\delta^{13}C$ versus $^{187}Os/^{188}Os$ and Os concentration (in ppt), (b) $\delta^{13}C$ versus $^{187}Re/^{188}Os$, and Re concentration (in ppb).

1.5.3 Re and Os concentrations in Tarim oil compared to Tarim Flood Basalt and Lower-Cambrian black shales

The Re and Os isotopic compositions of Tarim Flood Basalt and related rocks, have been presented in two previous studies (Zhang et al., 2014; Chen et al., 2014). Zhang et al. (2014) collected drilled borehole and surface Fe–Ti–V oxide magmatic deposits from west Tazhong Uplift for Re and Os isotope analysis. Their titanomagnetite samples have Re and Os concentrations of 0.19–0.75 ppb and 4–192 ppt, respectively. Chen et al. (2014) sampled mantle xenoliths in Xikeer County, northwest of the Tarim Flood Basalt region. The Re concentrations of the peridotite xenoliths are 0.193-0.871 ppb, whereas Os concentration is much higher than Zhang et al., (2014), ranging from 3195 to 4723 ppt. The Re–Os isotopic systematics of the xenoliths yield an apparent isochron of ~290 Ma, which was concluded to be identical to the timing of eruption of Tarim Flood Basalt (Chen et al., 2014).

Two Re and Os studies of Lower Cambrian black shale drilled from northwest of the North Depression (Figure 1.2) were presented by Yu et al. (2004; 2009). The Re and Os concentrations of the black shales are considered undisturbed in these basin sediments, indicating a typical continental crust source (Peucker-Ehrenbrink and Jahn, 2001). As shown in Figure 1.5, Tarim Basin oils have been plotted against Tarim Flood Basalt samples and Lower Cambrian black shales from northern Tarim Basin with respect to Re and Os total abundances. Most of Tarim oils have intermediate Os concentrations between Lower Cambrian black shales and titanomagnetites and mantle peridotites. The two Re abundances of Tarim asphaltenes are about one order of magnitude lower than the those of Lower Cambrian black shales. The black shales display a Re and Os enrichment compared to titanomagnetites and mantle xenoliths.

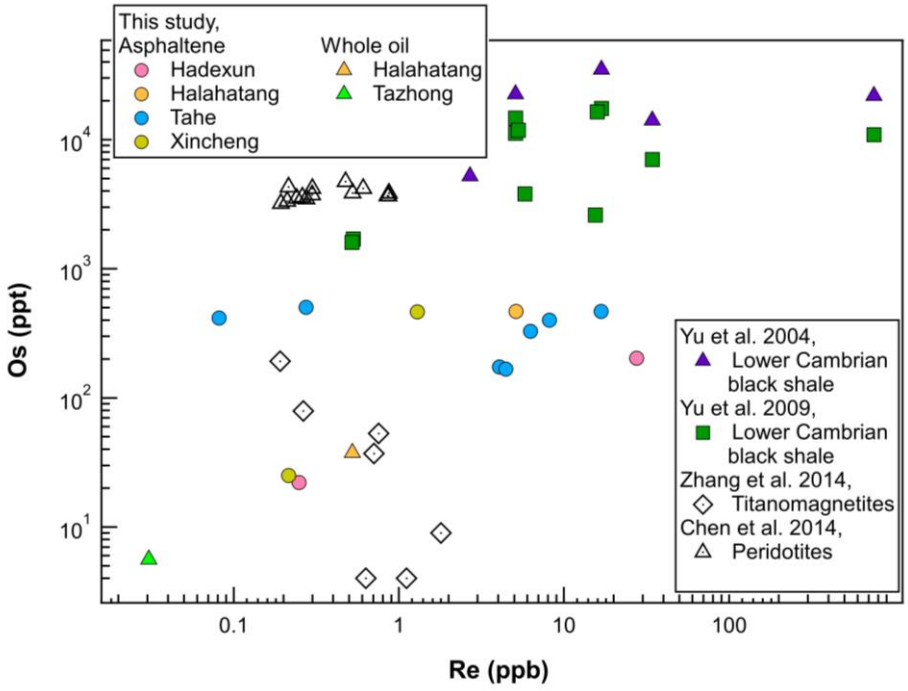

Figure 1.5 Re and Os concentrations in Tarim oil in comparison to Tarim Flood Basalt related rocks, mantle peridotites values are from Chen et al., (2014), Titanomagnetites data are from Zhang et al., (2014) and Lower-Cambrian black shales are from Yu et al., (2004; 2009).

1.6 Discussion

1.6.1 Potential mantle-derived fluid interaction with crude oils

The Re and Os elemental abundances and $^{187}Os/^{188}Os$ values of mantle peridotites are similar to primitive mantle (Becker et al., 2006; Chen et al., 2014). The titanomagnetites have a large range of Re and Os concentrations and present-day $^{187}Os/^{188}Os$ ratios of 0.23-7.5 (Figure 1.6, Zhang et al., 2014). The titanomagnetites were formed during metallogenesis in the Early Permian magmatism. The level of crustal contamination in the titanomagnetites varies by different degrees (Zhang et al., 2014). Samples with high Re and low Os abundances and very radiogenic $^{187}Os/^{188}Os$ most likely experienced assimilation of crustal materials (Walker et al., 1994; Zhang et al., 2008; Zhang et al., 2014). As Figure 1.6 shows there is a good linear regression with $R^2 = 0.9774$ between the mantle peridotites and titanomagnetites between $^{187}Re/^{188}Os$ and $^{187}Os/^{188}Os$. All of the Tarim asphaltene samples, except for TK211, roughly follow the mixing trend between titanomagnetites and mantle peridotites.

The Tarim black shales from lower Cambrian plot as a separate array that extends away from the mixing trend and shows a large range of $^{187}Re/^{188}Os$ from 1.8 to 399, but with a relatively narrow range of $^{187}Os/^{188}Os$ from 1.2-2.7. The reason for the wide range in Re/Os ratios in the Tarim black shales has been suggested to be the result of addition of Os from hydrothermal fluids upwelling from ancient mafic crust (Yu et al., 2004; 2009). The sample TK211 that is far from the cluster of other Tarim oils plots on the low Re/Os side of the Tarim black shales array. To apply regression on all Tarim oils except TK211, a $R^2 = 0.559$ is obtained. The poor correlation indicates that these oils may have been generated at different ages with possibly different initial $^{187}Os/^{188}Os$ values. Additionally Re and Os exchange by external

disturbances is likely to also cause the Re-Os isotopic system to reset. Therefore, the observed $^{187}Re/^{188}Os$ and $^{187}Os/^{188}Os$ values of Tarim oils most likely represent more than one mixing event or process.

1.6.2 Timing of hydrothermal fluid interaction and TSR effect on Re-Os clock

In order to investigate the closure times for Re and Os in the oils, age calculations using IsoplotR (Vermeesch, 2018) were performed using the different subsets of from the Tarim Basin based on the location of oil fields and sampling formations. A Model 1 regression was used for all isochrons presented (York et al., 2004). The 6 oils from Hadexun, Xincheng and Halahatang oil fields yield a scatterchron age of 286.74 ± 2.34 Ma with an initial $^{187}Os/^{188}Os$ of 0.3616 ± 0.0026 and MSWD = 2000 (Figure 1.7a). This Re-Os age is consistent with previous U–Pb zircon ages between 291 ± 4 and 272 ± 2 Ma using rhyolite samples from northern Tabei uplift boreholes (Tian et al., 2010). Previous studies have shown that petroleum charge took place in late Hercynian Orogeny at the end of the Permian (Xiao et al., 2005; Lu et al., 2007; Cai et al., 2009). Thus, the Re-Os age may represent the timing of oil generation. Oils charged in this period may have been newly generated from the upper part of the Cambrian and Early Ordovician source rocks or re-migrated from previously charged oil pools, which may have further went into the Ordovician and Silurian reservoirs (Cai et al., 2009).

The six oils were collected from the Ordovician formation (n = 5) and the Triassic formation (n = 1), at depth of 5576-7231 m. The five Ordovician oils yield a scatterchron age of 227.20 ± 1.86 Ma with a smaller MSWD = 310 and an initial $^{187}Os/^{188}Os$ of 0.0212 ± 0.0050. The mid-Triassic age may represent the post activities after Tarim Flood magmatic activity. The smaller MSWD of 310 implies reduced data scatter. Lillis and Selby (2013) applied Re-Os

analysis to the crude oils from Phosphoria petroleum system, Bighorn basin, USA. They found the main trend yields an age of 39 ± 43 Ma with MSWD of 1596. However, after excluding the oils experienced TSR and a Late Triassic age of 211 ± 21 Ma was obtained with MSWD = 148, which reflects the beginning of Phosphoria oil generation and migration. Involvement of Re-Os data from oils experienced TSR led to high uncertainty of the Re-Os oil generation age and the TSR event itself was also be recorded by the Re-Os clock (Lillis and Selby, 2013).

Previous research shows that for TSR to occur temperature has to be in 100-140°C generally, in some settings it requires temperatures of 160–180°C (Machel, 2001). In Tabei lift area the burial history indicates that the Ordovician reservoirs are deeply buried up to 7000 m corresponding to a reservoir temperature of 160 °C (Figure 1.8, Zhu et al., 2012). Triassic formation is also currently hotter than 110 °C. In Tabei uplift, Ordovician and Triassic reservoirs are approaching the TSR temperature window. Thus, the data scatter in Figure 1.7a are likely caused by TSR. Lillis and Selby (2013) have measure the $\delta^{34}S$ values for the Phosphoria-sourced oils, ranging from - 6.2 ‰ to +5.7 ‰. A large number of Phosphoria-sourced oils from the Bighorn and Wind River Basins that may have been altered by TSR have $\delta^{34}S$ ranging from -7‰ to -2‰ (Orr, 1974). Lillis and Selby (2013) used -2‰ as the break to divided oils into TSR and non-TSR, and improved the $^{187}Re/^{188}Os$ and $^{187}Os/^{188}Os$ regression. Hence, to perform sulfur isotope measurement and evaluate $\delta^{34}S$ values for Tarim Basin oils should be very helpful in identifying the effect and extent of TSR.

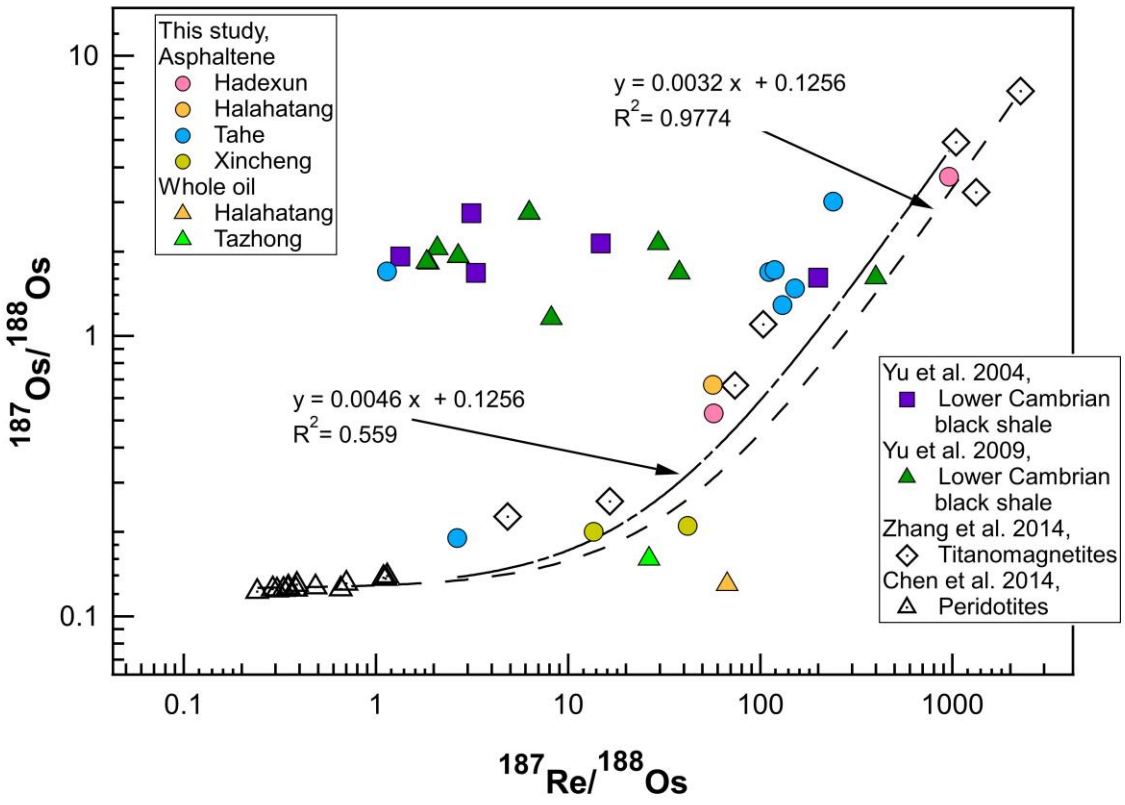

Figure 1.6 $^{187}Re/^{188}Os$ vs. $^{187}Os/^{188}Os$ for Tarim Basin oils. mantle peridotites values are from Chen et al. (2014), Titanomagnetites data are from Zhang et al. (2014) and Lower-Cambrian black shales are from Yu et al. (2004; 2009).

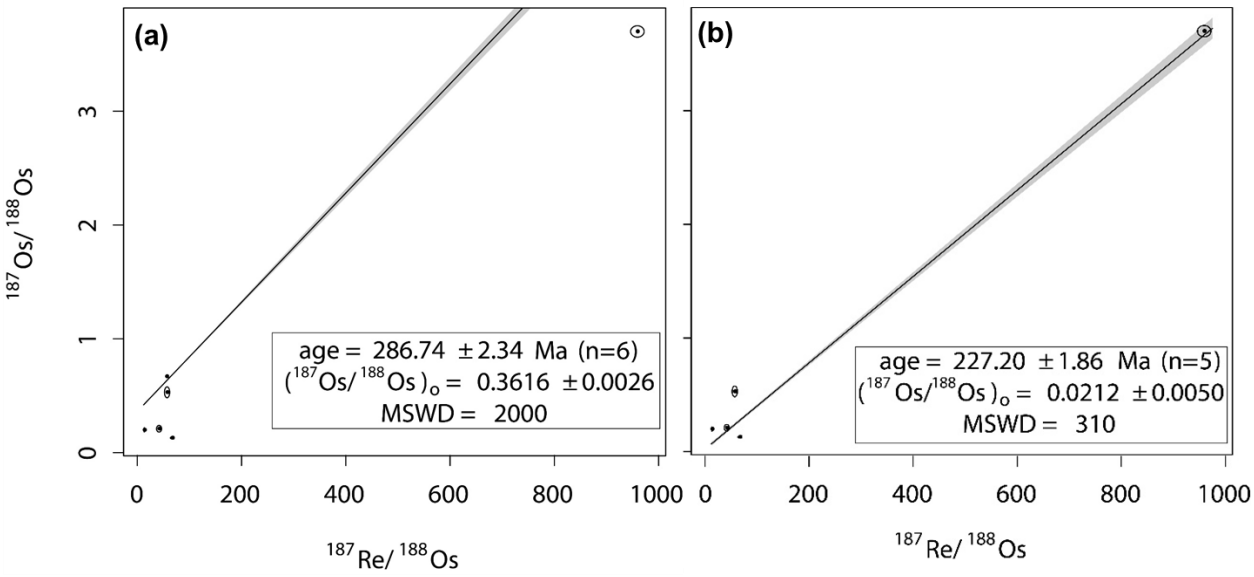

Figure 1.7 Re–Os isotope data of Hadexun, Xincheng, and Halahatang oil fields, (a) $^{187}Re/^{188}Os$ vs. $^{187}Os/^{188}Os$ of 6 crude oils and asphaltenes from the 3 oil fields (b) $^{187}Re/^{188}Os$ vs. $^{187}Os/^{188}Os$ of 6 crude oils and asphaltenes from the 3 oil fields excluding the only oil from Triassic formation, the other five samples are from the Ordovician formation. Regression of the Re-Os data was used online IsoplotR (Vermeesch, 2018).

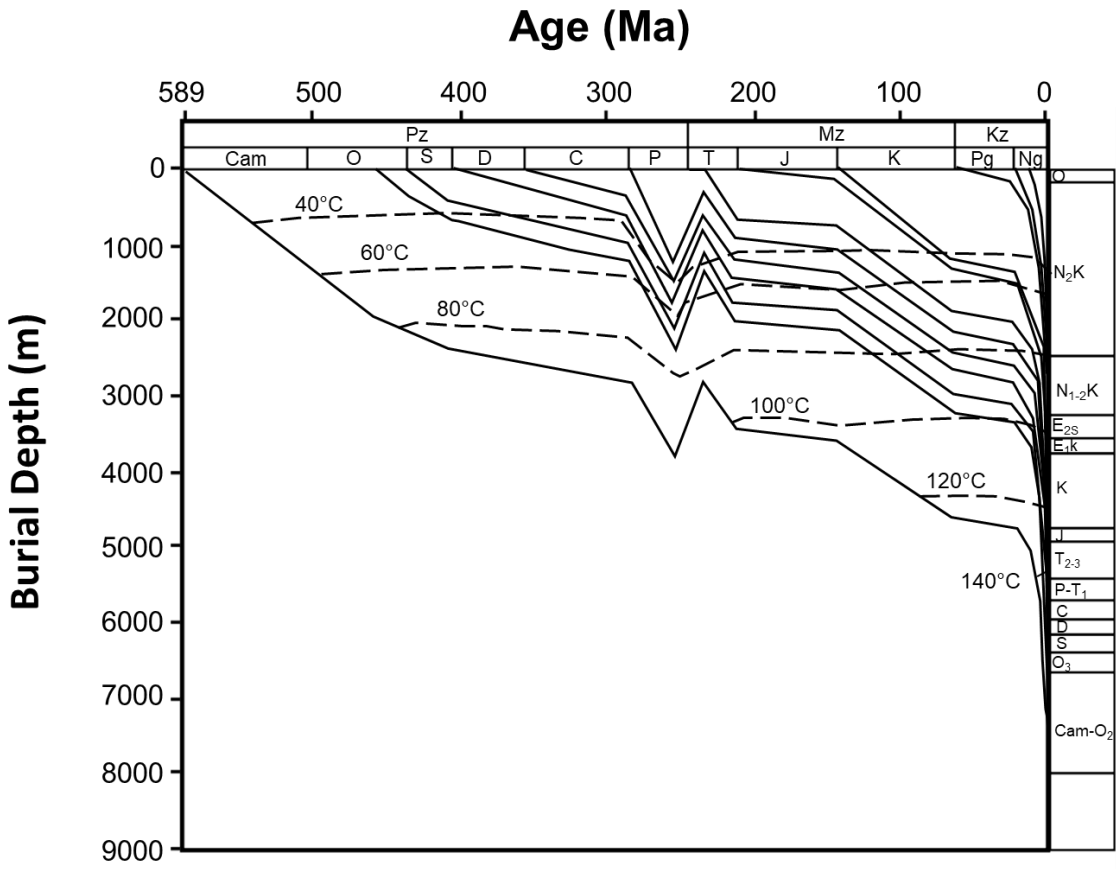

Figure 1.8 Burial history of the Tabei Uplift represented by Well Ha 601-4 in Halahatang Oil Field. Modified after Zhu et al. (2012).

1.7 Conclusions

The Re and Os content in Tarim oils are much more concentrated in asphaltene fractions relative to whole oils. Oil samples from five oils fields in Tarim Basin have a various range of Re and Os elemental abundances and $^{187}Os/^{188}Os$ values. Nine samples have consistent Re and Os elemental abundances and radiogenic $^{187}Os/^{188}Os$ values with previous reported crude oil studies. Five samples display unradiogenic $^{187}Os/^{188}Os$ values < 0.2 that are most likely caused

by mantle-derived hydrothermal fluid interaction with the petroleum reservoirs. In consistent with prior discoveries, the intrusive and extrusive volcanic rocks in Tarim exploration area may have been the result of the large extent magmatism dated early Permian. In addition, an Early Permian age of 286.74 ± 2.34 Ma with MSWD =2000 was yielded by six oils from Tarim Basin. The large scatter of the might be caused by TSR. As the Ordovician and Triassic reservoirs have reached the temperature window of 100-140 °C. A much revised MSWD = 220 with an age of 227.20 ± 1.86 Ma was obtain by a subset of the six oils, which may represent post magma intrusion after the late Hercynian Orogeny.

For its resistance to biodegradation and distinct features between crustal and mantle materials, Re-Os geochronometer has proven to be a valid dating and tracing tool to petroleum systems. Together with $\delta^{34}S$, $\delta^{13}C$, and other analytical techniques, basin modeling, Re-Os systematics could provide unique and powerful analysis and interpretation.

Chapter 2 was previously published in Science Advances as:

Sun, N., Brandon, A. D., Forman, S. L., Waters, M. R., & Befus, K. S. (2020). Volcanic origin for Younger Dryas geochemical anomalies ca. 12,900 cal BP. Science advances, 6(31), eaax8587.

Chapter 2. Volcanic Origin for Younger Dryas Geochemical Anomalies ca. 12,900 CAL BP

2.1 Introduction

The Younger Dryas event, occurred from 12.9 to 11.7 ka in the Northern Hemisphere with abrupt cooling over a time interval of decades with temperatures possibly reaching 15^{o}C colder than present (Severinghaus et al., 1998; Firestone et al., 2007). This cooling part of succession of climate variability in the Late Pleistocene resulted in progressive megafauna extinction (Guthrie, 2006). There are currently four hypotheses for the origins of the YD event. The prevailing hypothesis is cooling and stratification of the North Atlantic Ocean were a consequence of massive ice sheet discharge of meltwater and icebergs and resulted in reduction or cessation of the North Atlantic Conveyor. This is thought to be augmented by climate forcing with expanded snow cover in the Northern Hemisphere (Wang et al., 2018). Another persistent hypothesis is that global cooling was trigged by a bolide impact or airbursts (Firestone et al., 2007). Stratigraphic markers supporting the YD impact hypothesis include elevated concentrations of carbon spherules, magnetic grains, nanodiamonds, and Pt and Ir abundance anomalies (Moore et al., 2019). These markers are found singularly or more at various sites globally and appear to reach peak abundances near or at the YD basal boundary layer. A meteorite crater potentially associated with the YD was recently discovered in Greenland, though not well-dated (Kjær et al., 2018).

A third hypothesis proposes that a supernova explosion in the Vela constellation could have depleted the ozone layer resulting in greater UV exposure and atmospheric and surface

changes that led to cooling (Brakenridge, 2011). Finally, a megaeruption of the Laacher See volcano ejected 6.3 km^3 (dense-rock equivalent, DRE) of zoned sulfur-rich phonolite magma far into the stratosphere at the time of the onset of the YD event (Harms and Schmincke, 2000). Volcanic aerosols and cryptotephra dispersed throughout the Northern Hemisphere over a period of two months and affected the atmospheric optical density for over one year (Graf and Timmreck, 2001). Laacher See released a minimum 2 megatons (Mt) of sulfur (possibly ranging up to 150 Mt), and is suggested to have triggered the sudden lowering of temperature coincident with YD climate change in the Northern Hemisphere (Baldini et al., 2018).

Each of these four possible triggers for the YD event is complex and there is not a clear consensus as to which mechanism or combination of these events initiated the YD cold period. Of these explanations, the impact hypothesis has received the most attention, but problems plague this hypothesis. The fundamental issue is delineating if the markers used to support the hypothesis extracted from the YD layers at various sites are really impact markers (Firestone et al., 2007; Wittke et al., 2013). The grains interpreted as carbon spherules and "elongates" and "glass-like carbon" have been instead identified as fungal sclerotia common in Northern Hemisphere forest litter and soils (Scott et al., 2010). In addition, the micrograins interpreted as hexagonal nanodiamonds from YD sites of Murray Springs (AZ), Arlington Canyon on Santa Rosa Island (CA) are instead assessed as graphene/graphene aggregates (Daulton et al., 2017). These disagreements are compounded by a lack of valid age control at many of the YD boundary layer sites. It is now thought that only three of the twenty-nine sites dated to the onset of YD event were within the prerequisite time period. Further, there are problems in that the reproducibility of observations at the YD level has been questioned for the presence of magnetic grains, spherules, and Ir enrichments. Surovell et al. (2009) failed to duplicate the

magnetic grain or microspherule peaks associated with the YD basal boundary. Thus, there is a lack of consensus on how to interpret the impact markers.

Highly elevated concentrations of Ir together with enrichments of other highly siderophile elements (Os, Ir, Ru, Pt, Pd, Re) in nearly chondritic ratios are considered indicators of a meteoritic contribution delivered when an extraterrestrial (ET) object impacts the Earth or airbursts over it (Alvarez et al., 1980). These HSE enrichments may be from an external source because the Earth's crust has < 0.1 % of CI-chondritic abundances (McDonald et al., 2001). In addition, chondrites have $^{187}Os/^{188}Os$ ratios of around 0.125 (Shirey and Walker, 1998), whereas continental crust has $^{187}Os/^{188}Os$ ratios > 1 (Esser and Turekian, 1993), such that small amounts of ET material added to continental crust will shift the $^{187}Os/^{188}Os$ ratios of the hybridized material to lower values.

The cause of the elevated HSE concentrations and the Os isotopic ratios in YD layer sediments remains equivocal and has been used to both support and negate the YD impact hypothesis. For example, Petaev et al. (2013) found a Pt enrichment accompanied with an extremely high Pt/Ir but Al-poor signature in the Greenland Ice Sheet Project 2 ice core at the Bølling-Allerød/YD transition period, which they interpreted to be consistent with an ET impactor. Also, the elevated Pt abundance anomalies of 100 to 65,600 parts per trillion (ppt) at the onset of the YD in sites from North America is purportedly consistent with the Greenland ice core Pt data (Moore et al., 2017). Moore et al. (2017) found Pt and Pd/Pt anomalies in the YD basal layer in South Carolina. These data are used to support a model of wide-ranged atmospheric input of platinum-rich dust during the YD potentially related to a bolide impact or airburst. In contrast, the $^{187}Os/^{188}Os$ ratios obtained on YD basal boundary layers from widely dispersed locales in North America and Europe have largely been similar to those for continental

crust or seawater with no evidence of unradiogenic $^{187}Os/^{188}Os$ ratios from ET or mantle sources, both having $^{187}Os/^{188}Os$ ratios of 0.11 to 0.13 (Paquay et al., 2009; Wu et al., 2013). This is exceptional because <1% of ET material from an impactor mixed into continental crust would shift the resultant hybridized material away from terrestrial crustal $^{187}Os/^{188}Os$ values towards the less radiogenic values of $^{187}Os/^{188}Os$ chondrites (Shirey and Walker, 1998). Only one site has been identified with an unradiogenic Os signature, with a $^{187}Os/^{188}Os$ ratio of 0.4 for the YD basal boundary layer at Melrose, PA (Wu et al., 2013). This signature is attributed to surface films on glass spherules with highly elevated Os concentrations and unradiogenic $^{187}Os/^{188}Os$ ratios of 0.113 to 0.121 that may have been caused by mobilization of Os within a bolide fireball, and possibly terrestrial in origin and ejected as molten material following impact (Wu et al., 2013). An important question remains: why are low $^{187}Os/^{188}Os$ ratios found only at one site, and not more widely dispersed if it is derived from impact or air burst of a bolide?

The above studies show that there is no clear consensus on the interpretation of HSE concentrations and $^{187}Os/^{188}Os$ compositions of YD basal boundary sediments (Paquay et al., 2009; Wu et al., 2013). A better understanding of their systematics is crucial for determining the role, if any, of a bolide event for the Younger Dryas cooling, and to refine conclusive evidence in the rock record for bolide impacts. To further examine this issue, we measured HSE abundances and $^{187}Os/^{188}Os$ isotope ratios in samples from Hall's Cave, Texas including those from the YD boundary. Hall's Cave formed in the Segovia Formation of the lower Cretaceous Edwards Group and contains sediments dating from 20,000 years BP to present (Toomey, 1993). The cave has a consistent depositional environment with minimal reworking or disturbance over this time period (Toomey, 1993). The stratigraphy is well dated based on 162 accelerator mass spectrometry (AMS) ^{14}C dates from vertebrate fossils, snails, charcoal, and sediment chemical fractions

(Toomey, 1993; Bourne et al., 2016). The YD basal boundary layer at Hall's Cave also contains purported extraterrestrial proxies including nanodiamonds, aciniform soot, and magnetic spherules (Stafford, et al., 2009). Here, we present Os isotopes and HSE abundances from the YD basal boundary strata in addition to layers above and below that horizon. Our measurements span ~4,000 years of sediment deposition at Hall's Cave. The HSE chondrite-normalized patterns combined with $^{187}Os/^{188}Os$ at different levels within this section at Hall's Cave including the YD basal boundary layer, show a repeating record of Os concentration enrichment. Multiple occurrences above and below the anticipated YD basal boundary layer bring into question the single impact theory for the YD climate event. Instead, we propose that the five layers containing HSE enrichments and Os isotopic signatures represent volcanic aerosols and cryptotephra contributed from distant volcanic eruptions over the ~4,000 years.

2.2 Results

Osmium concentrations and $^{187}Os/^{188}Os$ ratios were measured on five bulk samples from the YD basal boundary dark layer and thirty-two samples were measured from horizons above and below it in Hall's Cave (Table S2.1). In total, samples were collected at high spatial and temporal resolution across depositional ages ranging from 9,600 to 13,500 yr BP (Stafford, et al., 2009). Hall's Cave bulk sediments display large variations in Os abundance from 22.6 to 4,478 ppt and $^{187}Os/^{188}Os$ ratios from 0.12 to 2.35 (Figure 2.1). The samples are divided into two groups based on their Os abundances and $^{187}Os/^{188}Os$ ratios. In the first group (n=30, hereon named 'radiogenic'), the samples have $^{187}Os/^{188}Os$ ratios from 1.11 to 2.35 and Os abundances from 22.6 to 56.9 ppt. This combination of high $^{187}Os/^{188}Os$ ratios and low 10's of ppt Os abundances is typical for continental crust sediments (Shirey and Walker, 1998; Wu et al., 2013).

The second group (n = 7, hereon 'unradiogenic') has $^{187}Os/^{188}Os$ ratios from 0.12 to 0.42 and Os abundances from 105 to 4,478 ppt. These values are not typical of continental crust and reflect an input from an extraterrestrial or a mantle source. These samples come from five different horizons located at, above, and below the YD basal boundary layer (Figure 2.1). Of the five YD basal boundary samples four are radiogenic with $^{187}Os/^{188}Os$ values of 1.49 to 2.22, whereas only HC17_44 has a low, non-continental crust-like $^{187}Os/^{188}Os$ value of 0.41 and Os abundance of 105 ppt.

Samples of Hall's Cave sediments with $^{187}Os/^{188}Os$ ratios > 1.11 (e.g., belonging to the radiogenic group) have CI chondrite-normalized HSE patterns that are indistinguishable from upper continental crust (Figure 2.2). The unradiogenic samples, with $^{187}Os/^{188}Os$ ratios ≤ 0.42, including the one sample in this group at the Younger Dryas boundary (YDB) layer, have low Ir, Ru, Pt, Pd and Re abundances that are also similar to upper continental crust (Figure 2.2 and Table S2.2). Hence, there is no enrichment in these elements spanning across the YD section in Hall's Cave. This result is consistent with data from eight other YD locales (Paquay et al., 2009). However, the CI chondrite-normalized HSE patterns for the unradiogenic $^{187}Os/^{188}Os$ samples display a distinct enrichment for Os concentrations relative to upper continental crust and the radiogenic samples (Figure 2.2).

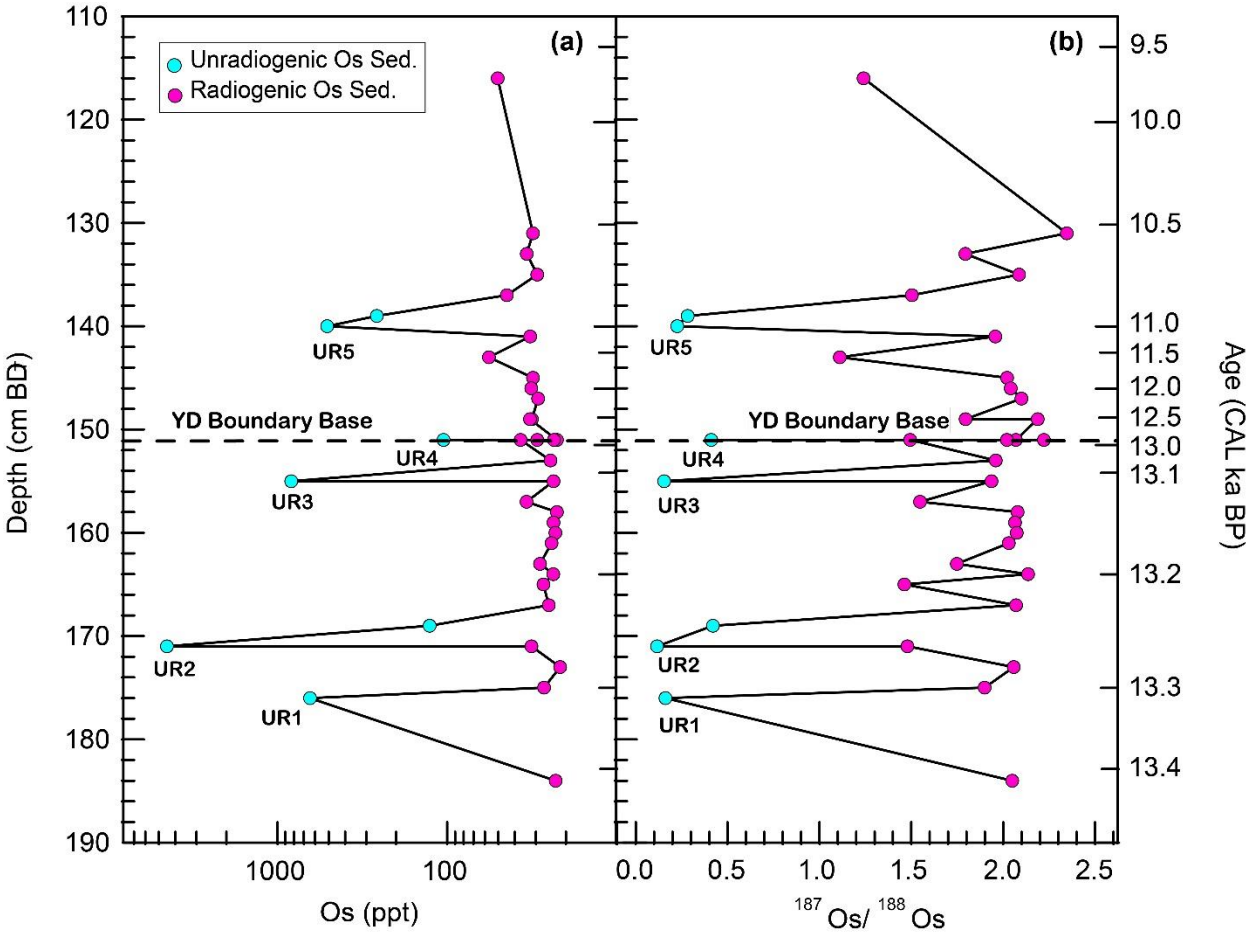

Figure 2.1 Depth below datum (DBT) profiles against total Os abundances (ppt) and $^{187}Os/^{188}Os$ ratios of Hall's Cave sample section. (a) Depth versus total Os abundances (ppt), (b) Depth versus $^{187}Os/^{188}Os$ ratios. Local datum used in this study was placed by Toomey in 1986 (Toomey, 1993)**.** UR = unradiogenic, UR 1-5 represent five unradiogenic Os peaks. Depth values are the basal depth of the 1 cm thick excavation interval relative to the datum. Six ages were calibrated using direct AMS ^{14}C measurements with 95.4% confidence intervals, then used to calculate the rest of the dates with linear interpolation between the dated levels.

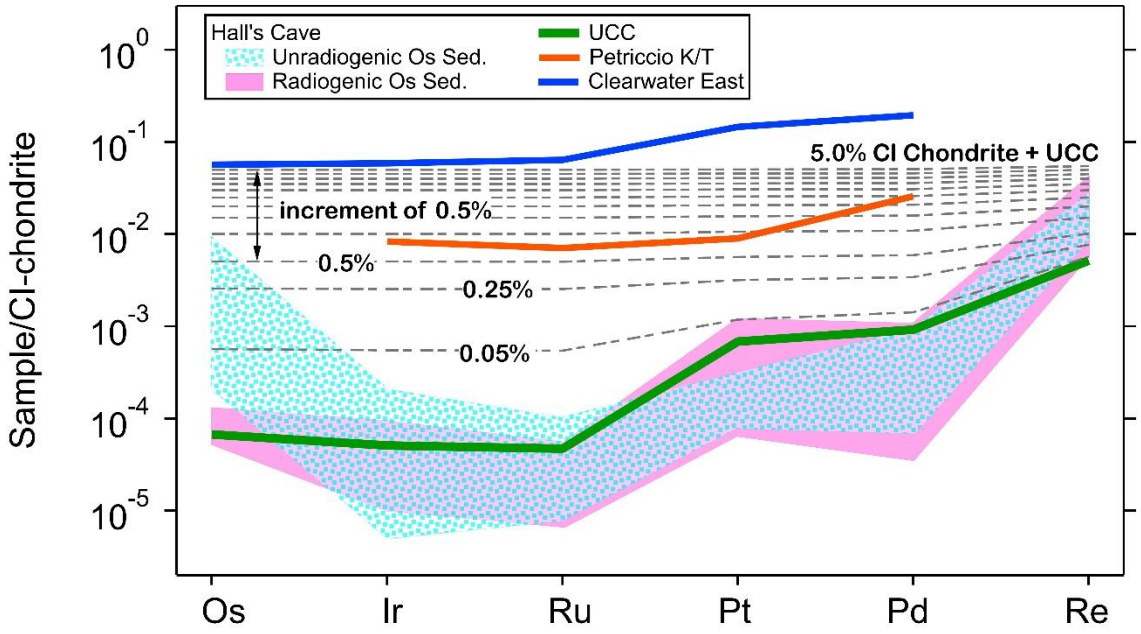

Figure 2.2 CI chondrite-normalized HSE patterns and incremental mixing model of CI chondrite material into an Upper continental crust–like target. From 0.5 – 5.0 % mixing lines use 0.5% increment, beneath are the 0.05% and 0.25% lines. HSE patterns of Hall's Cave Unradiogenic Os sediments (blue dotted pattern) and Radiogenic Os sediments (pink shadow), compared with average upper continental curst (Esser and Turekian, 1993; Park et al., 2012), Clearwater East Impact melt rock, Canada (Evans et al., 1993; McDonald, 2002), Petriccio K/T boundary, Italy (Evans et al., 1993). Cl-chondrite values used for normalization are from Wasson and Kallemeyn (1988).

2.3 Discussion

2.3.1 Testing the Younger Dryas Impact Hypothesis Using Os Isotopes and HSE

The Os isotope systematics and HSE abundance patterns (Figure 2.2) indicate that exotic materials were contributed during multiple time intervals to the continuous sedimentary record in Hall's Cave. It is unlikely that multiple impacts/airbursts at these distinct time intervals over ~4,000 years had occurred (Figure 2.1). Further, a bolide compositional signature is unsupported with mass balance calculations for the $^{187}Os/^{188}Os$ ratios and HSE concentrations with end members of CI chondrite and upper continental crust. For Os, assuming CI chondrite values of $^{187}Os/^{188}Os = 0.127$ and Os of 486,000 ppt, and upper continental crust values of $^{187}Os/^{188}Os = 1.3$ and Os of 30 ppt (Wasson and Kallemeyn, 1988; Esser and Turekian, 1993; Park et al., 2012), the amount of meteorite material mixed into upper continental crust to explain the $^{187}Os/^{188}Os$ ratios of the Hall's Cave unradiogenic samples is 0.02 to 0.79%. Similar models using the other HSE indicate 0.05 to 5.00% contribution from a CI chondrite impactor. The addition of only 0.05% CI chondrite to the upper continental crust results in gentle positive slopes from Os to Re for CI chondrite-normalized patterns (Figure 2.2). Increasing the amount of CI chondrite to 0.5 – 1.0%, to match the highest amounts of Os found in the unradiogenic samples, the slopes of the mixtures flatten. These models do not match the relative distribution or abundances observed in the unradiogenic samples with the Os-enriched concentrations (Figure 2). The measured abundances are not matched by models using any other chondrite material, including enstatite, ordinary, or other carbonaceous chondrites (Figure S2.1 and Table S2.3). Impact melts with purported admixed chondritic material show an even distribution of HSE (Figure 2.2). No iron meteorite groups display the observed distinct enrichments in Os relative to

Ir, or the increasing abundances from Ru, to Pt, to Pd, to Re relative to CI. Thus, mixing iron meteorites with upper continental crust will not result in the HSE patterns exhibited by the unradiogenic samples (Figure S2.1 and Table S2.3).

The modeling above indicates that the combined HSE abundances and $^{187}Os/^{188}Os$ ratios are inconsistent with contribution from an extraterrestrial impactor or bolide airburst in agreement with previous results from other YD locales (Paquay et al., 2009). Failing a meteorite source, the source of the enrichments and isotopic signature remains unresolved. A better explanation must include a terrestrial source of material able to be supplied frequently and episodically across short time intervals (years to decades).

2.3.2 Volcanic Origin of Hall's Cave Sediment $^{187}Os/^{188}Os$ and HSE Variations?

The Hall's Cave samples are characterized by a two end-member mixing model based on $^{187}Os/^{188}Os$ ratios and 1/Os abundances (Figure 2.3). Data from other YD locales with $^{187}Os/^{188}Os$ ratios scatter around the Hall's Cave data, consistent with distinct natural variations in the continental crust (Figure S2.2). Sediment cores from the Gulf of California and Cariaco Basin are not shown because Paquay et al. (2009) have conclusively argued that their $^{187}Os/^{188}Os$ ratios reflect rehomogenization with seawater and hence lack evidence of an unradiogenic $^{187}Os/^{188}Os$ component added to the sediments. The bulk sediment, bulk spherules, residues, and leachates from the Melrose, Pennsylvania YD locale (Wu et al., 2013) cluster around the unradiogenic $^{187}Os/^{188}Os$ samples from Hall's Cave. The leachates, which are surface films on the bulk spherules (Wu et al., 2013), plot to less radiogenic $^{187}Os/^{188}Os$ ratios and higher Os concentrations defined by the Hall's Cave samples. These relationships are consistent with mixing between Hall's Cave crust and components broadly similar to the unradiogenic

$^{187}Os/^{188}Os$ spherule surface films. This hypothesized mixing can yield the variation in Os isotope systematics for Hall's Cave unradiogenic $^{187}Os/^{188}Os$ samples. This mixing from two HSE sources provides a possible causal link between these North American locales for the unradiogenic $^{187}Os/^{188}Os$ ratios particularly for the Hall's Cave YD layer. The spherules deposited at the Melrose (PA) YD layer were interpreted to be airborne material (Wu et al., 2013). The unradiogenic surface films on the spherules are hypothesized to originate from a bolide as it ablated during heating in the Earth's atmosphere or as terrestrial material that was ejected back into the atmosphere and redeposited following impact. However, these scenarios are problematic. The $^{187}Os/^{188}Os$ ratios from 0.112 to 0.120 in the spherule surface films are unlike most meteorites that have $^{187}Os/^{188}Os$ ratios of ≥ 0.124, with a few from 0.120 to 0.124, and two at 0.117 (Wu et al., 2013). These low values in the spherule surface films are consistent with being ancient subcontinental mantle (SCM) of ≥ 2.4 Ga, but no known impact site of a YD age is present in areas where such material may be accessible (Wu et al., 2013). Thus, if the Os from these surface films are similar to the material within the YD layer in Hall's Cave, and potentially the other layers with unradiogenic $^{187}Os/^{188}Os$ ratios, then it is unlikely that this material came from a bolide, a series of bolides at different times, or from multiple impact sites. This conclusion is also in agreement with the HSE patterns of the Hall's Cave sediments that are inconsistent with being derived from a meteoritic source.

Instead, the unradiogenic $^{187}Os/^{188}Os$ ratios from 0.12 to 0.42 in seven of the Hall's Cave samples indicate that some type of mantle-derived material was likely incorporated into some sediment layers at different time intervals. The elevated Os concentrations in these samples of 105 to 4478 ppt relative to continental crust with 30 ppt Os, and the radiogenic $^{187}Os/^{188}Os$ samples with 22 to 55 ppt Os, is consistent with mantle-derived Os material being added to these

layers. If it is not impact ejecta from ancient SCM as discounted by Wu et al. (2013), one possibility is that exposed ancient mantle peridotite or komatiite (1000s of ppt Os) (Puchtel et al., 2005; Brandon et al., 2006) with low $^{187}Os/^{188}Os$ and high Os abundance was eroded and episodically provided a supply of sediment at these time intervals where the unradiogenic $^{187}Os/^{188}Os$ ratios are found in the layers. However, there are no known exposures of peridotite or komatiite within 100s of km of Hall's Cave rendering this possibility unlikely. Another possibility is local mafic volcanic material with mantle-derived $^{187}Os/^{188}Os$ ratios that is subsequently eroded and deposited in Hall's Cave. Mafic volcanic material is also problematic from the perspective of not having a source of this material nearby to erode.

One final scenario is that the source of the unradiogenic $^{187}Os/^{188}Os$ may be airborne material from concurrent volcanic eruptions, which would alleviate the need for nearby older volcanic sources to erode and deposit material in Hall's Cave. If the unradiogenic $^{187}Os/^{188}Os$ ratios in the YD layer and potentially the other layers in Hall's Cave are of volcanic origin, then the very high abundances of Os in the Melrose surface films of ~19,000 to 43,000 ppt (Wu et al., 2013) could reflect aerosols enriched in HSE associated with airborne volcanic tephra from distant eruptions, that are enriched in Os with mantle-like $^{187}Os/^{188}Os$ ratios.

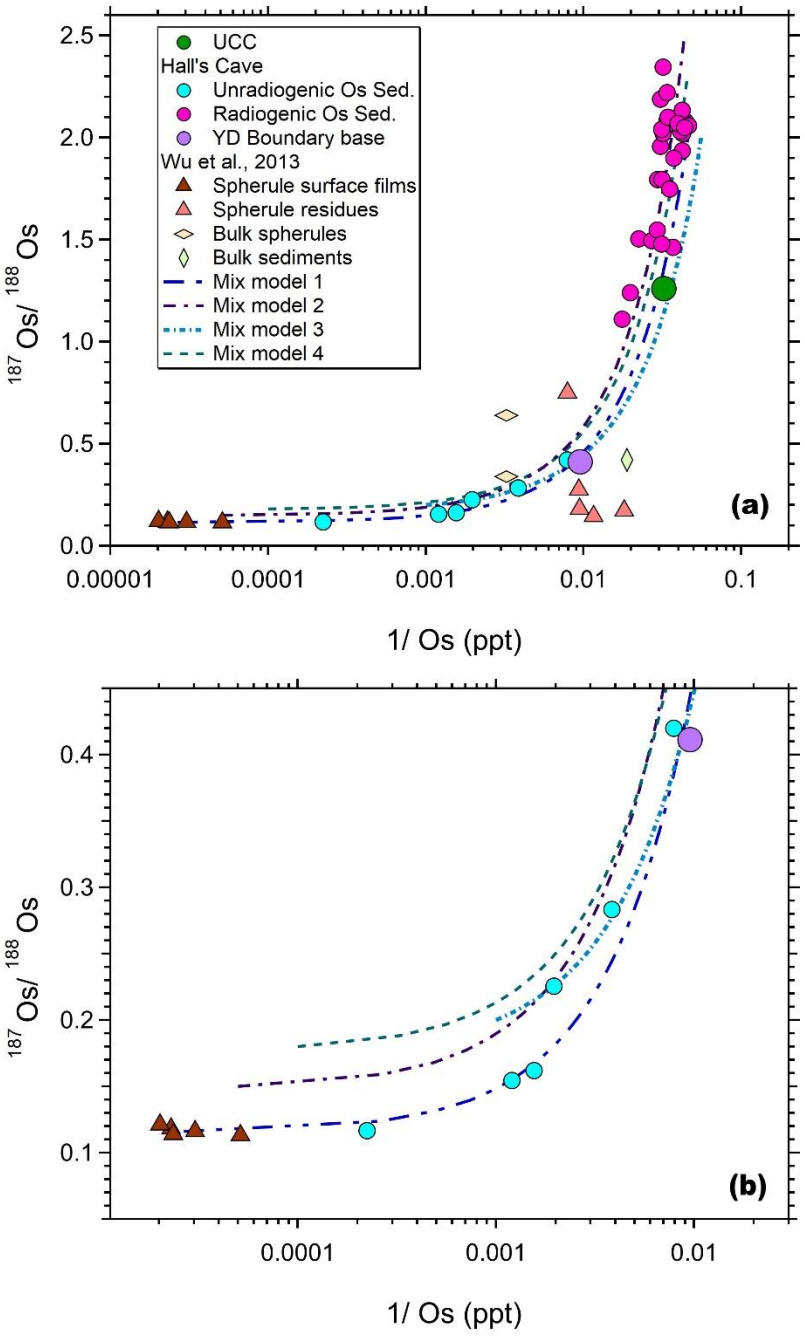

Figure 2.3. Osmium isotope results and mixing models between Hall's Cave crusts and mantle-like Os end-members. (a) $^{187}Os/^{188}Os$ versus 1/Os concentration (ppt) for Hall's Cave sediments with four mixing models for this study. Parameters used for the models are listed in Table S2.4 (b) Mixing models close-up view on the lower left end of (a). UCC is upper continental crust (Esser and Turekian, 1993; Park et al., 2012), data for bulk sediments, bulk spherules and spherule surface films and residues were for the Melrose (PA) YD site from Wu et al. (2013).

To test this hypothesis, mixing models were developed between Hall's Cave crust compositions and hypothetical mantle-like Os end-members. These models were parameterized to examine the range of potential variation in these components when mixed together, simulate the unradiogenic $^{187}Os/^{188}Os$ and high Os concentrations in the Hall's Cave samples. Table S2.4 lists the Os concentrations and $^{187}Os/^{188}Os$ ratios for the end member components used for the mixing calculations. In Mix 1 (Figure 2.3) the average of the leachates for Objects 2, 4, 5, 11, and 13 from the Melrose locale was used as the unradiogenic $^{187}Os/^{188}Os$ end-member. When this is mixed with Hall's Cave crust with 21 ppt Os and $^{187}Os/^{188}Os$ of 2.1, the mixing curve passes through the unradiogenic Os sample from the YD layer in Hall's Cave and three of the samples from the other layers in Hall's Cave. Three unradiogenic $^{187}Os/^{188}Os$ samples from other layers in Hall's Cave plot to higher values of $^{187}Os/^{188}Os$ and not along this mixing curve. Three other representative mixing curves are shown in Figure 2.3, where the Hall's Cave crust end member varies from 18 to 23 ppt and $^{187}Os/^{188}Os$ ratios from 2.0 to 2.5, with the unradiogenic Os end member varying from as low as 1,000 to approximately 40,000 ppt and $^{187}Os/^{188}Os$ ratios from 0.115 to 0.2. These mixing models are all hyperbolic and all 7 unradiogenic $^{187}Os/^{188}Os$ samples from Hall's Cave fall within the band of possible values generated by mixing this range of end-member compositions. This modeling indicates that the observed compositions of the Hall's Cave unradiogenic $^{187}Os/^{188}Os$ samples reflect a range in Os concentrations and $^{187}Os/^{188}Os$ values for unradiogenic Os end-members, when mixed with Hall's Cave crustal component. Thus, the different layers in Hall's Cave with unradiogenic $^{187}Os/^{188}Os$ ratios are unrelated to a single source of Os, as expected given the different depositional times, but instead

likely related to a process of high Os concentration material deposited having a range of $^{187}Os/^{188}Os$ values from around 0.115 to 0.20.

This range of $^{187}Os/^{188}Os$ values needed for the mantle end-member are within the range present in volcanic lava samples worldwide, for example the Cascade arc (0.129 to 0.253) (Borg et al., 2000), Ocean Island lavas from 0.110 to 0.176 (Day, 2013), and Ethiopian lavas from East African Rift (0.124-0.427) (Nelson et al., 2012) and numerous other volcanic rock locales. Aerosols measured at Mauna Loa in Hawaii have $^{187}Os/^{188}Os$ ratios of 0.136 to 0.140 (Krähenbühl et al., 1992), consistent with the compositions of lavas from this volcano (Brandon et al., 1999). Condensates from aerosols from Piton de la Fournaise fumarole on Reunion Island show that different sources can be tapped and decoupling in the $^{187}Os/^{188}Os$ ratio can occur between lavas and aerosols (Gannoun et al., 2015). The samples from the lowest temperature condensates (< 350ºC) have $^{187}Os/^{188}Os$ ratios of 0.130 to 0.135 and overlapping those of the associated lavas. The highest temperature condensates (384 to 400ºC) have $^{187}Os/^{188}Os$ ratios of 0.123 to 0.129, indicating derivation from older mantle sulfides and show that Os can be derived from different sources than those for the lavas resulting in distinct $^{187}Os/^{188}Os$ values. Hence, the lavas are not always a direct indication of the $^{187}Os/^{188}Os$ ratios for those of the associated aerosols, and these sources for Os can change during evolution of the volcano magmatic systems. What these relationships indicate is that it is not unexpected then that airborne cryptotephra with high Os concentration surface films derived from volcanic aerosols would have $^{187}Os/^{188}Os$ ratios consistent with the range of those needed to explain the range of unradiogenic $^{187}Os/^{188}Os$ sample values from Hall's Cave.

For this scenario, powerful volcanic eruptions provide the most likely source for the observed high Os abundances and low $^{187}Os/^{188}Os$ signatures at Hall's Cave and potentially

explain the surface films on the Melrose spherules in the YD layer. The record of punctuated volcanism would be preserved as cryptotephra horizons with unique chemical fingerprints within the stratigraphy. Mafic melts contain the highest concentrations of HSE with the concentration of at 0.1 to 1,000 ppt (Woodland et al., 2002; Day, 2013). Fractional crystallization produces more silicic, evolved melts with lower HSE concentrations (e.g., Os of 10 - 934 ppt) (Lassiter and Luhr, 2001; Woodland et al., 2002). Such values do not completely overlap with the Os concentrations preserved in the seven possible cryptotephra samples at Hall's Cave, which range from 105 to 4,478 ppt. Volcanic degassing may provide the required mechanism that enriches low magmatic HSE concentrations to much higher values. During ascent and depressurization volatiles exsolve from magma. Common volatiles include CO_2, H_2O, SO_2, H_2S, HCl and HF. Importantly, HSE partition strongly to an exsolved vapor phase, with estimated melt-vapor distribution coefficients as high as 10^5 to 10^6 (Yudovskaya et al., 2008; Zelenski et al., 2013). This process can be accentuated by both the increasing solubility of sulfur and increasing oxidation state of the magma during decompression. In oxidized magmas with lower amounts of H_2S, HSE concentrate in the melt where they are available to degas. This is because the sulfide minerals in which HSE would partition are unstable (Oppenheimer et al., 2011; Day, 2013). Sulfur becomes increasingly soluble with decreasing pressure, which causes the melt to become sulfur-undersaturated and forces HSE-bearing sulfides to dissolve back into the melt with subsequent gas release (Oppenheimer et al., 2011; Gannoun et al., 2016).

The HSE during an eruption are lost from the melt, added to the eruption column and exist in sulfur and other compounds and adhere to ash particles (herein referred to as volcanic aerosols) (Yudovskaya et al., 2008; Gannoun et al., 2015). The magnitude of a volcanic eruption controls how high the plume penetrates the atmosphere, which subsequently controls the

geographic distribution of the tephra. Large eruptions may thus entrain HSE far into the atmosphere where they can be transported long distances before deposition (Henley and Berger, 2013). Eruptions with magnitudes > 5 Volcanic Explosivity Index (VEI) reach the stratosphere and can be globally distributed as volcanic aerosols (Robock, 2000). Volcanic aerosols have a significant impact on climate interactions, ozone chemistry, and vapor transport, and therefore such particles have been the focus of observation and modeling (Oppenheimer et al., 2011). Particulate entrainment within the planetary wave-train results in global distribution of volcanic aerosols from high latitude volcanoes, with spread of the cryptotephra across the hemisphere, whereas equatorial eruptions may distribute volcanic aerosols in both hemispheres (Timmreck et al., 1999).

We contend from the analysis of Hall's Cave sediments that horizons with unradiogenic $^{187}Os/^{188}Os$ ratios are cryptotephra with surface films consisting of volcanic aerosols. Thus, the HSE concentrations should correspond to observed values in volcanic aerosols from eruptions in modern environments. Indeed, the HSE values in Hall's Cave follow a trend showing a progressive increase in concentrations from Ru to Ir to Os, and from Ru to Pt and Pd that closely matches the patterns of the Kudryavy volcano gas condensates, Kurile Islands (Figure 2.4). In particular, Ir and Pt have been used to support the bolide hypothesis in other YD locales (Firestone et al., 2007; Petaev et al., 2013). As shown in Figure 2.5, using Pt, Ir, Os, and Pd concentrations and ratios, the Hall's Cave unradiogenic Os samples instead closely match those for the range and variation of gas condensates from three different volcanoes (Figure 2.5) (Woodland et al., 2002; Yudovskaya et al., 2008; Gannoun et al., 2016). The range in HSE concentrations and ratios for all Hall's Cave samples plot as well-defined trends or clusters in these variation diagrams. These variations are consistent with mixing scenario between volcanic

aerosols with a range of HSE systematics related to specific supplies of material from different volcanoes, with upper continental crust, within any given unradiogenic $^{187}Os/^{188}Os$ layer, observed for $^{187}Os/^{188}Os$ versus 1/Os (Figure 2.3) and that for $^{187}Os/^{188}Os$ versus Os/Ir (Figure S2.3).

The one HSE that is not showing a similar enrichment in the Hall's Cave unradiogenic $^{187}Os/^{188}Os$ samples to that expected from volcanic aerosol addition is Re. Rhenium, like Os, shows up to a 2-order of magnitude enrichment in volcanic aerosols relative to upper continental crust but this is not observed in the Hall's Cave samples (Figure 2.4). If the volcanic aerosol hypothesis is viable, then the question arises as to why there is no Re enrichment. There are 2 possible scenarios. In the first scenario, Re was redistributed in the sediments thereby erasing the aerosol signature. Rhenium can be highly mobile in the surface environment in oxidizing conditions where it can form ReO^{4-} (Perrhenate). However, this is discounted because the Pt/Os and Re/Os ratios strongly correlate with $^{187}Os/^{188}Os$ in the Hall's Cave samples indicating little to no HSE mobility (Figure S2.4).

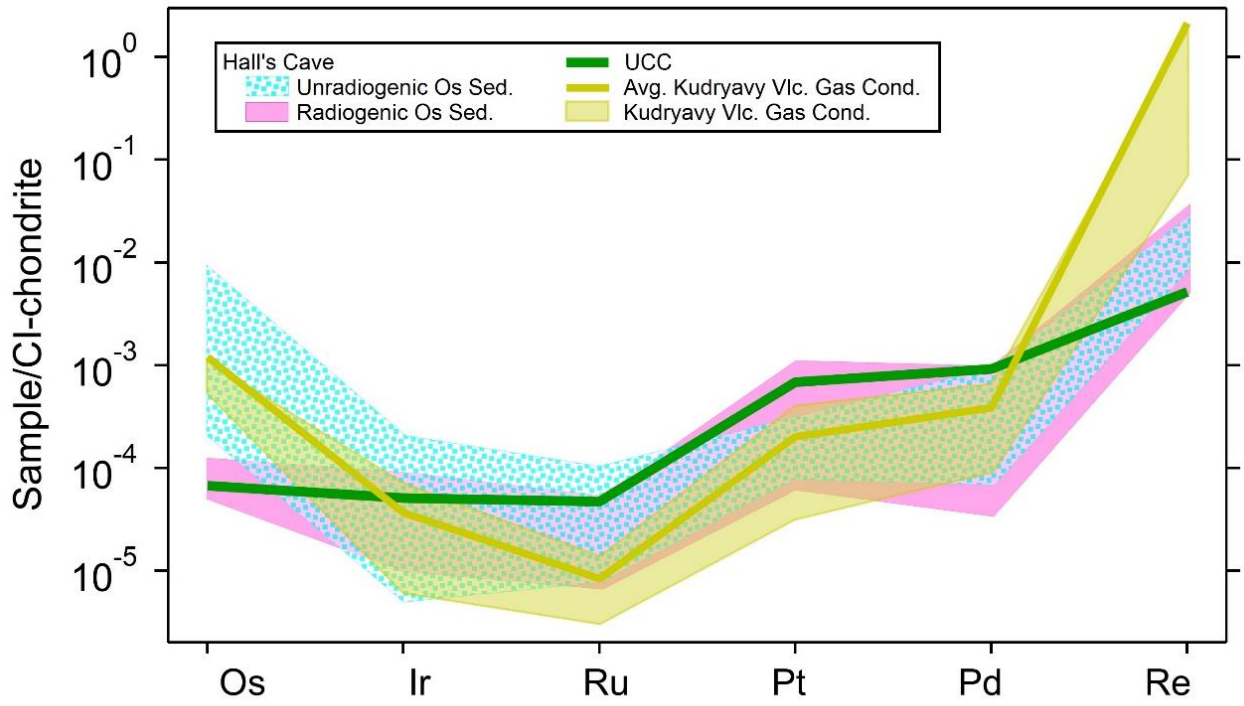

Figure 2.4. CI chondrite-normalized HSE patterns of all gas condensates and the average of the Kudryavy volcano gas condensates, Kurile Islands. Upper continental crust is from Park et al. (2012) Esser and Turekian (1993). The HSE patterns for the Os isotope radiogenic and unradiogenic groups from Hall's Cave are in pink shadow and blue dotted pattern, respectively. All Kudryavy volcano gas condensates (abbreviated to Vlc. Gas Cond.) (Yudovskaya et al., 2008) are plotted as yellow shadow whose average is presented as the dark grey line. Cl-chondrite values used for normalization are from Wasson and Kallemeyn (1988).

In the second scenario, Re from volcanic aerosols is not condensing on cryptotephra surfaces that are transported long distances prior to deposition in locations such as Hall's Cave. The limited studies on volcanic systems to date indicate that the HSE can strongly fractionate from each other during volatile phase transport and condensation from the aerosols (Yudovskaya et al., 2008). The HSE fractionations and minerals condensed, such as rhenite (ReS_2), K-Re-perrhenate, and those for Pt-Pd and Os alloys, are dependent on the temperature of condensation and volatile compounds that are present in the aerosols (Yudovskaya et al., 2008). These can vary greatly from volcano to volcano as do the variations for HSE relative to each other in the aerosols (Yudovskaya et al., 2008; Zelenski et al., 2013; Chaplygin et al., 2016). Further work will be required to better constrain the HSE relationships during these gaseous volcanic processes and as they relate to the observed aerosol fingerprints observed in the Hall's Cave unradiogenic $^{187}Os/^{188}Os$ samples and elsewhere.

Of note, the HSE systematics show only minor overlap with those for mafic and ultramafic lavas from different tectonic settings further supporting a scenario where the HSE are fingerprinting the aerosols from volcanic systems and unlikely sourced from respective silicate magmas. In addition, impact related materials have clearly different HSE systematics (Figure 2.5) consistent with a non-extraterrestrial source with low $^{187}Os/^{188}Os$ ratios for the unradiogenic samples. The HSE systematics in the Hall's Cave unradiogenic $^{187}Os/^{188}Os$ samples are thus best explained by input of cryptotephra with surfaces laden with HSE-enriched aerosols from distal, large-volume Plinian eruptions occurring at different times and added to the continental crust derived sediments.

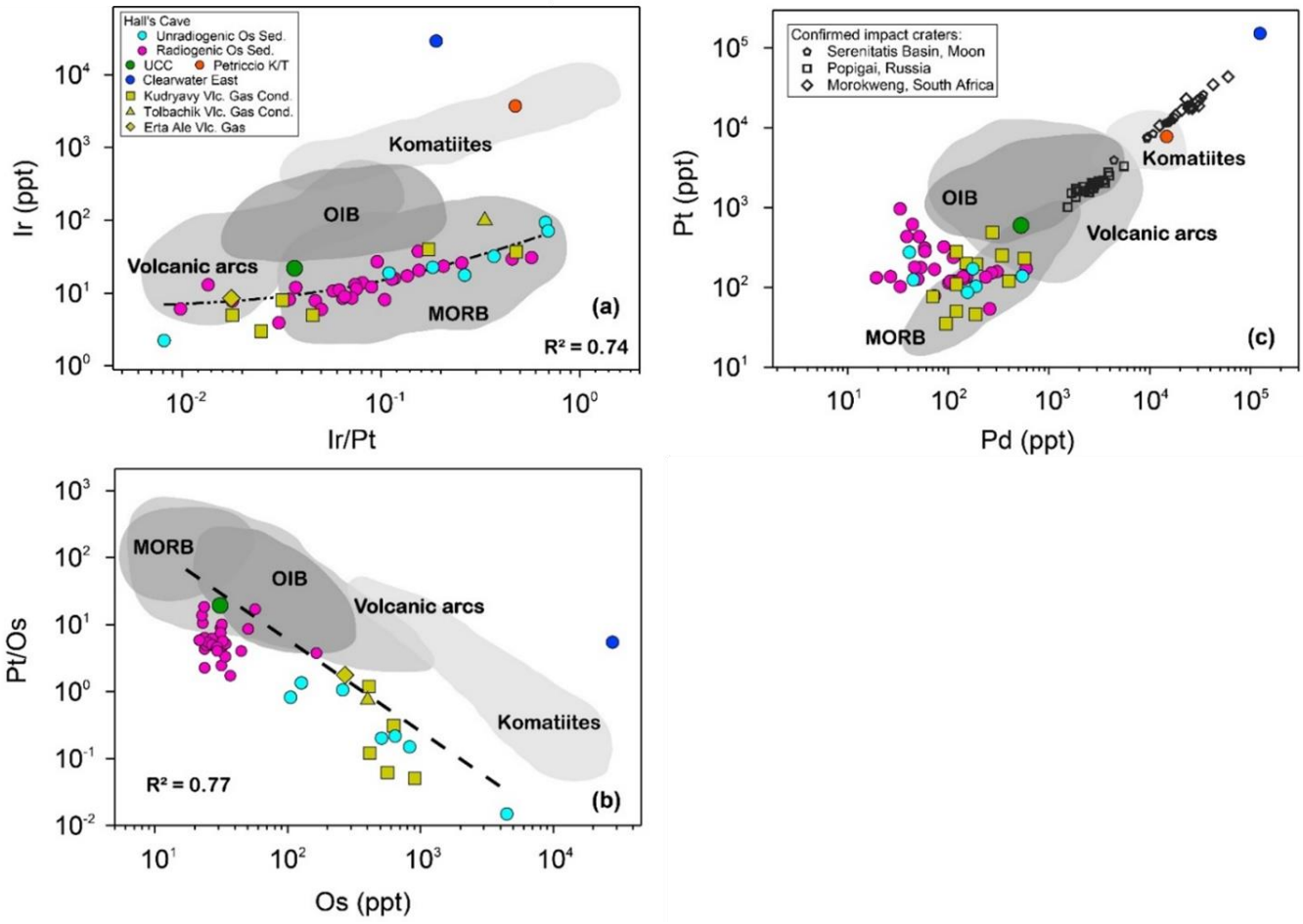

Figure 2.5. Binary plots of HSE elements and ratios of Hall's Cave samples. (a) Ir versus Ir/Pt, (b) Pt/Os versus Os, (c) Pt versus Pd. Compared to upper continental crust (Esser and Turekian, 1993; Park et al., 2012), Clearwater East Impact melt rock, Canada (Evans et al., 1993; McDonald, 2002), Petriccio K/T boundary, Italy (Evans et al., 1993), Kudryavy volcano gas condensates, Kurile Islands (Yudovskaya et al., 2008), Tolbachik volcano gas condensate, Kamchatka (Chaplygin et al., 2016), Erta Ale volcano gas (abbreviated to Vlc. Gas), Ethiopia (Zelenski et al., 2013) and confirmed impact craters, Popigai, Russia (Tagle and Claeys, 2005), Morokweng, South Africa (McDonald et al., 2001), Serenitatis basin, Moon (Tagle, 2005), MORB (Bézos et al., 2005; Yang et al., 2014), OIB (Ireland et al., 2009; Day et al., 2010), Volcanic arcs (Woodland et al., 2002), komatiites (Puchtel et al., 2005; Connolly et al., 2011). (a) Ir versus Ir/Pt, (b) Pt/Os versus Os. (c) Pt versus Pd. See text for more information.

2.3.3 Timing of Volcano Eruptions with Hall's Cave Sediment Deposition

Distant volcanic eruptions may provide both the compositional control and physical mechanism to produce the HSE-enriched cryptotephra horizons in Hall's Cave. The multidecadal to century scale time resolution for sedimentation in Hall's Cave obviate correlation with specific volcanic eruptions. However, this section documents significant eruptions within the time frame of the cryptotephra horizons fingerprinted by $^{187}Os/^{188}Os$ ratios and HSE systematics. These times indicate active volcanism in regions in the Northern Hemisphere that could have contributed cryptotephra to Hall's Cave sediments. The cryptotephra horizon at 151 cm at the YD basal boundary layer at 13.11-12.90 ka was likely sourced from the 13.10 ± 0.10 ka eruption of Laacher See. The Laacher See eruption ejected 6.3 km^3 (dense-rock equivalent, DRE) of sulfur-rich magma far into the stratosphere and likely dispersed volcanic aerosols throughout the Northern Hemisphere (Harms and Schmincke, 2000; Graf and Timmreck, 2001). Laacher See released from 2 to 150 Mt of sulfur. Although under debate, this may have triggered the temperature decline associated with YD climate change in the Northern Hemisphere (Baldini et al., 2018).

To identify possible volcanic sources for the other horizons in Hall's Cave that have $^{187}Os/^{188}Os$ ratios and HSE signatures consistent with cryptotephra, the ^{14}C ages of large magnitude volcanic eruptions during the late Pleistocene to Holocene are compared to the ^{14}C ages of the five HSE-enriched unradiogenic horizons (UR 1-5) in Hall's Cave (Table S2.5, Figure 2.1). The five interpreted cryptotephra horizons can be grouped into three volcanic mixing events that correlate well with known eruptions. The couplet of UR1 and UR2 horizons at 176 and 171 cm BD_T (below datum by Toomey in 1986 (Toomey, 1993) with a depositional age of 13.33 ± 0.19 ka, is similar to the Glacier Peak volcano in Washington, USA erupted at

13.71-13.41 ka and/or the J Swift tephra erupted from Mount Saint Helens erupted at 13.75-13.45 ka (Table S2.5). Importantly, these eruptions demonstrate that the Cascade volcanic arc was highly active at these times and would likely have dispersed volcanic aerosols and cryptotephra widely across the Northern Hemisphere.

There are possibly two eruptive candidates for Horizon UR5 at 140 cm BD_T which dates to 10.98 ka. Both the Fisher Tuff eruption from the Aleutian Arc and the Lvinaya Past eruption from the Kuril Arc occurred during the appropriate time interval (Table S2.5). Each of these large-volume arc volcano eruptions produced a Plinian eruption column that reached the stratosphere and distributed volcanic aerosols across North America (Pyne-O'Donnell et al., 2016).

2.4 Conclusions

The mass balance models using a range of chondrite and iron meteorite HSE abundances indicate that it is highly improbable the addition of meteoritic impactor components into continental crust could reproduce the observed chondrite-normalized HSE patterns for the Hall's Cave unradiogenic $^{187}Os/^{188}Os$ samples. A two end-member mixing relationship between Melrose (PA) spherule surface films and Hall's Cave bulk sediments demonstrate a distinctly different Os isotope systematics for the YD layer. The four other layers above and below the YD layer with unradiogenic $^{187}Os/^{188}Os$ ratios are consistent with mixing between Hall's Cave sediment and mantle-derived end-members with a range of $^{187}Os/^{188}Os$ ratios from 0.115 to 0.2. This range of $^{187}Os/^{188}Os$ ratios overlaps those for lavas from different tectonic settings worldwide and those measured on volcanic aerosols. The HSE ratios and chondrite-normalized patterns for these samples from Hall's Cave display close similarity with volcanic aerosols. The

five unradiogenic Os peaks, including the YD layer fall within a ~ 4,000-year time interval. The unradiogenic $^{187}Os/^{188}Os$ ratio and HSE abundance data from Hall's Cave sediments are inconsistent with the Younger Dryas impact hypothesis. Alternatively, these levels contain cryptotephra and associated aerosols derived from large Plinian volcanic eruptions. The Younger Dryas horizon correlates in time with the Laacher See eruption with a VEI of 6 and a 6.3 km^3 eruptive volume that was dispersed throughout the Northern Hemisphere. Previously discovered Younger Dryas markers, such as nanodiamonds and other wildfire products are not necessarily solely impact induced. Instead these could originate from high-temperature, large-scale volcanic eruptions whose explosive conditions are capable of producing molten silica and carbon spherules and possibly nanodiamonds (Lonsdaleite) (van Hoesel et al., 2014).

These observations from the Hall's Cave section also explains the lack of an Os isotope ET signature, or for the interpretation of a cryptotephra signature, at many YD locales across the Northern Hemisphere. Deposits of cryptotephra at any given time would be dependent on dispersal of the eruptive products from the volcanos emitting them, which could be localized or found in narrow bands depending on the dispersal patterns. This issue requires further investigation using HSE and Os isotopes to track dispersal dynamics.

The results here have implications for not only the Younger Dryas Event, but also other Pt and Ir enrichment events in Earth history and where other supposed bolide markers have been used to support impacts at these times. This analysis indicates that coupled Os isotope and HSE concentration data are needed at close stratigraphic intervals above and below suspected bolide events to evaluate an alternative volcanic origin.

2.5 Materials and Methods

Approximately 1 cm thick sediment samples were taken consecutively along vertical sequences transecting the YDB layer in Hall's Cave. The depths are measured at the base of each 1 cm thick sampling unit, for example, HC16_01 was extracted sediment between depths of 151 cm and 152 cm. Samples were dried at ~200 ℃ for three hours. Hereafter, samples were weighed, spiked, and dissolved in reverse aqua regia using the Carius tube digestion method (Shirey and Walker, 1995) at 240°C for a continuous ~ 48 hours. Subsequent acid solution processing was closely followed by CCl_4 solvent extraction (Cohen and Waters, 1996), microdistillation (Birck et al., 1997) and ion exchange chromatography to obtain purified HSE and Os isotopes. Osmium isotope and HSE abundances were determined with a mixed spike via isotope dilution using a negative thermal ionization mass spectrometer (ID-NTIMS) Thermo Fisher Triton Plus and quadrupole ICP-MS respectively at the University of Houston. No metal tools were used for collecting or transferring samples during any stage of the sampling or chemical processes. Details of sampling site, sampling techniques, HSE and Os isotope methodology are given in the Supplementary Materials.

2.6 Supplemental Information

Hall's Cave Sediment Section

Hall's Cave is located in Kerr County, Central Texas, and lies in the center of the Edwards Plateau. It was formed via karst activity of the Cretaceous, Edwards Group limestone platform during the Quaternary (Kastning, 1987; Toomey, 1993). Sedimentation in the cave

began ~20,000 years ago resulting in fluvial and colluvial deposits derived from several tens of hectares surrounding the cave and formed a 3.8 m thick stratigraphic sequence (Toomey, 1993; Bourne et al., 2016). The stratigraphic sequence in Hall's Cave is exposed in three vertical walls approximately 2.5 m high from previous excavations (Toomey, 1993; Bourne et al., 2016) (Figure S2.5). The sediment section, from the top surface to the base is as follows. The upper most layer consists of biological remains, brown and red clays with cobbles and boulders, followed by a 30 to 40 cm black guano unit with limestone cobbles, clastic sediments, wood fragments, charcoal, and bones on the top. This is followed by a ~60 cm thick dark brown clay with pebbles with lesser amounts of organic materials such as guano, hearth and bone. Below these layers at ~1 m depth in the section, is a 60 to 80 cm of brown clay with cobbles, charcoal, coprolites and several pebble zones. Fossiliferous material is enriched in the bottom ~10 cm layer. The Younger Dryas layer at ~1.75 m depth is approximately 20 cm thick and consists of dark brown fine-grained materials with a distinct color difference from the contacting layer beneath. The layer at ~1.95 m directly below the Younger Dryas layer is ~ 20 cm red brown clay with a moderate angular blocky structure. This overlies an extremely abundant pebble and cobble clay layer that extends downward ~80 cm to the bottom of the excavation wall (Toomey, 1993)**.** The uniform dark and cool depositional environment in the cave limited pedogenesis and preserved a fairly continuous section with a hiatus at 191 cm (younger than 1 ka) (Toomey, 1993; Wong et al., 2015; Bourne et al., 2016). Before the YD episode at 12.9 ka, the sedimentation rate was ~3 cm/ 100 years. After the YD event, the sedimentation rate slowed down to ~1 cm/100 years (Bourne et al., 2016), subject to the fact that Younger Dryas cooling had an extensive influence on terrestrial environments such as climate and vegetation change (Brauer et al., 2008), and depositional environment.

Sampling

Sampling in this study was conducted primarily in the south excavation wall originally placed in 1986 by Toomey (Toomey, 1993) from 35 cm above to 33 cm below the YD boundary base (Figure S2.5). Sample positions were measured vertically relative to an absolute datum (Toomey, 1993), which is ~1.8 m above the present sediment floor (Bourne et al., 2016), the base of YD boundary dark layer is 151 cm below datum (Toomey, 1993). Each sampling unit is ~ 1 cm thick, the depths used in this study represent the base of each unit, for example, a specimen with a depth of 151 cm was taken between 151 cm and 152 cm below the datum. A non-metallic spatula with a width of 5 cm was used to extract sediments to avoid cross-contamination. In total, vertically 32 bulk sediments weighing 3~8 grams each were sampled, five of them were laterally collected along the YD boundary.

Age Model Construction

The chronology for this study is constructed based on six calibrated dates using accelerator mass spectrometry (AMS) ^{14}C measurements conducted at the Stafford Research Laboratories. The age calibration used Bayesian analysis of radiocarbon dates on the software OxCal software (Bronk Ramsey, 2009) with a 95% confidence interval. Output calibrated date values were in ranges but converted to averages for forming a single axis for depth-age correlation in Figure 1. From the oldest to the youngest age in calibrated ka before present (CAL ka BP), these dates are labeled as 1-6, as shown in Figure S2.6.

First, we assume a linear accumulation rate between dated levels, then the age is treated as variable y and depth as variable x, with a relation of $y = a + bx$. Each trending line has two-

point controls, the intercept a and coefficient b are determined by the two points, for example, y = 10.5x + 11466 is the equation calculated by fitting through point 1 and 2. The depth range for the six points is from 116 cm ~ 176 cm. The sampling sequence goes below 176 cm and above 184 cm, so the age estimation for these two depth intervals was extrapolated using the same liner equation as between point 1 - 2 and point 5 – 6. The complete estimated ages are listed in Table S2.2.1.

Methods

Extraction and Measurement of Osmium Isotopes

Sediments obtained from study site were dehydrated in an oven at ~200 °C for ~3 hours with no contact with metallic products. Approximately 1.0 g each of dried soil samples were weighted and transferred to cleaned Carius tubes (CTs). A mixed HSE spike consisting of enriched ^{190}Os, ^{191}Ir, ^{99}Ru, ^{194}Pt, ^{105}Pd, and ^{185}Re) and 12 mL of aqua regia solution (3 ml conc. HCl and 9 ml conc. HNO_3) were added to the CTs. After freezing and sealing, the CTs were transferred to an oven and were digested at 240°C for a minimum of 48 hours. Following digestion, CTs were frozen, opened then thawed, and Os was extracted using CCl_4 (20). The Os was then back extracted into HBr (Cohen and Waters, 1996), and further purified via H_2SO_4/H_2CrO_4 microdistillation (Birck et al., 1997). The isolated Os was then loaded onto H. Cross Company^{TM} 99.995% pure Pt filaments as a Br salt and coated with a thin layer of $Ba(OH)_2$ activator.

The Os isotopic compositions were determined via negative thermal ionization mass spectrometry (NTIMS) on a ThermoFisher Triton Plus at the University of Houston. Osmium was measured as OsO_3^- via ion-counting using a secondary electron multiplier and collected for

150 cycles with 16s integration time in peak-hopping mode. Repeated measurements of UMD Johnson Matthey Os standard were conducted to monitor reproducibility of isotope ratio measurements and cup drift, the standard yielded $^{186}Os/^{188}Os$ of 0.12063± 0.00084, $^{187}Os/^{188}Os$ of 0.11420 ± 0.00068, $^{189}Os/^{188}Os$ of 1.21990 ± 0.00504, and $^{190}Os/^{188}Os$ of 1.9864 ± 0.00836 (2σ standard deviation n=10) consistent values reported by Goderis et al. (2017). Measured isotopic ratios were spike stripped, corrected for isobaric oxygen interferences, instrumental mass fractionation ($^{192}Os/^{188}Os$=3.083), and procedural blank contributions. Uncertainties were obtained through the error propagation of uncertainties in blank abundance and isotopic composition, spike abundance values, mass spectrometry measurements of Os, and the reproducibility of the Os isotopic values of the standard. Average procedural blank was 0.35 ± 0.55 pg/g for Os with $^{187}Os/^{188}Os = 0.17 \pm 0.01$ (2σ, n = 10).

Determination of Highly S Elements

Following the extraction of Os, the remaining aqua regia solutions that containing all of the other HSE were dried down at ~80 °C and converted to the chloride form by repeated dissolutions in 6N HCl and then evaporated to dryness. The sample solutions were purified for Re and PGEs as a group using Eichrom AG 1X8 100-200 mesh anion resin following a modified procedure from (Day et al., 2016). The Re and PGEs were then further purified as a group using cation exchange columns with 1.6 mL of Eichrom AG50X-8 100-200 mesh cation resin following the procedure of Puchtel and Humanyun (2001).

Following collection of Re and the PGEs, the cuts were brought up in 1.4 mL of 2% HNO_3 for measurement. Isotope dilution analyses were performed on an Agilent 8800 Triple Quadrupole ICP-MS at the University of Houston. The Ru, Pd, Pt, and Re isotopes were

measured in a NH_3 carrier gas, while Ir isotopes were measured in a He carrier gas. This procedure insured minimization of possible isotopic interferences while maximizing signal intensities. Signal intensities for the sample solutions using these carrier gases were monitored for monoisotopic interferences from Hg, Zn, Mo, Zr, La, Lu, and Hf and their possible hydrides and oxides (LuO: ^{191}Ir HfO: ^{193}Ir, ^{194}Pt, ^{195}Pt, ^{196}Pt) and were found to be negligible. Mass fractionation and instrumental drift were determined by applying sample/standard bracketing with a standard of natural isotopic composition and then applying this correction factor to the individual measurements. Over the course of the analytical campaign, reproducibility on 1 ppb of a mixed PGE standard of natural isotopic composition was better than 2% (2σ) for the isotopic ratios used for isotope dilution calculations (^{185}Re/^{187}Re: 0.5974 ^{191}Ir/^{193}Ir: 0.5949 ^{194}Pt/^{195}Pt: 0.9744, ^{100}Ru/^{101}Ru: 0.7479, ^{106}Pd/^{105}Pd:1.2238). Procedural blanks were 19 ± 0.95 pg for Ir, 5.5 ± 0.28 pg for Ru, 171 ± 8.55 pg for Pt, 9 ± 0.45 pg for Pd and 22 ± 1.1 pg for Re (2σ, n = 5).

Supplemental Figures and Tables

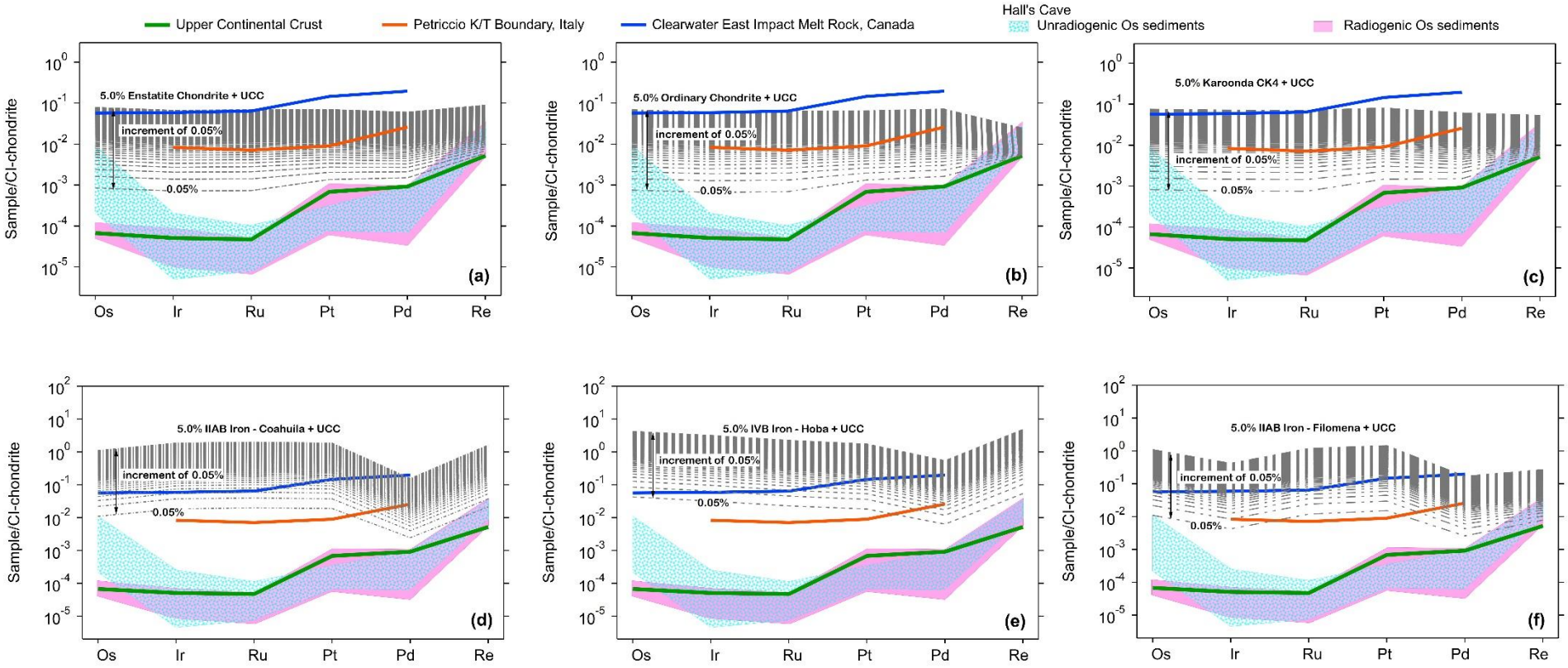

Figure S2.1. CI chondrite-normalized incremental mixing models of various input materials. (a) Enstatite, (b) Ordinary, or (c) Karoonda carbonaceous chondrites (Walker et al., 2002; Horan et al., 2003; Brandon et al., 2005; Fischer-Gödde et al., 2010; Day et al., 2016; Goderis et al., 2017) and (d) IIAB - Coahuila, (e) IVB - Hoba and (f) IIAB - Filomena iron meteorites (Cook et al., 2004; Petaev and Jacobsen, 2004; Walker et al., 2008) into an upper continental crust target, with Hall's Cave sediment sub-groups in the background as in blue dotted pattern and pink shadow. Confirmed impact melt rocks, Clearwater East Impact melt rock, Canada (Evans et al., 1993; McDonald, 2002), Petriccio K/T boundary, Italy (Evans et al., 1993) were plotted for reference.

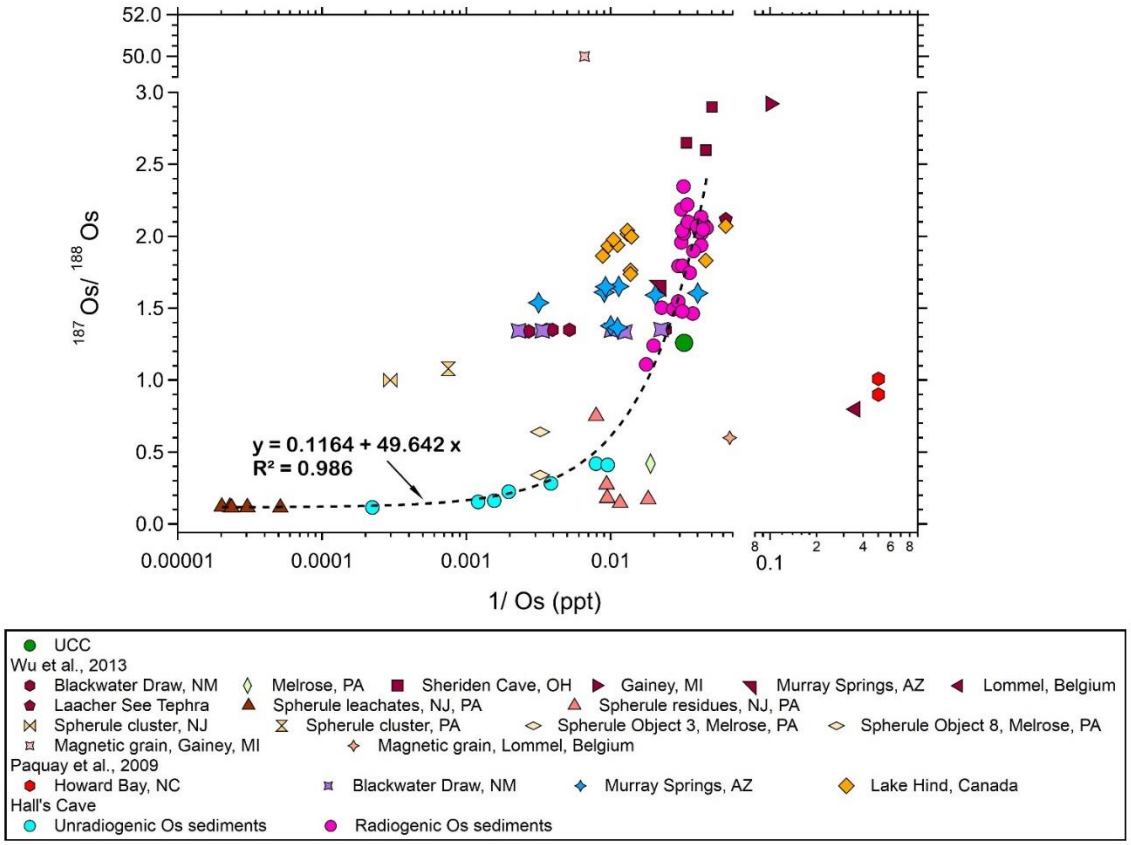

Figure S2.2 ^{187}Os/^{188}Os versus 1/ Os concentration (ppt) for Hall's Cave sediments. Compared to upper continental crust (Esser and Turekian, 1993; Park et al., 2012), Chicxulub impact melt rocks (Gelinas et al., 2004), data source for bulk sediments and spherule leachates and residues in the studied YD sites, Blackwater Draw (NM), Gainey (MI), Laacher See tephra, Melrose (PA), Murray Springs (AZ), Newtonville (NJ) and Melrose (PA) is Wu et al., (2013). Data for the YD sites: Howard Bay (NC), Blackwater Draw (NM), Murray Springs (AZ) and Lake Hind (Canada) are from Paquay et al. (2009). Dashed line shows linear mixing relation between all the Hall's Cave samples in this study and the spherule leachates (Wu et al., 2013) with a slope of 49.642 ± 1.23 and an intercept of 0.1164, and R^2 = 0.986.

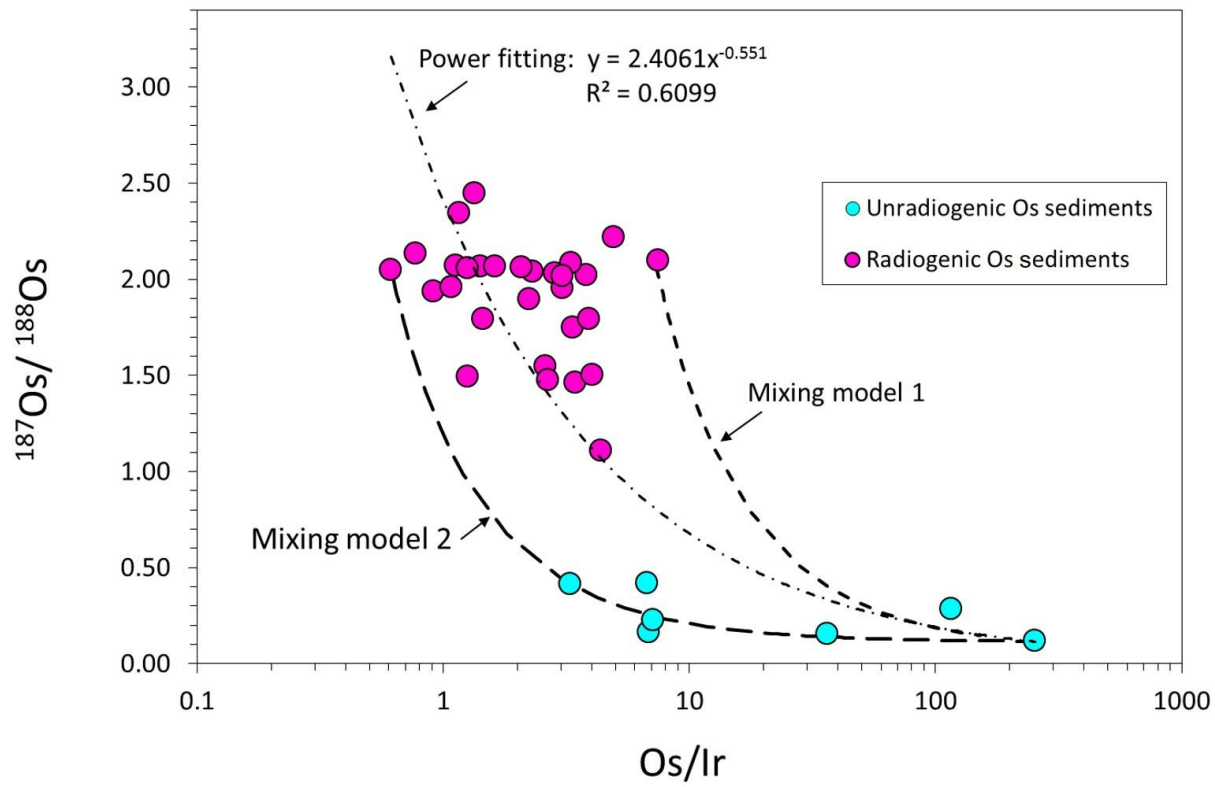

Figure S2.3 $^{187}Os/^{188}Os$ versus Os/Ir ratios for Hall's Cave sediment groups. Radiogenic Os and Unradiogenic Os. Mixing model 1 and 2 are mass balanced using the lowest $^{187}Os/^{188}Os$ sample on the lower right with radiogenic sample 1 and 2, respectively.

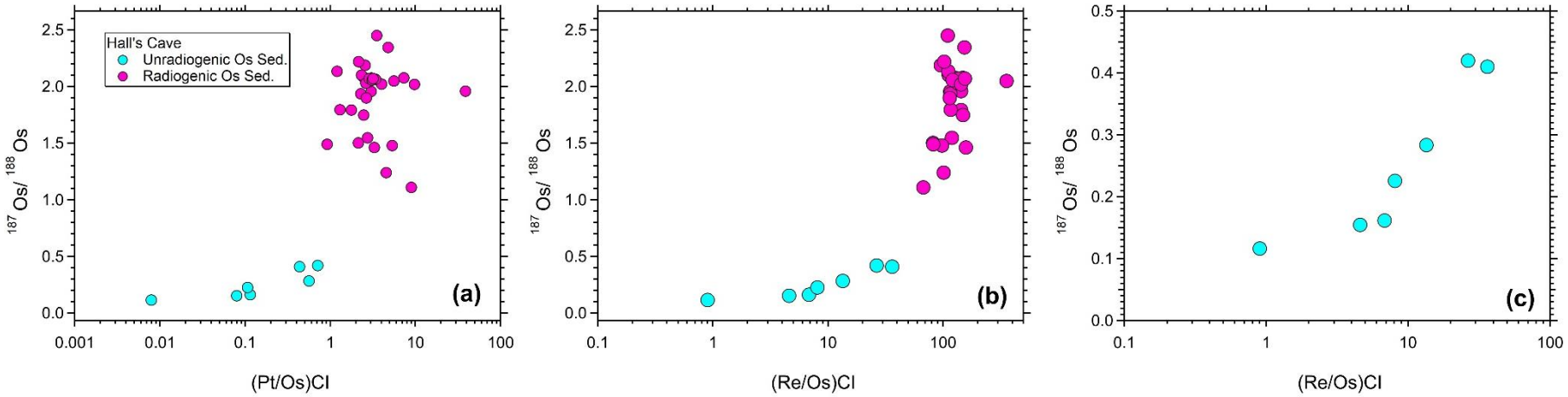

Figure S2.4 CI chondrite-normalized Pt/Os and Re/Os versus ^{187}Os/^{188}Os for Hall's Cave sediment groups. (a) (Pt/Os)CI versus ^{187}Os/^{188}Os, (b) (Re/Os)CI versus ^{187}Os/^{188}Os, (c) Close-up view of unradiogenic Os sediment group in (Re/Os)CI versus ^{187}Os/^{188}Os.

Figure S2.5 Hall's Cave sediment section with a 2 m scale bar. Wavy to sinuous, dashed red line represents the base of the dark brown fine-grained YD boundary layer. Photo Credit: Nan Sun, University of Houston

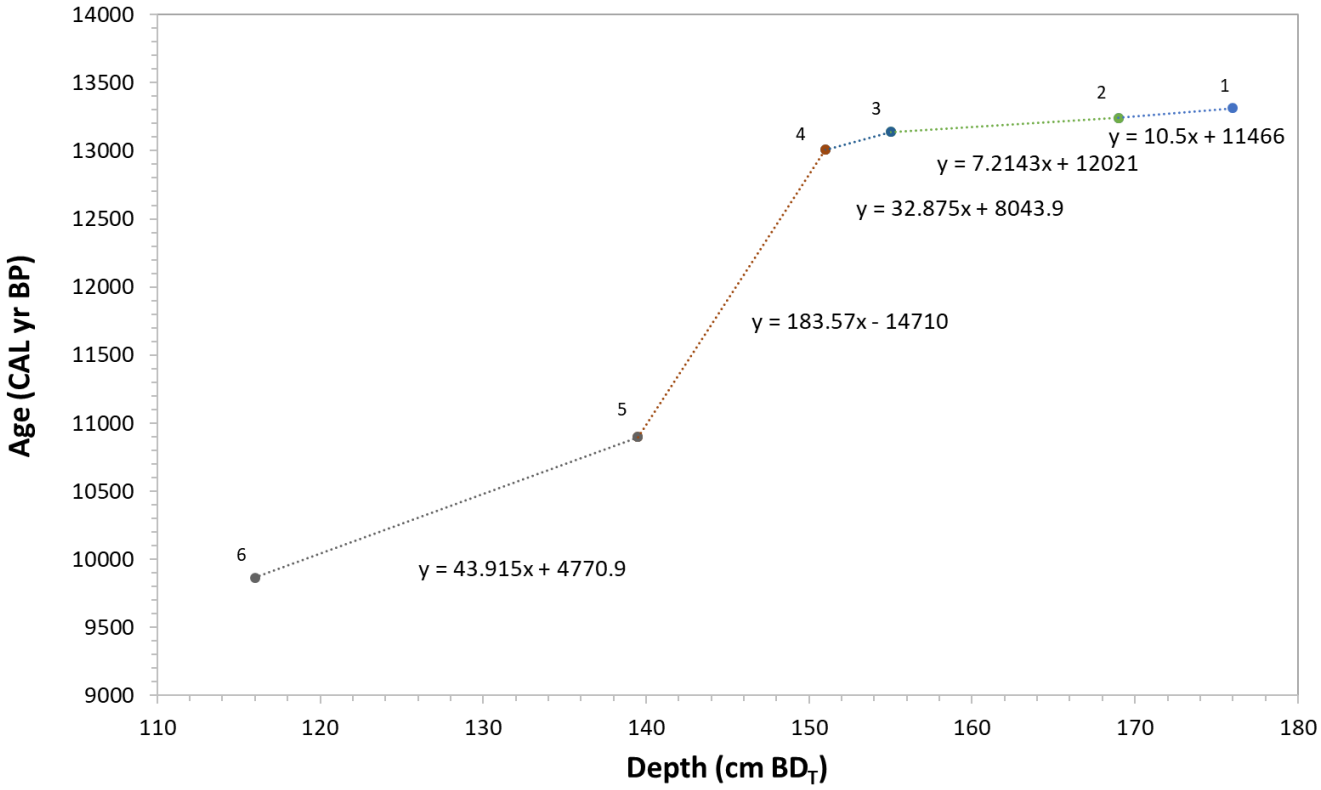

Figure S2.6 Age model constructed from six calibrated ages using accelerator mass spectrometry (AMS) ^{14}C measurements. They are labeled as 1 – 6 in the figure from the oldest age to the youngest. Each liner equation is also displayed between the two control points.

Table S2.1 Os isotopic ratios and HSE concentrations (ppt) for bulk sediments from YDB layers, Hall's Cave, Texas.

Sample§ (Hall's Cave)	Depth, BDT cm	Age CAL ka BP	Sample Weight gram	$^{187}Os/^{188}Os$*	± 2 σ	Os ppt	Ir ppt	Ru ppt	Pt ppt	Pd ppt	Re ppt
HC15_18	116	9.865^	0.51	1.24	0.06	50.5		23.9	434.4	51.5	441.8
HC15_16	131	10.524	0.53	2.35	0.20	31.3	27.0	26.8	282.0	58.7	414.6
HC16_22	133	10.612	1.08	1.79	0.06	34.0	23.4	12.9	113.3	101.1	421.1
HC16_21	135	10.699	1.11	2.09	0.09	29.5	9.0	4.2	136.3	140.1	302.7
HC16_20	137	10.787	1.04	1.50	0.04	44.6	11.1	25.0	180.0	46.1	314.4
HC16_19	139	10.897^	1.10	0.28	0.00	259.9	2.2	14.6	275.5	41.1	301.7
HC15_13	140	10.990	0.52	0.23	0.00	509.7	71.5	26.6	102.9	188.2	355.6
HC16_18	141	11.173	1.02	1.96	0.08	32.5	10.7	12.0	185.7	158.9	323.7
HC16_17	143	11.541	1.06	1.11	0.02	56.9	13.1	17.9	965.6	33.2	331.4
HC16_16	145	11.908	1.07	2.02	0.08	31.3	8.2	16.5	237.2	112.0	353.6
HC15_12	146	12.091	0.53	2.04	0.16	32.0	13.9	14.1	171.7	593.8	356.6
HC16_15	147	12.274	1.12	2.10	0.09	29.1	3.9	7.7	128.1	140.9	282.5
HC15_42	149	12.642	0.51	2.19	0.18	32.5		14.9	157.7	304.1	268.4
HC16_14	149	12.642	1.13	1.80	0.07	31.8	8.2	21.1	78.1	72.5	320.2
HC15_11	151	13.008^	0.51	1.49	0.10	37.0	29.4	25.8	64.3		262.1
HC16_01	151	13.008^	1.06	2.07	0.12	22.6	16.0	8.6	136.4	26.7	303.2
HC17_01	151	13.008^	1.01	2.02	0.11	23.6	7.8	12.2	435.1	38.7	292.3
HC17_39	151	13.008^	1.18	2.22	0.09	29.5	6.0	5.2	120.0	104.3	260.6
HC17_44	151	13.008^	1.03	0.41	0.01	105.3	32.1	11.7	86.6	154.9	328.4
HC15_10	155	13.008^	0.52	1.94	0.21	23.7	26.1	20.2	102.4	33.4	236.8
HC16_03	155	13.008^	1.00	0.15	0.00	829.7	22.7	5.1	124.7	44.8	328.8
HC16_04	157	13.153	1.06	1.55	0.06	34.1	13.1	31.9	176.9	53.3	351.9
HC15_15	158	13.160	0.51	2.08	0.25	22.6		28.7	312.1	58.4	290.4
HC16_05	159	13.167	1.02	2.06	0.12	23.7	11.4	16.4	151.7	268.4	297.2
HC15_09	160	13.173	0.52	2.07	0.24	23.1	20.6	32.8	132.4		259.1
HC16_06	161	13.180	1.01	2.03	0.11	24.3	8.6	14.0	120.4	117.2	281.6
HC16_07	163	13.194	1.03	1.75	0.08	28.4	8.5	15.1	132.5	19.3	364.8
HC15_08	164	13.200	0.52	2.13	0.24	23.7	30.8	24.8	53.8	257.8	226.9
HC16_08	165	13.207	1.01	1.46	0.09	27.1	7.9	15.2	168.5	72.8	370.3
HC16_09	167	13.220	1.10	2.07	0.10	25.2	15.5	31.6	136.6		298.3
HC16_10	169	13.241^	1.13	0.42	0.00	127.1	18.9	7.8	171.6	175.0	290.5
HC15_07	171	13.241^	0.52	0.12	0.00	4,477.8	17.7	65.8	67.0		348.2
HC16_11	171	13.241^	1.09	1.48	0.05	32.0	12.0	9.3	321.8	90.4	270.6
HC16_12	173	13.277	1.10	2.06	0.11	21.7	17.3	18.8	127.3	50.0	226.9
HC16_13	175	13.302	1.08	1.90	0.09	26.9	12.1	20.3	134.8	234.7	264.8
HC15_06	176	13.314^	0.52	0.16	0.00	643.3	93.7	12.2	139.2	541.6	379.0
HC15_05	184	13.412	0.51	2.05	0.24	23.0	37.6	21.6	243.5		707.7

§ All samples from Hall's Cave were measured in bulk after drying in oven for ~3 hours at ~200°C.

* Blank-corrected ($^{187}Os/^{188}Os$) ratios. Each batch was corrected with a blank of 0.35 pg of Os with $^{187}Os/^{188}Os$ = 0.17 in average.

^ Ages are in calibrated ka before present (CAL ka BP), values with symbol "^" are calibrated using ^{14}C accelerator mass spectrometry measurements and Bayesian Analysis software OxCal (Bronk Ramsey, 2009), the rest were calculated assuming linear interpolation between the dated levels.

BD_T = depth below datum, a local datum placed by Toomey in 1986 (Toomey, 1993). Depth values are the base of 1 cm thick sample excavation unit.

ND = not determined

Table S2.2 HSE concentrations (ppt) in volcanic gas condensates and impact materials from previous studies.

Reference	Os	Ir	Ru	Pt	Pd	Re
	ppt	ppt	ppt	ppt	ppt	ppt
Kudryavy Volcano gas condensates (Average)*	586	16	5	174	219	84,640
Tolbachik Volcano Gas Condensate, Kamchatka§	400	100	400	300	33,000	27,000
Erta Ale Volcano Gas, Ethiopia#	270	9		480		26,700
Petriccio K/T Boundary, Italy&		3,700	4,600	7,800	14,700	
Clearwater East impact melt, Canada¥	28,000	29,000	47,000	153,000	124,000	
Upper continental crust¤	31	22	30	599	526	198

* Kudryavy Volcano (Iturup Island, Russia) gas condensates are from Yudovskaya et al. (2008).

§ Tolbachik Volcano (Kamchatka) Gas Condensate is from Chaplygin et al. (2016).

Erta Ale Volcano (Ethiopia) Gas is from Zelenski et al. (2013).

& Petriccio K/T boundary data is from Evans et al. (1993).

¥ Clearwater East impact melt, Canada is from Evans et al. (1993) and McDonald (2002).

¤ Upper continental crust HSE are based on Esser and Turekian (1993) and Park et al. (2012)

Table S2.3 HSE abundances (ppb) in various chondrites and iron meteorites.

Reference	Os	Ir	Ru	Pt	Pd	Re
	ppb	ppb	ppb	ppb	ppb	ppb
Chondrites¶						
Enstatite chondrites	720	578	882	1200	678	64
Ordinary chondrites	634	528	818	1124	809	15
Karoonda carbonaceous chondrites	691	615	895	1398	690	37
Iron meteorites††						
IVB Iron – Hoba	39218	27570	29150	30780	6198	3731
IIAB Iron – Coahuila	10140	16000	25400	32170	1770	1230
IIAB Iron – Filomena	10033	3600	15200	25340	1910	200

¶ Chondrite data from Day et al. (2016), Goderis et al. (2017), Walker et al. (2002), Horan et al. (2003), Brandon et al. (2005) and Fischer-Gödde et al. (2010).

†† Iron meteorites data sources are from Cook et al. (2004), Petaev and Jacobsen (2004) and Walker et al. (2008)

Table S2.4 The Os concentrations and $^{187}Os/^{188}Os$ ratios of the end member components for the mixing models.

Mixing model	Unradiogenic Os Component		Hall's Cave Crust	
	Os ppt	$^{187}Os/^{188}Os$	Os ppt	$^{187}Os/^{188}Os$
Mix 1	37528.8	0.116	21	2.1
Mix 2	20000	0.15	23	2.5
Mix 3	1000	0.2	18	2
Mix 4	10000	0.18	22	2.3

Table S2.5 Late Quaternary Plinian volcanic eruptions in the Northern Hemisphere and their associated ages

Eruption/tephra Name	Volcano	Age B.P. (ka)	Composition	VEI*	Volume (km^3)	References
Saksunavatn	Grimsvotn, Iceland	10	Basaltic	Multiple	5	(Andrews et al., 2002; Neave et al., 2015)
Longonot	eastern Kenya	10.47 ± 0.21	Trachyte	6.7	15	(Rogers et al., 2004; Macdonald and Scaillet, 2006)
Fisher Tuff	Fisher Caldera, AK USA	10.66 ± 0.28	Dacite	7	10	(Bindeman et al., 2001; Stelling et al., 2005)
Lvinaya Past	Kuril Islands, Japan	10.48-10.78	Dacite	6.9	75	(Razzhigaeva et al., 2016; Smirnov et al., 2017)
Grímsvötn tephra series	Grimsvotn, Iceland	11.41-12.26	Basaltic	Multiple	5	(Jennings et al., 2014; Neave et al., 2015)
Vedde Ash (Solheimar)	Katla, Iceland	12.06 ± 0.05	Rhyolite	~5 or 6	3.3-6	(Tomlinson et al., 2012; Lohne et al., 2014)
Upper Toluca Pumice	Toluca, Mexico	12.53 -12.42	Dacite	6	6	(Arce et al., 2003)
Laacher See	Eifel, Germany	13.00 ± 0.10	Phonolite (zoned)	6	6.3	(Ramsey et al., 2015)
Glacier Peak set (B & G)	Glacier Peak WA USA	13.71-13.41	Dacite	5.7	4.4	(Gardner et al., 1998; Kuehn et al., 2009)
Mashu	Kuril Islands,Japan	13.59-13.99				(Bazanova et al., 2016; Smirnov et al., 2017)
J Swift Creek	Mt. St Helens, WA	13.75-13.45	Dacite	5.6	1.8	(Mullineaux, 1996; Pyne-O'Donnell et al., 2016)
N4, U-Oki, U4	Ulreung, Korea	13.94 ± 0.10	Phono-Trach	6.5	12.4	(Shiihara et al., 2011; Kim et al., 2014)
Neapolitan Yellow Tuff	Campi Flegrei	14.1	Trachyte	7		(Petrini et al., 1999; Deino et al., 2004)

*VEI = Volcanic Explosivity Index, relative measure of explosiveness for volcanic eruption

Chapter 3. Geochemical Evidence of Volcanic Signatures for the Younger Dryas Event

3.1 Introduction

The Younger Dryas (YD) cooling episode represents a major climate change during the last deglaciation between 12.9 -11.6 ka (Firestone et al., 2007; Kennett et al., 2009a; Wu et al., 2013). The triggering mechanism for YD event has been debated for decades. One widely accepted hypothesis of YD cooling is based upon proxies and mode results which favor massive freshwater discharge into the North Atlantic reducing the formation of deep waters and weakening or shutting down of the meridional overturning circulation (Broecker et al., 1985; McManus et al., 2004; Tarasov and Peltier, 2005; Carlson et al., 2007; Wang et al., 2018; Cheng et al., 2020). This hypothesis places the origin and termination of the YD within Earth's complex network of feedback mechanisms (Broecker et al., 1985; Alley, 2000, 2007; Cheng et al., 2020). Another prevailing hypothesis is that global YD cooling was triggered by fragments of a large, disintegrating asteroid or comet that struck the North hemisphere (Firestone et al., 2007). The purported projectile(s) impacted somewhere on the Laurentian ice sheet and destabilized it, which then triggered the global cooling (Firestone et al., 2007; Kennett et al., 2009b). Supporting evidence includes various markers including magnetic grains and microspherules, charcoal, soot, carbon spherules, nanodiamonds, elevated Ir and Ni abundances that peak at or near YD base boundary layer (YDB). Reproducibility of these makers is challenged by failing to duplicate the same patterns at the same sites (Surovell et al., 2009; Paquay et al., 2009; Daulton et al., 2010).

In addition, impact-sensitive highly siderophile elements (HSE: Os, Ir, Ru, Pt, Pd, Re) and $^{187}Os/^{188}Os$ ratios by Paquay et al., (2009) show no evidence of an extra-terrestrial (ET) input in any of the investigated locations. Similarly, at Hall's Cave, Texas, the $^{187}Os/^{188}Os$ ratios and HSE abundances from a sediment sequence through the YDB suggest a terrestrial origin for this marker, instead of ET impactor(s). The geochemical signatures of HSE and $^{187}Os/^{188}Os$ ratios detected at Hall's Cave trace back to a volcanic origin, challenging the impact hypothesis for YD cooling event (Sun et al., 2020). In this study, HSE abundances and $^{187}Os/^{188}Os$ ratios are reported from a well-dated section through the YD at the Debra L. Friedkin site along Buttermilk Creek, Texas. We also compare these results with the section from nearby Hall's Cave to evaluate and constrain the sources for the geochemical anomalies of this YD stratigraphic sequence. Trace elements including Ni and REE of Hall's Cave and the Debra L. Friedkin site are utilized to better understand the nature of the geochemical anomalies during the formation of these sediments.

3.2 Geological Settings at the Debra L. Friedkin Site

The Debra L. Friedkin site is located on the Edwards Plateau in central Texas approximately 200 km northeast of Hall's Cave, which is also located on the Edwards Plateau. At the Friedkin site, 104 m^2 of an area known as Block A was excavated, which is located on the second terrace adjacent to Buttermilk Creek (Waters et al., 2011; 2018). The Late Quaternary sediments in Block A consist of colluvium resting on Late Cretaceous limestone bedrock (Edwards Limestone and Comanche Peak Limestone Formations), that is overlain by 1.2 to 1.4 m of unstratified clay that was deposited incrementally during overbank floods from Buttermilk Creek. Post-burial disturbance of the sediments is minimal (Waters et al., 2011; 2018; Lindquist

et al., 2011; Driese et al., 2013). Seventy OSL ages were obtained from the Late Pleistocene and Early Holocene sediments of Block A, primarily from four vertical columns (Waters et al., 2011; 2018; Forman and Waters, 2016). All OSL ages are in correct stratigraphic order. The samples used in this study were collected from the south wall of the 2016 excavation block adjacent to OSL column labelled OSL-16. Fifteen total OSL ages were obtained in this column. The nine ages in this column between 90.30 and 90.60 meters above datum (m AD) were used in this study.

Within the floodplain deposits is an archeological record spanning the period from Pre-Clovis (Buttermilk Creek Complex), Clovis, Folsom, Late Paleoindian, Early Archaic, Middle Archaic, Late Archaic, and Late Prehistoric (Waters et al., 2011; 2018). One hundred thirty time-diagnostic artifacts, mostly projectile points, define these zones. The ages generated using the OSL method at the Friedkin site correlate with the known age of these time-diagnostic artifacts and cultural time periods. The samples collected for this study encompass the Pre-Clovis Buttermilk Creek Complex (below 90.32 m AD), Clovis and Folsom (90.32-90.40 m AD), and Late Paleoindian (above 90.40 m AD) zones. The Younger Dryas boundary is found within the zone with Clovis and Folsom artifacts. Clovis dates from 13,050 to 12,750 cal yr B.P. and Folsom from 12,750-12,000 cal yr B.P. (Waters and Stafford, 2014; Waters et al., 2020). In this part of the site, Clovis artifacts are found below and above 90.35 m AD, the zone identified as the base of the Younger Dryas. Also at 90.35 m AD, two Clovis projectile points were found. The presence of Clovis, Folsom, and Late Paleoindian time-diagnostic artifacts in these deposits agrees with the OSL ages and position of the Younger Dryas basal boundary.

3.3 Sampling, analytical methods and age model construction

3.2.1 Sampling

The sampling procedure at the Friedkin site adopted a similar approach taken by Sun et al. (2020) at the Hall's Cave site. Sample collection was conducted primarily on the south wall of the excavation unit. The depth used to describe all samples is elevation to an arbitrary datum originally established at the upstream Gault site (Waters et al., 2018). The sampling sequence is from 90.32~90.55 m AD crossing the YD boundary base (Waters et al., 2011). The base of YD boundary layer is located at 90.35 m AD. The sampling interval is 1-2 cm between consecutive samples along a 22 cm long sequence. The elevation used in this study describing each sample represent the center of each sample layer. A non-metallic spatula and sample containers were used to avoid metal contamination. In total, 17 samples spanning across this vertical column were collected at the Friedkin site.

3.2.2 Analytical Methods

3.2.2.1 Os isotope ratios and HSE abundance measurements

All chemical procedures and measurements in this study were at the University of Houston. No metal tools were used for processing or transferring samples during any stage of the sampling, chemical, and analytical procedures. The samples were processed and analyzed in duplicate. The sediments were dehydrated and then weighed targeting ~ 1 g for Os isotope and HSE analyses. Prior to transferring each sample aliquot into a Carius tube (CT), an enriched in ^{99}Ru, ^{105}Pd, ^{185}Re, ^{190}Os, ^{191}Ir, and ^{194}Pt spike was added. Reverse aqua regia was then added following similar procedures to Shirey and Walker (1995). The CT's were heated to 240 °C for

48 hours. Osmium was then extracted from the sample solutions using $CHCl_3$, followed by back extraction into 9 N HBr. The residue was then microdistilled with a CrO_3 - H_2SO_4 solution and collected in 9 N HBr (Birck et al., 1997).

Osmium isotope compositions were determined using a thermal ionization mass spectrometer in negative mode on a secondary electron multiplier using peak hopping mode. Repeated measurements of UMD Johnson Matthey Os standard yielded $^{187}Os/^{188}Os$ of 0.11382 ± 0.00021 (± 2σ, n = 9) which is consistent with the accepted value of 0.11380 ± 0.00026 reported by Brandon et al. (1999). Measured isotopic ratios were corrected for isobaric oxygen interference, instrument mass fractionation ($^{192}Os/^{188}Os$ = 3.083), procedural blank contribution, and spike contribution. Uncertainties were obtained through the error propagation of uncertainties in blank abundance and isotopic composition, spike abundance values, mass spectrometry measurements of Os, and the reproducibility of the Os isotopic values of the standard. Average procedural blank was 4.12 ± 0.21 pg/g for Os with $^{187}Os/^{188}Os$ = 0.12 ± 0.01 (2σ, n = 9).

The residual solutions after Os removal contains all of the other HSE. The solutions were dried at ~80 °C. This was followed by dissolution in 6N HCl, then taken to dryness again. This step was repeated twice to ensure full conversion to chloride form. The HSE were purified using ion exchange chromatography. The sample solutions were passed through Eichrom AG 1X8 100-200 mesh anion resin following a modified procedure from Day et al. (2016). The HSE fractions were collected and then dried down, then converted to chloride form by redissolving in HCl. The HSE fractions were then further purified using Eichrom AG50X-8 100-200 mesh cation resin following the procedure of Puchtel and Humayun (2001). This was repeated to ensure interference elements were removed for the HSE fractions.

The HSE isotopes were measured in an Agilent 8800 Triple Quadrupole ICP-MS. The Ru, Pd, Pt, and Re isotopes were measured in a NH_3 carrier gas, whereas Ir isotopes were measured in a He carrier gas. This procedure insured minimization of isotopic interferences while maximizing signal intensities. Mass fractionation factors were determined by sample/standard bracketing using a standard of natural isotopic composition and then applying the obtained exponential mass fractionation factor to the sample measurements. Over the course of the analytical campaign, reproducibility on 1 ppb of a mixed PGE standard of natural isotopic composition was better than 2% (2σ) for the isotopic ratios used for isotope dilution calculations ($^{185}Re/^{187}Re$: 0.5974 $^{191}Ir/^{193}Ir$: 0.5949 $^{194}Pt/^{195}Pt$: 0.9744, $^{100}Ru/^{101}Ru$: 0.7479, $^{106}Pd/^{105}Pd$:1.2238). Procedural blanks were 6.1 ± 0.3 pg for Ir, 12.4 ± 0.62 pg for Ru, 93.7 ± 4.7 pg for Pt, 8.6 ± 0.43 pg for Pd and 14.9 ± 5.7 pg for Re (2σ, n = 6).

Trace element measurements

A total of 40 sediment samples from Hall's Cave and 17 sediment samples from the Debra L. Friedkin site were processed for trace element measurement. About ~ 2 grams of each sample were crushed to fine powder in an alumina mortar and pestle. The mortar and pestle were pre-cleaned by repeatedly grinding with Ottawa quartz sand in ethanol. The sample powders were digested with mixed acids using a slightly modified method described by Gao et al. (2009). 100 mg of each sample was dissolved in 1 mL of 16 N HNO_3 and 2 mL of HF in Savillex PFA beakers. The samples were then dried down several times and redissolved in different amounts of HF, HCl, and HNO_3 (Gao et al., 2009). The final dissolution was in 8 N HNO_3 and dried down at a temperature of 100°C for 5–12 hours to ensure samples were in complete solution. Afterwards, the clear sample solutions were transferred into acid-cleaned, low-density polyethylene bottles

and diluted with Milli-Q H_2O to a dilution factor of 1:1000. The trace elements were measured on an Agilent 8800 Triple Quadrupole ICP-MS. The United States Geological Survey (USGS) standards BHVO-2, SCO-1, SGR-1 were measured as unknowns to monitor the analytical precision and accuracy. The elements Ni, Ti, Cs, Rb, Ba, Th, U, Nb, Ta, La, Ce, Pb, Pr, Sr, P, Nd, Zr, Sm, Eu, Gd, Tb, Dy, Ho, Er, Tm, Y, Yb, and Lu were analyzed. Analytical accuracy represented by the difference between analyzed and referenced concentrations is generally better than 5%, obtained by 10 replicate analyses of the USGS standards.

3.2.3 Chronology and Bayesian age model construction

Seventy-eight optically stimulated luminescence (OSL) dates, primarily collected from four separate stratigraphic columns in the floodplain sediments, provide chronological control at the Friedkin site. The OSL method precisely dates Late Quaternary sediments such as those in the Debra L. Friedkin site section, and yields accurate results (Waters et al., 2011; Forman and Waters, 2016). In this study, the chronostratigraphy was modeled using 16 OSL ages (Table 3.1, Waters et al., 2018). In order to construct the Bayesian age model, the OSL ages were input into OxCal software using a Poisson deposition model to compute an age-elevation profile (Bronk Ramsey, 2008; 2013). The age model did not detect an outlier. The modeled age profile was used to interpolate dates throughout the section (Figure 3.1). The modeled ages agree with the age of time-diagnostic projectile points found in the dated deposits (Waters et al., 2018).

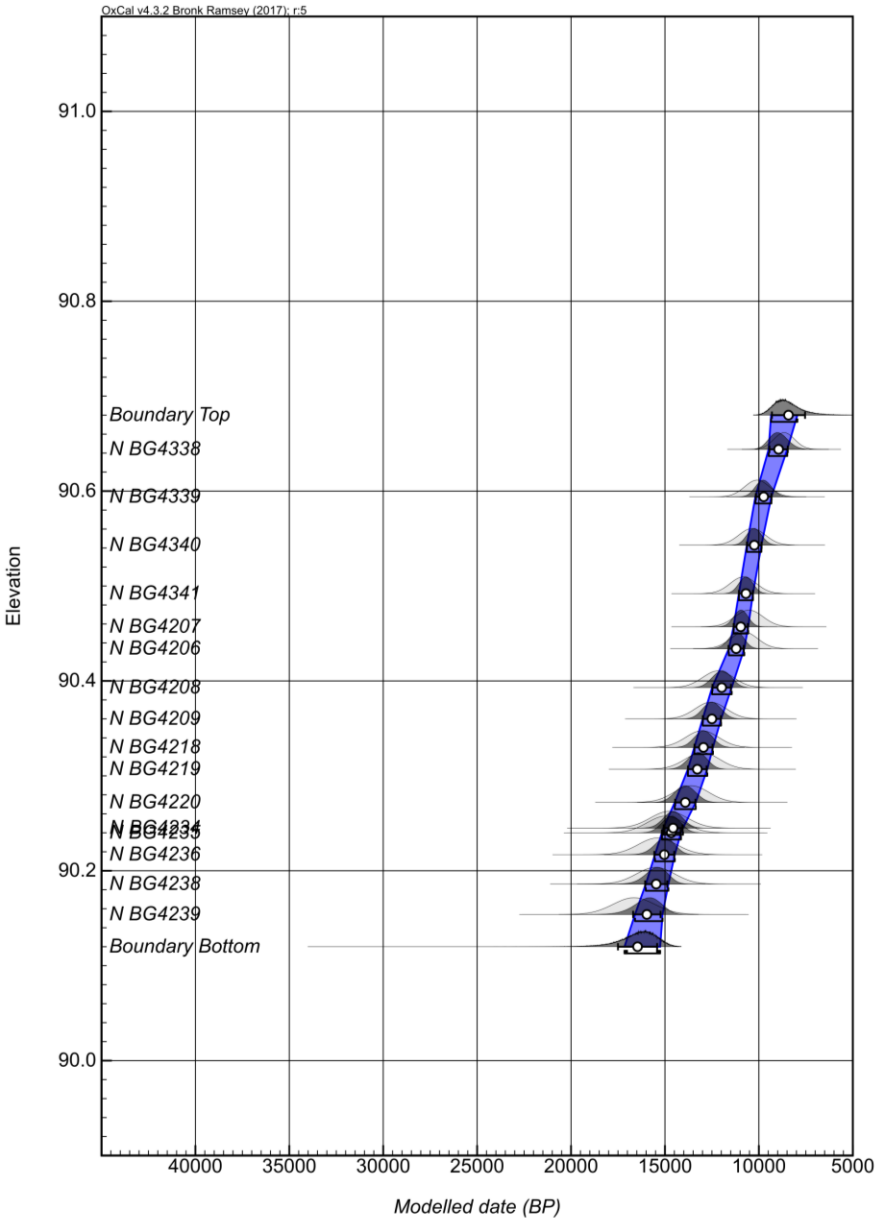

Figure 3.1 Bayesian analysis of the OSL ages for Friedkin site. The model was created in OxCal to identify outliers and compute posterior age estimates using a Poisson deposition model (Bronk Ramsey, 2008; 2013).

Table 3.1 Sixteen OSL ages from the 2016 core (Waters et al., 2018) for the construction of the Bayesian age model (Bronk Ramsey, 2009).

Sample	Elevation (m AD)	OSL ages (yr BP)	Standard Error	Modelled(CAL yr BP) From	To
BG4338	90.644	8655	550	9480	8490
BG4339	90.594	10095	655	10186	9335
BG4340	90.543	10360	705	10642	9866
BG4341	90.492	10830	695	11066	10315
BG4207	90.457	10530	750	11347	10567
BG4206	90.434	10785	715	11600	10777
BG4208	90.393	12170	820	12489	11448
BG4209	90.360	12560	830	12991	12012
BG4218	90.330	13020	870	13437	12445
BG4219	90.307	13010	905	13779	12747
BG4220	90.272	13595	930	14478	13362
BG4234	90.245	14790	985	15085	14041
BG4235	90.240	14965	985	15162	14147
BG4236	90.217	15400	1015	15532	14476
BG4238	90.186	15500	1020	16020	14816
BG4239	90.154	16650	1110	16594	15129

3.4 Results

3.4.1 Os isotope and HSE abundances for the Debra L. Friedkin site samples

The Os isotope and HSE measurements were conducted twice on each of the 17 samples, to total 34 data points for the entire stratigraphic sequence (Table 3.2). The deposition ages for the sampling sequence range from 10.25 to 13.06 ka. The base of YD boundary is located at elevation 90.35 m AD, which is bracketed between 12.5 ± 0.48 ka and 12.95 ± 0.48 ka. Bulk sediments at the Friedkin site have a variation in Os total abundances from 12.6-1985 ppt and $^{187}Os/^{188}Os$ ratios range from 0.119-2.128. The data can be divided into two groups based on Os abundances and $^{187}Os/^{188}Os$ ratios. The first group (hereon 'unradiogenic') contains nine

sediments spanning the sampling column, having unradiogenic $^{187}Os/^{188}Os$ of 0.119-0.565 and with Os abundances ranging from 46-1985 ppt. The second group (hereon 'radiogenic') comprise the rest of the data, preserving with $^{187}Os/^{188}Os$ of 0.620-2.128, and much lower Os abundances ranging from of 12.6-41.1 ppt. There are seven unradiogenic Os sediment layers at Friedkin site occurring above, within, and below the YD boundary base layer (Figure 3.2).

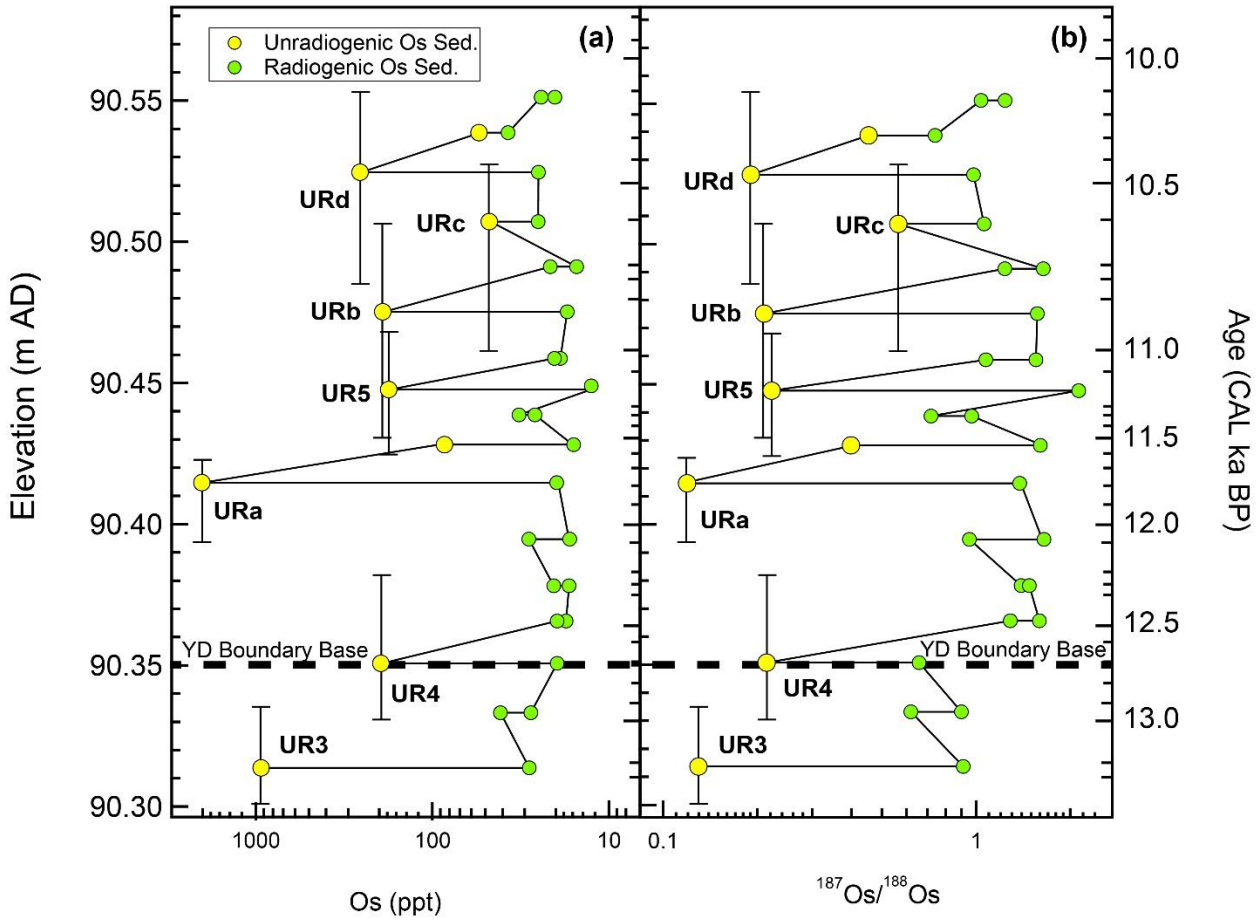

Figure 3.2 Elevation above datum profiles against total Os abundances (ppt) and $^{187}Os/^{188}Os$ ratios of Friedkin site sample section. (a) Elevation versus total Os abundances (ppt), (b) Elevation versus $^{187}Os/^{188}Os$ ratios. UR is unradiogenic. Arbitrary datum used in this study was referred to (Waters et al., 2011). Nine OSL ages were used for Poisson deposition model (Bronk Ramsey, 2008, 2013), intermediate depth-age pairs were extracted from the model. The error bars represent calculated age range at each corresponding depth using Bayesian age model by OxCal version 4.2 (Bronk Ramsey, 2013, Figure 3.1).

Table 3.2 Os isotopic ratios and HSE abundances for bulk sediments at the Friedkin site, Texas

Sample*	Elevation (m AD)	Modelled Age# (CAL ka BP)	$^{187}Os/^{188}Os$	±2σ	Os (ppt)	Ir (ppt)	Ru (ppt)	Pt (ppt)	Pd (ppt)	Re (ppt)
BMC16_01	90.55	10.25	1.24	0.07	20.2	14.5	52.3	270.6	163.4	265.5
BMC16_01.D	90.55	10.25	1.04	0.05	24.1	29	41.9	110.9	5.5	227.1
BMC16_02	90.54	10.26	0.74	0.02	37.2	23.5	112.9		421.7	484.9
BMC16_02.D	90.54	10.26	0.45	0.01	53.5	11.8	19	115.1	146.7	215.9
BMC16_03	90.53	10.39	0.19	0	252.1	6.9	19.4	329.1	232.3	119.7
BMC16_03.D	90.53	10.39	0.98	0.05	25	1.5	9.7		392.4	149.8
BMC16_04	90.51	10.59	1.06	0.05	25.1	14	11.6	201	247.9	159.5
BMC16_04.D	90.51	10.59	0.57	0.01	46.7	7.2	16.8	231.5	128.7	137
BMC16_05	90.49	10.69	1.64	0.14	15.2	17.1	21.6	200.1	130.4	130.5
BMC16_05.D	90.49	10.69	1.24	0.06	21.5	20.6	32	198.6	129.8	217.6
BMC16_06	90.48	10.94	0.21	0	187.9					
BMC16_06.D	90.48	10.94	1.57	0.11	17.2	5	11.6	191.4	201.3	205.1
BMC16_07	90.46	10.97	1.56	0.1	18.8	11	174.6	940.8	26.7	167.5
BMC16_07.D	90.46	10.97	1.07	0.06	20.3	3.1		407.5	99.2	100.9
BMC16_08	90.45	11.12	0.22	0	173.5	35	63.2	689.3	124	55.1
BMC16_08.D	90.45	11.12	2.13	0.26	12.6	17.1	0.9	526	259.5	143.6
BMC16_09	90.44	11.21	0.72	0.03	32.3	8.1	17.8	201.7	337.2	141.9
BMC16_09.D	90.44	11.21	0.97	0.04	26.3	22.7	12.7	155.3	53.3	149.4
BMC16_10	90.43	11.54	0.4	0.01	83.8	10.9	20.1	262.6	235.7	209.7
BMC16_10.D	90.43	11.54	1.6	0.12	15.8	3.9	12.2	453.9		160
BMC16_11	90.42	11.69	1.38	0.09	19.7	13.6	30.1	442.3	20.6	113.5
BMC16_11.D	90.42	11.69	0.12	0	1985.3	0.2	17.4	387.3	229.5	149.8
BMC16_12	90.4	11.98	1.65	0.12	16.6	8.7	43.9	212.1	151.1	203.1
BMC16_12.D	90.4	11.98	0.95	0.04	28.4	14.5	10.5	182.5		144.5
BMC16_13	90.38	12.22	1.39	0.08	20.5	8.5	19.9	504.8	343.2	179.8
BMC16_13.D	90.38	12.22	1.48	0.1	16.8	3.6	20.4	148.5	1129.6	187.1
BMC16_14	90.37	12.63	1.59	0.11	17.5	9.3	16.3	172.2	260.5	186.4
BMC16_14.D	90.37	12.63	1.29	0.08	19.6	0.6	15.4	34.8	59.8	198.2
BMC16_15	90.35	12.7	0.21	0	192.3	12.8	8.7	310.2	26.9	160.9
BMC16_15.D	90.35	12.7	0.66	0.02	19.6	1.7	8.5	62.1		108.5
BMC16_16	90.33	12.95	0.9	0.04	27.6	10.3		114.1		182.2
BMC16_16.D	90.33	12.95	0.62	0.02	41.1	3.3	34.7	398.8	14.5	185.8
BMC16_17	90.32	13.06	0.91	0.04	28.2	12.7	42.2	293.2	0	97.5
BMC16_17.D	90.32	13.06	0.13	0	917.9	10.1	23.9	90.7	81.5	173.3

With exception of Os for the unradiogenic $^{187}Os/^{188}Os$ group data, the samples have HSE abundances on average that are similar to or only lower than upper continental crust (UCC) which contains on average 31 ppt of Os, 22 ppt of Ir, 30 ppt of Ru, 599 ppt of Pt, 526 ppt of Pd, 198 ppt of Re (Esser and Turekian, 1993; Park et al., 2012). The CI chondrite-normalized HSE patterns for the radiogenic $^{187}Os/^{188}Os$ group for the samples from the Friedkin site show a compositional range that fluctuate around, and encompasses UCC values with similar shaped patterns (Figure 3.3). The unradiogenic $^{187}Os/^{188}Os$ group data are similar apart from having distinctly higher Os abundances that result in distinct HSE-normalized patterns relative to UCC or the radiogenic $^{187}Os/^{188}Os$ group data.

3.4.2 Trace element abundances for the Debra L. Friedkin site and Hall's Cave samples

Trace element abundances in the Friedkin and Hall's Cave sites are presented in Table 3.3. Both sites have similar trace element abundances to upper continental crust (Gromet et al., 1984; Condie, 1993; Gaschnig et al., 2016). All samples display Ba, Sr, and Nb-Ta negative anomalies, as well as positive La and Pb anomalies in primitive mantle-normalized plots (Figure 3.4). However, the two sites have distinct differences in P abundances. The P abundance of 210-289 ppm in the sediment samples from the Friedkin site is about two order of magnitude less than that of Hall's Cave with 2010-18021 ppm. The REE abundances normalized to primitive mantle (Anders and Grevesse, 1989) show an enrichment in LREE relative to HREE with a Eu negative anomaly (Figure 3.5). The unradiogenic and radiogenic Os sediment groups for both sites are indistinguishable with respect to REE.

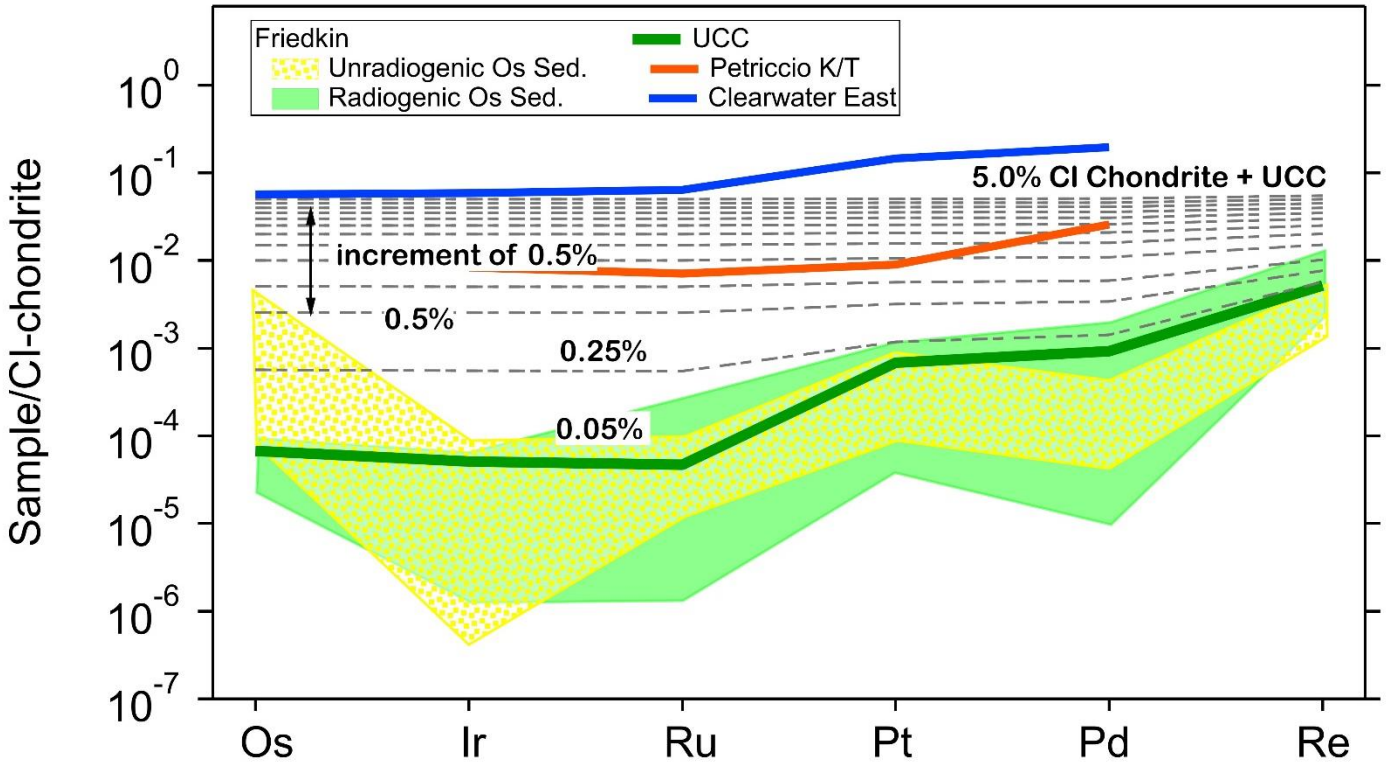

Figure 3.3 CI chondrite-normalized incremental mixing model of CI chondrite material into an upper continental crust–like target. From 0.5 – 5.0 % mixing lines use 0.5% increment, beneath are the 0.05% and 0.25% lines. HSE patterns of Friedkin site Unradiogenic Os sediments (yellow dotted pattern) and Radiogenic Os sediments (green shadow), compared with average upper continental curst (UCC) (Esser and Turekian, 1993; Park et al., 2012), Clearwater East Impact melt rock, Canada (Evans et al., 1993; McDonald, 2002), Petriccio K/T boundary, Italy (Evans et al., 1993). Cl-chondrite values used for normalization are from Wasson and Kallemeyn (1988).

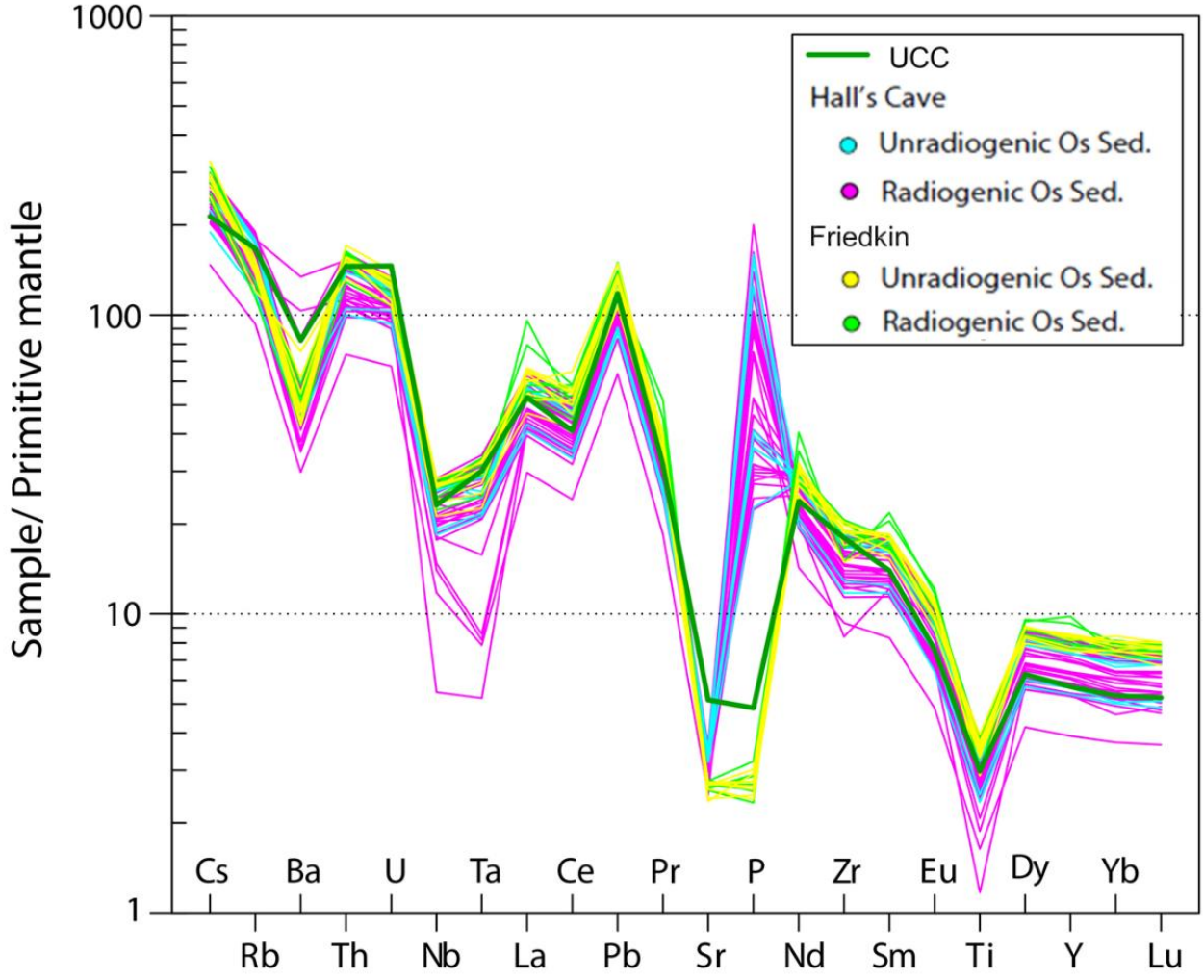

Figure 3.4 Spectrum of rare earth elements normalized to the primitive mantle of (McDonough and Sun, 1995) for average upper continental curst (UCC), Friedkin site and Hall's Cave samples.

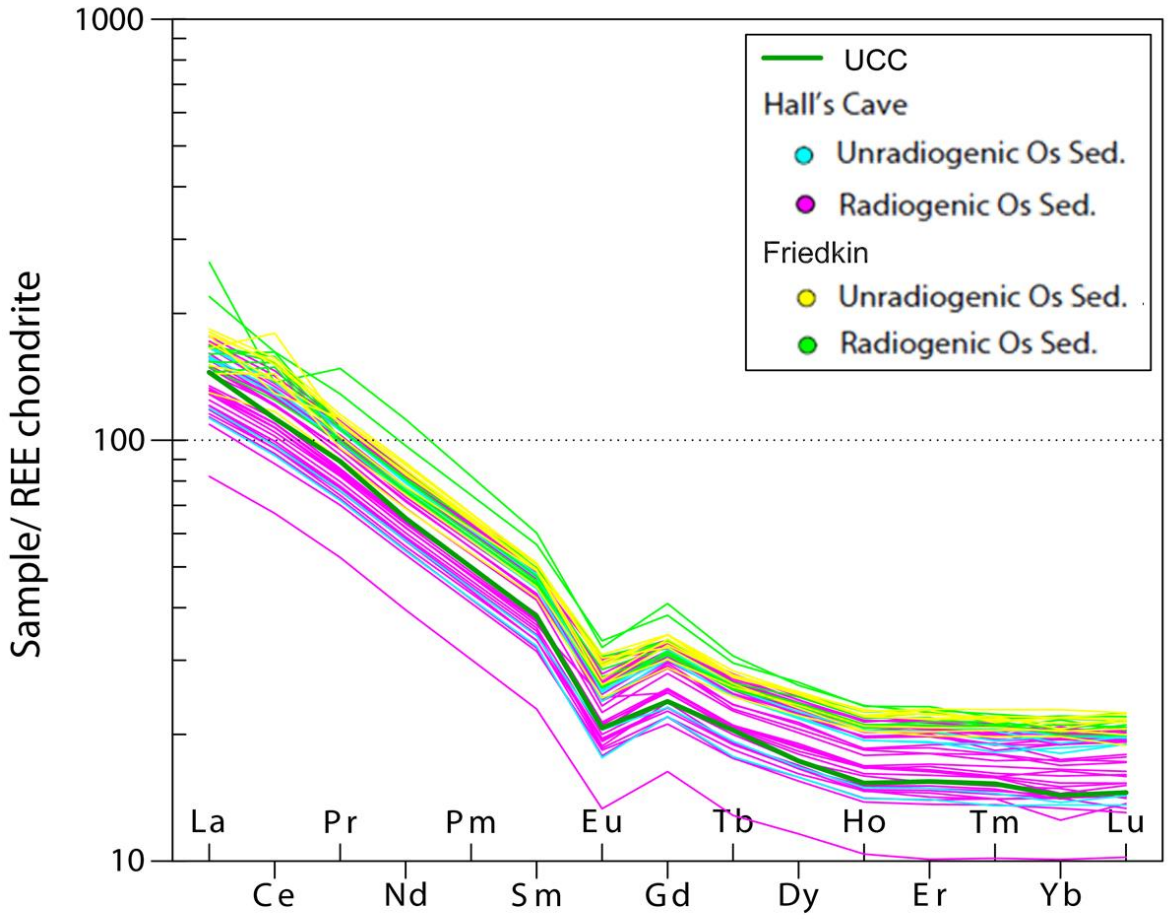

Figure 3.5 Spectrum of rare earth elements normalized to the chondrites (Anders and Grevesse, 1989) for average upper continental crust (UCC), Friedkin site and Hall's Cave samples.

Table 3.3 Trace element abundances (parts per million, ppm) for bulk sediments from the Friedkin site and Hall' Cave, Texas.

Sample	Ni	Ti	Cs	Rb	Ba	Th	U	Nb	Ta	La	Ce	Pb	Pr	Sr
BMC16_01.D	25.56	3591	5.09	68.77	280.7	10.30	2.15	14.61	0.91	62.10	82.68	18.00	13.19	51.13
BMC16_02.D	30.76	4754	6.85	91.97	319.0	13.65	2.82	18.67	1.18	35.32	84.01	20.27	9.09	53.39
BMC16_03.D	24.31	4342	6.07	81.95	281.0	12.50	2.62	17.47	1.10	41.52	77.90	18.43	10.07	53.32
BMC16_04.D	35.46	4024	6.07	84.47	405.4	12.17	2.25	15.81	1.01	43.07	94.50	19.98	10.26	51.63
BMC16_05.D	30.30	4646	6.59	90.12	320.3	13.08	2.54	18.43	1.12	33.98	89.94	20.43	8.83	52.02
BMC16_06.D	23.50	3989	6.10	84.75	294.1	12.46	2.23	15.50	0.94	30.42	70.54	15.99	8.02	48.07
BMC16_07.D	37.04	4488	6.30	87.26	364.0	12.55	2.51	18.00	1.10	36.01	92.10	21.05	9.01	51.99
BMC16_08.D	44.04	3467	5.23	72.34	497.8	10.60	2.15	13.96	0.84	38.77	108.27	22.32	9.68	47.08
BMC16_09.D	25.69	4575	6.28	89.96	293.4	12.74	2.61	18.50	1.16	35.02	75.16	17.66	8.84	53.28
BMC16_10.D	29.78	4502	6.21	89.01	324.7	12.47	2.46	17.94	1.09	33.79	86.68	19.84	8.53	53.59
BMC16_11.D	33.93	4159	5.97	86.10	361.4	12.52	2.51	17.67	1.09	42.42	91.27	20.12	10.05	54.20
BMC16_12.D	34.53	4265	5.85	84.04	352.4	12.05	2.63	17.34	1.08	39.07	92.71	20.88	9.46	53.25
BMC16_13.D	39.20	4562	6.18	88.89	385.6	12.86	2.60	17.86	1.23	39.22	95.17	21.17	9.77	54.96
BMC16_14.D	29.58	4419	6.05	87.60	335.0	12.91	2.61	17.90	1.21	37.61	97.61	22.50	9.47	53.71
BMC16_15.D	27.37	4353	5.95	85.47	311.2	12.51	2.67	17.44	1.13	39.93	83.60	19.40	9.82	54.43
BMC16_16.D	34.87	3947	5.39	76.36	353.6	11.56	2.38	16.16	1.11	51.49	97.75	20.02	11.47	55.24
BMC16_17.D	32.93	4243	5.70	84.70	360.7	12.51	2.55	17.38	1.20	41.66	92.77	20.45	10.06	54.50
HC15_05	20.99	3708	5.16	91.61	302.6	9.93	2.12	15.33	0.79	33.78	73.44	17.19	8.22	63.25
HC15_06	22.92	4323	6.15	107.2	341.5	11.74	2.48	18.17	0.91	39.28	83.20	19.82	9.57	64.04
HC15_07	22.62	4272	5.99	105.9	343.0	11.63	2.43	17.88	0.95	38.88	82.83	19.47	9.40	64.80
HC15_08	20.84	3852	5.46	97.23	361.6	10.76	2.22	16.01	0.92	34.91	72.67	18.04	8.48	64.66
HC15_09	22.26	4222	5.97	106.6	364.5	11.97	2.34	17.75	1.06	39.00	82.61	20.25	9.39	65.04
HC15_10	22.13	4124	5.76	104.4	380.4	11.68	2.30	17.54	1.05	37.15	79.10	19.58	8.95	69.71
HC15_11	18.80	3408	4.94	91.6	314.3	10.07	1.94	13.98	0.87	31.60	67.84	15.53	7.63	67.33
HC15_12	20.48	3262	4.66	85.9	290.7	9.83	2.14	13.44	0.77	31.20	66.20	15.57	7.56	66.65
HC15_13	18.94	2831	3.97	71.68	287.8	8.01	1.86	12.10	0.78	26.48	55.45	13.14	6.41	69.17
HC15_14	20.70	3086	4.25	80.1	248.8	8.95	1.89	13.12	0.82	28.32	60.00	14.33	6.93	67.37
HC15_15	23.78	4365	6.08	111.5	361.5	12.33	2.40	18.09	1.12	39.51	82.26	20.27	9.52	66.16
HC15_16	13.97	1972	3.09	55.9	196.4	5.90	1.35	7.74	0.29	19.26	40.43	9.54	4.69	49.19
HC15_17	19.38	2920	4.32	76.2	237.1	8.55	1.80	12.25	0.79	26.64	56.07	13.62	6.47	65.85
HC15_18	19.33	3075	4.52	79.7	331.8	8.61	1.98	12.92	0.85	28.34	58.99	13.98	6.85	72.43
HC15_42	17.30	2497	4.48	79.5	295.8	8.69	1.80	9.71	0.32	28.38	59.95	13.85	6.89	58.72
HC16_01	22.50	4256	6.25	107.7	885.8	12.19	2.60	17.53	1.04	38.92	80.88	19.85	9.45	67.15
HC16_02	23.52	4154	5.93	104.0	333.2	11.75	2.26	16.99	1.09	37.02	79.56	19.07	9.12	66.20
HC16_03	22.85	4064	6.02	105.7	318.2	12.04	2.34	17.07	1.06	37.08	79.76	19.63	9.03	63.45
HC16_04	20.75	4132	5.93	106.1	312.7	11.70	2.25	16.93	1.07	36.37	76.02	18.84	8.85	63.16
HC16_05	22.95	4332	6.08	109.3	331.5	12.67	2.52	18.05	1.18	39.34	83.12	20.32	9.57	66.33
HC16_06	23.77	4354	5.97	109.5	327.4	12.68	2.52	18.21	1.15	39.44	82.28	20.46	9.51	68.03
HC16_07	23.36	4507	6.14	113.9	336.8	12.73	2.51	18.49	1.18	40.08	83.48	20.70	9.81	67.53
HC16_08	20.46	3837	5.63	104.8	311.7	12.14	2.19	16.06	1.00	37.76	76.37	18.19	9.16	62.67
HC16_09	24.42	4544	5.92	110.6	342.1	12.68	2.66	18.34	1.19	39.86	83.56	20.42	9.64	67.87
HC16_10	23.37	4079	5.22	100.8	312.3	11.58	2.30	16.93	1.07	36.75	77.43	18.72	8.86	69.67
HC16_11	23.72	4589	5.74	110.5	556.1	12.94	2.68	18.68	1.26	41.38	88.16	21.05	9.89	64.74
HC16_12	19.34	4156	5.07	93.96	313.8	11.29	2.36	16.74	1.10	35.22	76.50	18.51	8.73	54.05
HC16_13	25.81	4504	5.98	107.5	375.4	12.79	2.64	18.51	1.20	40.35	85.68	20.79	9.79	67.32
HC16_14	18.84	3298	4.48	82.50	271.9	9.33	1.98	13.74	0.89	30.70	64.72	14.73	7.40	71.08
HC16_15	20.52	3436	4.72	86.29	297.4	9.54	2.11	14.22	0.92	30.87	66.05	15.37	7.48	69.80
HC16_16	20.33	3312	4.65	83.15	282.3	9.26	2.12	13.79	0.89	30.27	64.59	15.26	7.33	67.17
HC16_17	18.60	2963	4.57	78.34	291.9	8.95	2.01	11.92	0.58	29.23	61.66	13.87	7.10	64.43
HC16_18	22.69	3159	4.82	80.46	681.7	9.01	2.30	13.60	0.83	30.16	63.05	14.81	7.32	72.23
HC16_19	19.09	3000	4.71	77.46	361.9	8.41	2.06	12.56	0.80	27.94	58.56	13.65	6.75	70.17
HC16_20	19.95	2258	4.47	75.59	306.3	8.49	2.11	9.21	0.30	27.73	57.58	13.47	6.74	72.19
HC16_21	19.74	1411	4.63	76.06	289.6	8.22	2.05	3.60	0.19	27.10	57.69	13.41	6.59	70.41
HC16_22	19.12	2836	4.44	72.38	229.7	7.86	1.94	11.64	0.77	25.60	53.01	12.51	6.25	70.42
HC17_01	19.84	3690	5.31	95.4	347.4	10.64	2.29	15.33	1.01	35.39	73.34	17.24	8.50	72.17
HC17_39	27.14	3997	5.81	104.1	340.9	11.30	2.50	16.25	1.02	36.94	78.28	18.50	8.90	67.02
HC17_44	20.12	3876	5.72	104.3	299.2	11.07	2.50	15.99	0.90	36.51	77.62	18.39	8.77	66.56

Table 3.3 Trace element abundances (parts per million, ppm) for bulk sediments from the Friedkin site and Hall' Cave, Texas (continued).

Sample	P	Nd	Zr	Sm	Eu	Gd	Tb	Dy	Ho	Er	Tm	Y	Yb	Lu
BMC16_01.D	210.4	50.67	157.0	8.85	1.80	8.04	1.11	6.35	1.30	3.58	0.52	42.19	3.23	0.48
BMC16_02.D	271.5	35.07	213.0	7.20	1.47	6.41	1.00	6.13	1.26	3.65	0.55	35.20	3.72	0.55
BMC16_03.D	247.9	38.55	200.4	7.26	1.52	6.62	1.00	6.03	1.22	3.47	0.53	36.73	3.57	0.53
BMC16_04.D	215.8	40.00	178.5	7.47	1.64	6.78	0.99	6.06	1.23	3.45	0.53	36.29	3.45	0.52
BMC16_05.D	258.1	34.36	199.6	6.68	1.45	6.06	0.93	5.67	1.15	3.31	0.51	33.10	3.29	0.51
BMC16_06.D	222.7	31.09	184.6	6.21	1.37	5.66	0.89	5.38	1.13	3.22	0.50	32.30	3.33	0.49
BMC16_07.D	261.4	35.02	189.2	6.81	1.53	6.11	0.95	5.76	1.17	3.34	0.50	33.32	3.52	0.50
BMC16_08.D	263.1	37.89	156.3	7.21	1.70	6.32	0.96	5.60	1.13	3.15	0.48	32.53	3.21	0.46
BMC16_09.D	242.0	34.08	211.3	6.72	1.44	6.20	0.93	5.75	1.17	3.41	0.52	34.27	3.34	0.52
BMC16_10.D	239.0	33.59	198.2	6.59	1.47	5.93	0.94	5.69	1.17	3.30	0.50	33.33	3.31	0.50
BMC16_11.D	246.4	39.48	199.0	7.51	1.66	6.79	1.03	6.10	1.27	3.54	0.53	36.22	3.35	0.53
BMC16_12.D	232.6	36.44	199.8	6.99	1.60	6.32	0.96	5.96	1.22	3.48	0.51	35.55	3.42	0.51
BMC16_13.D	289.2	37.93	216.5	7.31	1.71	6.55	1.00	6.10	1.26	3.63	0.54	35.85	3.55	0.55
BMC16_14.D	247.9	36.71	199.7	7.46	1.65	6.55	0.99	6.06	1.22	3.57	0.53	34.98	3.59	0.54
BMC16_15.D	247.4	37.42	195.4	7.51	1.62	6.51	1.00	6.10	1.23	3.56	0.52	36.12	3.55	0.53
BMC16_16.D	229.3	43.89	174.2	8.31	1.87	7.55	1.07	6.45	1.30	3.70	0.53	39.96	3.54	0.52
BMC16_17.D	232.4	38.55	207.8	7.43	1.73	6.79	1.01	6.08	1.23	3.63	0.52	35.90	3.57	0.54
HC15_05	2193	31.17	162.4	6.13	1.26	5.49	0.83	4.90	0.99	2.86	0.43	29.88	2.74	0.42
HC15_06	3693	36.05	187.0	7.08	1.41	6.24	0.95	5.64	1.16	3.31	0.49	34.19	3.10	0.48
HC15_07	3237	35.78	193.3	6.95	1.44	6.18	0.94	5.66	1.15	3.31	0.50	34.18	3.23	0.48
HC15_08	3169	32.33	165.0	6.35	1.34	5.65	0.86	5.12	1.03	3.00	0.46	30.88	2.83	0.44
HC15_09	2831	36.00	184.4	6.97	1.48	6.21	0.96	5.63	1.13	3.31	0.48	33.92	3.07	0.48
HC15_10	3457	34.29	191.4	6.64	1.39	6.05	0.93	5.57	1.13	3.25	0.49	33.62	3.25	0.48
HC15_11	6766	29.14	146.4	5.64	1.16	5.00	0.76	4.62	0.94	2.70	0.41	27.51	2.68	0.40
HC15_12	9285	29.13	151.7	5.63	1.15	5.03	0.76	4.51	0.93	2.60	0.38	27.04	2.66	0.39
HC15_13	11253	24.66	123.3	4.77	0.99	4.34	0.64	3.84	0.78	2.23	0.33	23.13	2.21	0.33
HC15_14	7935	26.66	135.0	5.18	1.05	4.69	0.69	4.04	0.84	2.36	0.36	24.46	2.33	0.35
HC15_15	2834	36.17	185.2	7.08	1.46	6.41	0.96	5.57	1.17	3.27	0.48	33.83	3.39	0.48
HC15_16	6604	17.87	97.9	3.38	0.75	3.21	0.47	2.82	0.58	1.60	0.25	16.78	1.64	0.25
HC15_17	4751	24.80	129.3	4.72	1.00	4.33	0.64	3.76	0.77	2.17	0.33	22.79	2.17	0.32
HC15_18	9216	26.37	132.2	5.08	1.08	4.56	0.70	4.02	0.81	2.31	0.34	24.37	2.30	0.35
HC15_42	8705	26.05	127.6	5.07	1.10	4.55	0.69	4.10	0.82	2.34	0.35	24.56	2.30	0.36
HC16_01	4161	36.21	186.2	7.03	1.67	6.30	0.96	5.70	1.16	3.29	0.47	34.51	3.18	0.47
HC16_02	2624	34.92	174.5	6.88	1.44	6.14	0.93	5.41	1.10	3.19	0.44	31.73	3.08	0.47
HC16_03	2042	34.80	178.7	6.82	1.45	6.18	0.93	5.50	1.14	3.23	0.47	32.66	3.22	0.48
HC16_04	2010	33.84	177.3	6.70	1.36	5.86	0.91	5.32	1.10	3.17	0.46	31.51	3.16	0.47
HC16_05	2675	36.91	190.4	7.14	1.48	6.53	0.97	5.78	1.20	3.42	0.49	34.15	3.44	0.50
HC16_06	3715	36.55	197.5	7.16	1.49	6.44	0.97	5.67	1.15	3.32	0.49	34.09	3.35	0.50
HC16_07	2751	37.16	188.3	7.20	1.49	6.47	0.98	5.87	1.19	3.47	0.51	35.12	3.32	0.50
HC16_08	2849	35.07	162.5	6.91	1.48	6.15	0.93	5.49	1.13	3.22	0.47	33.23	3.16	0.47
HC16_09	4728	37.17	194.6	7.25	1.52	6.48	0.96	5.75	1.16	3.29	0.48	34.55	3.16	0.49
HC16_10	3565	33.82	179.2	6.53	1.34	5.92	0.89	5.29	1.08	3.03	0.46	32.02	2.93	0.46
HC16_11	3520	38.10	193.4	7.48	1.69	6.59	1.01	5.98	1.23	3.41	0.51	35.48	3.26	0.51
HC16_12	2451	33.14	167.9	6.57	1.31	5.80	0.85	5.18	1.03	2.95	0.43	30.14	2.80	0.43
HC16_13	2513	37.98	191.1	7.23	1.56	6.50	1.00	5.85	1.20	3.38	0.50	35.42	3.23	0.49
HC16_14	7781	28.62	143.0	5.49	1.18	5.01	0.76	4.56	0.93	2.62	0.39	27.11	2.49	0.37
HC16_15	8970	28.91	153.9	5.69	1.20	5.05	0.76	4.54	0.92	2.67	0.39	27.23	2.59	0.39
HC16_16	11216	27.99	153.6	5.45	1.19	4.94	0.75	4.43	0.93	2.59	0.38	26.35	2.44	0.37
HC16_17	10575	27.24	139.5	5.26	1.12	4.70	0.73	4.18	0.89	2.44	0.36	25.21	2.42	0.34
HC16_18	18022	28.08	140.0	5.35	1.37	4.94	0.74	4.36	0.90	2.54	0.38	26.00	2.35	0.37
HC16_19	14344	26.12	135.2	5.04	1.15	4.55	0.70	4.06	0.83	2.37	0.35	24.29	2.24	0.35
HC16_20	14604	26.08	137.0	4.91	1.09	4.47	0.69	4.04	0.84	2.40	0.36	24.30	2.28	0.36
HC16_21	12567	25.30	88.0	4.92	1.04	4.33	0.67	3.91	0.82	2.26	0.34	23.34	2.29	0.32
HC16_22	8517	24.15	119.5	4.63	1.03	4.16	0.64	3.84	0.78	2.22	0.34	22.96	2.03	0.33
HC17_01	8285	32.59	170.7	6.29	1.36	5.72	0.83	5.00	1.02	2.86	0.42	29.62	2.83	0.42
HC17_39	11181	34.32	181.0	6.67	1.41	6.02	0.91	5.45	1.09	3.14	0.46	32.93	3.07	0.47
HC17_44	13633	33.74	174.8	6.66	1.42	5.94	0.89	5.34	1.08	3.05	0.44	31.71	3.02	0.46

3.5 Discussion

3.5.1 Nugget effect on Os abundances and $^{187}Os/^{188}Os$ ratios

In both the Friedkin site and Hall's Cave sediments, there is within sample heterogeneity in HSE abundances and $^{187}Os/^{188}Os$ ratios. This is shown in the duplicates of each sample from the Friedkin site (Table 3.2), and those from Hall's Cave (Sun et al., 2020). For example, for the two fractions measured for sample BMC16-02, the Os abundances are 37.2 and 53.5 ppt and the $^{187}Os/^{188}Os$ ratios are 0.74 and 0.45, respectively. For BMC16-04, the Os abundances are 25.1 and 46.7 ppt and the $^{187}Os/^{188}Os$ ratios are 1.06 and 0.57, respectively. Similar variation is observed in all the Friedkin site samples (Table 3.1). The nugget effect in HSE is well known in many types of Earth materials because of the inhomogeneous distribution within for example, microscopic-sized grains such as sulfides and alloys (Shirey and Walker, 1998). In the case of the Hall's Cave and Friedkin site samples, if the Sun et al. (2020) hypothesis is viable that these reflect cryptotephra with Os-rich aerosol coatings, then the nugget effect may be produced by grain distribution during depositional processes. In this study and in Sun et al. (2020), ~50g sediment samples were each directly taken from the stratigraphic sections, and as noted above, were not processed further with the exception of drying to remove excess water and careful hand handpicking removal of mm to cm-sized limestone fragments, where present. Small, 1-2 gram fractions of the dried loose, material were processed for each sample including duplicates. Another approach would have been to homogenize each sample by grinding into a fine powder and performing extensive mixing operations of the powder in a vial, but this could have potentially diluted information on the HSE. This dilution may be borne out by the data from other North American and European locales at the YD basal boundary measured by Paquay et

al., (2009). Unlike the approach in Sun et al. (2020) and here, Paquay et al., (2009) processed 6 to 10 grams of homogenized powder for each sample measured for HSE abundances and $^{187}Os/^{188}Os$ ratios. . Using that technique, Os abundances ranged from 2 to 435 ppt, and the $^{187}Os/^{188}Os$ ratios ranged from 0.90 to 1.67. Paquay et al., (2009) observed some variability of samples taken from the same YD layer at the same locales, but only at Howard Bay (North Carolina) did any sample have $^{187}Os/^{188}Os$ ratios below 1, at 0.9, trending toward mantle-like values and trending away from the crust-like values of >1 at the locales they studied. Although not conclusive, it is possible that the sample nugget effect of the HSE were homogenized in their samples such that the potentially small amount of the mantle-like component was diluted to t be unrecognized in the larger, homogenized, sample sizes. Whereas the sample treatment used therein and in Sun et al. (2020), preserved isotopic variability in smaller sample sizes and reduced to negated isotopic homogenization of the samples (Paquay et al., 2009)

To test this hypothesis the following analyses was performed. Sediment from the Hall's Cave site yielded seven unradiogenic Os sediments spanning across the sampling sequence (Sun et al., 2020). One of these, sample HC15-07 was divided into fine-, medium-, and coarse-grained particles (Figure 3.6), to determine the effect on the distribution of Os and $^{187}Os/^{188}Os$ ratios. The diameters for the three fractions are < 0.66 mm, ~ 1.18mm, and > 2.36mm, respectively. The bulk sediment fraction measured in Sun et al. (2020) has an Os abundance of 4478 ppt and unradiogenic $^{187}Os/^{188}Os$ ratio of 0.12. The Os results of fine-, medium- and coarse-grained fractions are listed in Table 3.4. Three fractions have Os abundances ranging from 22.26 - 27.85ppt, and $^{187}Os/^{188}Os$ of 1.40-2.22, similar to those of upper continental crust, being 31 ppt and 1.05 (Peucker-Ehrenbrink and Jahn, 2001). Coarse- and fine-grained samples have very similar Os abundances and $^{187}Os/^{188}Os$ values. There is a good correlation between the bulk

sediment and 3 size fractions between $^{187}Os/^{188}Os$ and $1/^{192}Os$ (Figure 3.7). A mixing line between the fractions derived by linear regression has an R^2 of 0.994.

Table 3.4 $^{187}Os/^{188}Os$ and Os total abundances of fine-, medium- and coarse- grained fractions, and bulk sediment of sample HC15-07 from Hall's Cave.

Sample	$^{187}Os/^{188}Os$	Os (ppt)	^{192}Os (ppt)
HC15-07C	2.14	22.05	6.59
HC15-07M	1.40	27.85	9.20
HC15-07F	2.22	22.26	5.99
HC15-07B	0.12	4478	1835

This test in a single sample exhibits the heterogeneity of radiogenic and unradiogenic Os distribution and deposition at any given time in the Hall's Cave sediments. The measured sample weights are ~ 1 g, and thus consistent with the variations that are likely due to "nugget effect" on these amounts of sediment measured, observed in the sediment duplicates from Hall's Cave (Sun et al., 2020), and the Friedkin site (Table 3.2). It raises an interesting issue as to the transfer mechanism and resident form of Os in these loose sediments that will be further discussed below.

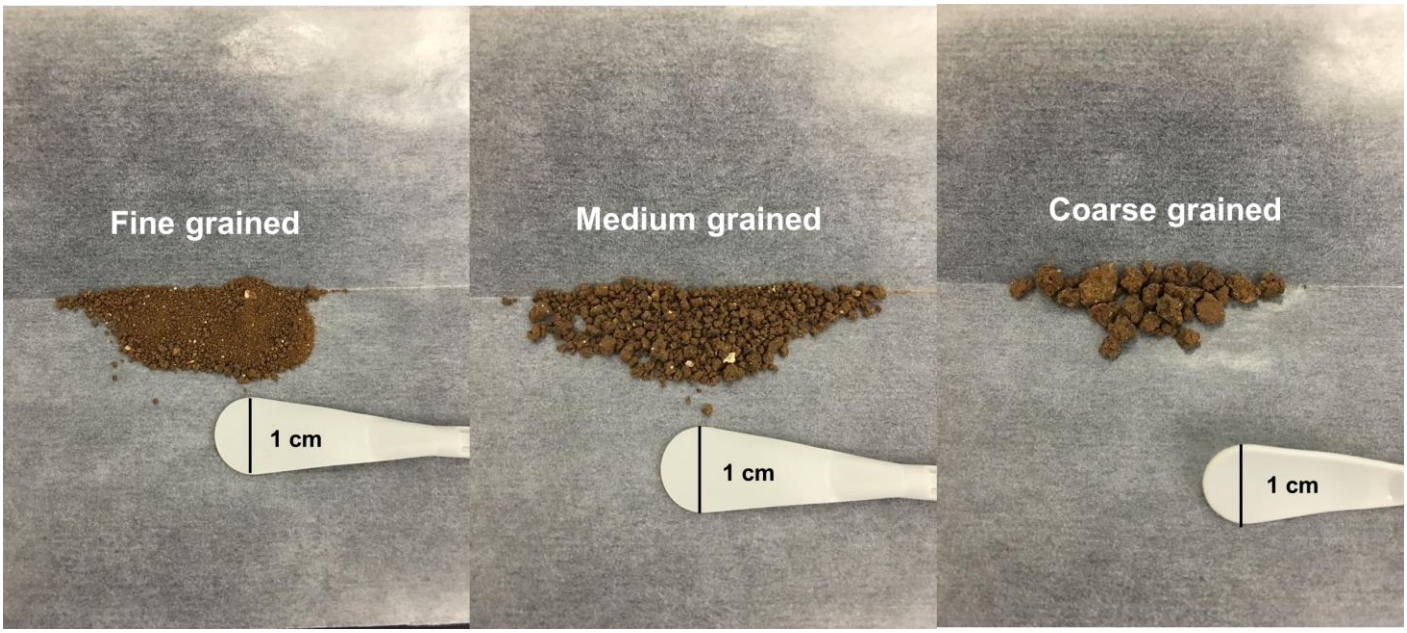

Figure 3.6 Fine-, medium- and coarse-grained aggregate fractions of sample HC15-07 at Hall's Cave.

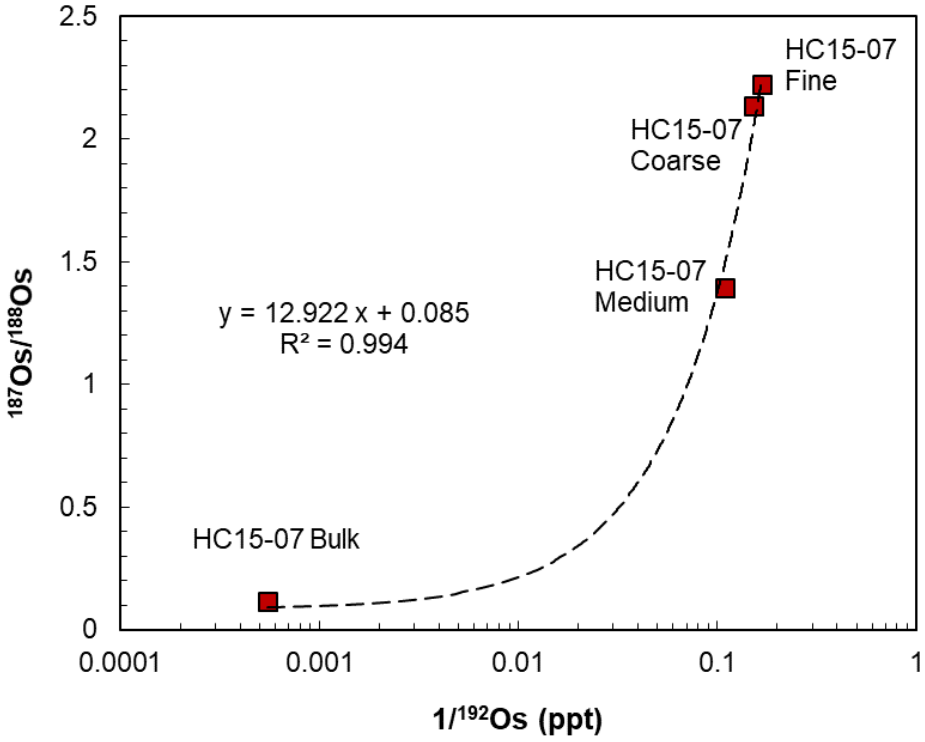

Figure 3.7 Osmium isotope results of fine-, medium- and coarse-grained aggregate fractions of sample HC15-07 at Hall's Cave.

3.5.2 Extra-terrestrial versus Volcanic Origin of $^{187}Os/^{188}Os$ and HSE Variations at the Debra L. Friedkin site

At the Friedkin site, unradiogenic Os peaks occur periodically in the vertical sequence (Figure 3.2). Six Os isotope peaks occur above, one peak within, and another one below YD boundary level. Over ca. 3000 years span of deposition of the studied section. This distribution of Os isotopic peaks is similar to the Hall's Cave sequence, with 5 unradiogenic Os peaks occurring above and below the YD level from 10.9-13.3 ka (Sun et al., 2020). It is unlikely that meteoritic Os input could have admixed into local crustal materials so frequently, every few

hundred to thousands of years from 10.25 to13.3 ka to yield Os excursions for Hall's Cave and Friedkin sites. A bolide source is equally implausible with the CI chondrite-normalized HSE patterns for Hall's Cave (Sun et al., 2020) and the Friedkin site (Figure 3.3). Mixtures of HSE of CI chondrite and UCC demonstrate that the unradiogenic and radiogenic Os groups is discordant, with the CI-normalized signature of the Friedkin site samples, even with as little as 0.05% addition of a CI chondrite (Figure 3.3). The higher percentage of CI chondrite mixed into UCC, the more consistent is the mixed profiles, with larger deviations from the Friedkin site patterns. Previously reported Clearwater East Impact melt rock from Canada, Petriccio K/T boundary and Italy would have similarity with <2 % mixing model lines (Evans et al., 1993; McDonald, 2002). The elemental data for other meteoritic materials, including enstatite chondrites, ordinary chondrites, carbonaceous chondrites and iron meteorites were also considered with incremental modeling with addition to UCC (Fig. S1 in Sun et al., 2020). The mixing models, using these materials, do not result in the HSE abundances observed in the Friedkin site samples. Therefore, the observed $^{187}Os/^{188}Os$ ratios and HSE abundances are inconsistent with contribution from an extraterrestrial impactor or bolide airburst.

Hence, a meteorite source is inconsistent for the elevated Os abundances and unradiogenic $^{187}Os/^{188}Os$ ratios relative to UCC. Instead, this systematics at Hall's Cave and the Friedkin site are likely of terrestrial origin. Wu et al. (2013) interpreted unradiogenic Os surface films on spherules from the Melrose, PA, boundary layer, with $^{187}Os/^{188}Os$ ratios from 0.112 to 0.120, to originate from a bolide as it ablated during heating in the Earth's atmosphere or as terrestrial material that was ejected back into the atmosphere and redeposited following the impact. The data is reevaluated by Sun et al. (2020) that most meteorites have $^{187}Os/^{188}Os$ ratios of ≥ 0.124, with a few ranging from 0.120 to 0.124, and two at 0.117 (Walker et al., 2002; Cook

et al., 2004; Brandon et al., 2005; Day et al., 2016; Goderis et al., 2017), and thus are unlikely to be the sources for the $^{187}Os/^{188}Os$ ratios in the spherule surface films. Instead, the large-scale volcanic eruption scenario (Sun et al. 2020) provided the scenario which could explain the frequent and episodic mantle-derived mass flux of Os in the Friedkin site and Hall's Cave sediments.

End-member mixing models were used to further test the volcanic scenario for the origin of Os isotopic variation. Osmium abundances and $^{187}Os/^{188}Os$ ratios were constrained for the mantle-like end-member as an explanation for the unradiogenic Os data for the Friedkin site. As with the Hall's Cave site data (Sun et al. 2020), the Friedkin site data plot along two-end member mixing curves for $^{187}Os/^{188}Os$ versus 1/Os (Figure 3.8). As with Hall's Cave data, the less radiogenic $^{187}Os/^{188}Os$ ratios and higher Os abundances of the Friedkin site samples lie between a mantle-like end member similar to spherule leachates, which were the surface films on the bulk spherules from Melrose, Pennsylvania YD locale (Wu et al., 2013) and upper continental crust (Figure 3.8). The radiogenic samples at Hall's Cave site have slightly higher $^{187}Os/^{188}Os$ ratios of ~ 2.35 than those for the Friedkin site at ~2.1. The spherule residues and bulk spherules scatter near the samples from the Friedkin and Hall's Cave sites. Four mixing models with different Os proportions and $^{187}Os/^{188}Os$ ratios of radiogenic Friedkin site crust and unradiogenic mantle-like Os (Table 3.5) are shown in Figure 3.8. In Mix 1, the average of the leachates for the Melrose Objects 2, 4, 5, 11, and 13 was used as the unradiogenic $^{187}Os/^{188}Os$ endmember (Figure 3.8). By mixing this surface film average from Melrose with Friedkin site crust of 22 ppt Os and $^{187}Os/^{188}Os$ of 1.2, the mixing curve passes through the unradiogenic and radiogenic Os samples from the YD layers at the Friedkin site and four of the unradiogenic samples coincide with the mean values. Three other mixing models were also plotted using end members varying from

1,000 to 20,000 ppt and $^{187}Os/^{188}Os$ ratios from 0.116 to 0.2. In Figure 3.8, the four hyperbolic mixing curves form a band that overlaps with all the Friedkin site sediments. This indicates that the different unradiogenic Os layers are likely the result of multiple sources having $^{187}Os/^{188}Os$ ratios of ~0.116 to 0.2 and were deposited at multiple times at the Friedkin site. This $^{187}Os/^{188}Os$ range for the unradiogenic Os end-member falls within the range of volcanic lavas and aerosol samples, such as lavas from the Cascade arc (0.129 to 0.253), ocean island lavas (0.110 to 0.176), and volcanic aerosols from Mauna Loa in Hawaii that have $^{187}Os/^{188}Os$ ratios of 0.136 to 0.140 (Krähenbühl et al., 1992; Borg et al., 2000; Day, 2013).

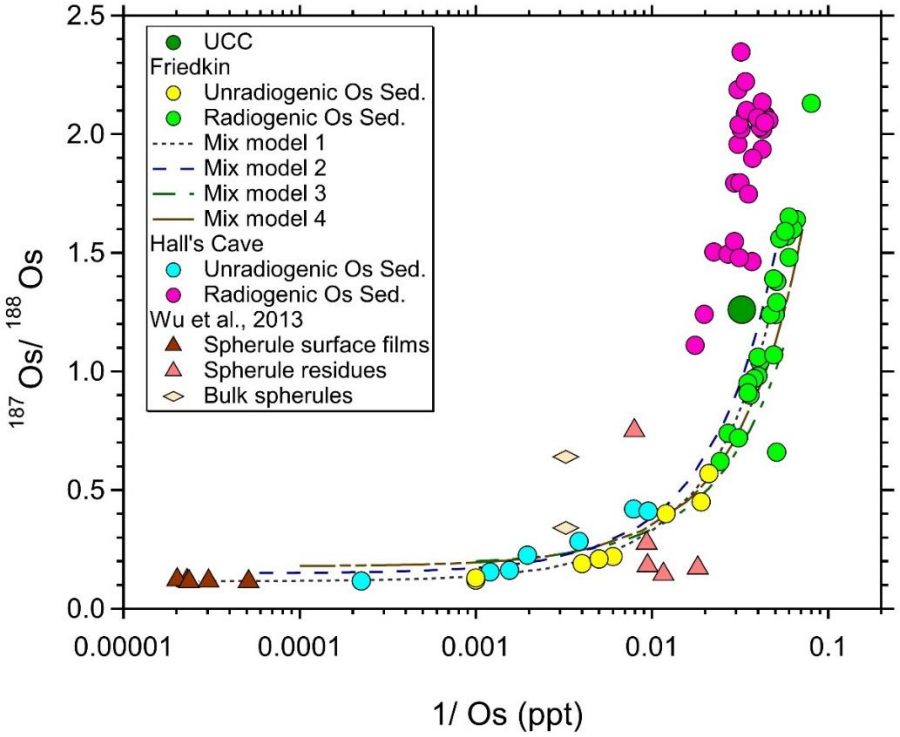

Figure 3.8 Osmium isotope results of Friedkin site and Hall's Cave and mixing models between Friedkin site local crust and mantle-like Os end-members. UCC is upper continental crust (Esser and Turekian, 1993), data for bulk sediments, bulk spherules and spherule surface films and residues were for the Melrose (PA) YD site from Wu et al. (2013).

Table 3.5 The Os concentrations and $^{187}Os/^{188}Os$ ratios of the end member components for the mass balance mixing models for Friedkin site samples.

Mixing model	Unradiogenic Os Component		Friedkin Crust	
	Os ppt	$^{187}Os/^{188}Os$	Os ppt	$^{187}Os/^{188}Os$
Mix 1	37529	0.116	22	1.2
Mix 2	20000	0.150	20	1.5
Mix 3	1000	0.200	18	1.1
Mix 4	10000	0.180	14	1.6

The required Os abundances for the mantle-like end member of ≥1,000 ppt are much higher than values measured in lavas from effusive eruptions, which typically have Os abundances less than 100 ppt (Day, 2013). Instead, the rich Os values observed at the Friedkin and Hall's Cave sites are more similar to Os concentrations found on aerosols formed during explosive volcanic eruptions.

In addition, the HSE CI-normalized patterns of the Kudryavy volcano gas condensates, Kurile Islands closely match the HSE CI-normalized patterns for Friedkin site unradiogenic Os samples, with the exception of Re (Figure 3.9) (Yudovskaya et al. 2008). Pt, Ir, Os, and Pd systematics at the Friedkin and Hall's Cave sites also closely match the values from gas condensates from the Kudryavy volcano and two other volcanoes, Tolbachik, Kamchatka, and Erta Ale, Ethiopia (Figure 3.10) (Yudovskaya et al., 2008; Zelenski et al., 2013; Chaplygin et al., 2016). The Friedkin site sediments do not fall within the fields of MORB, OIB, volcanic arcs, or komatiites (Woodland et al., 2002; Ireland et al., 2009; Day et al., 2010; Bézos et al., 2005; Gannoun et al., 2007; Yang et al., 2014; Tagle, 2005; Puchtel et al., 2004; Puchtel et al., 2005; Puchtel et al., 2008; Connolly et al., 2011).

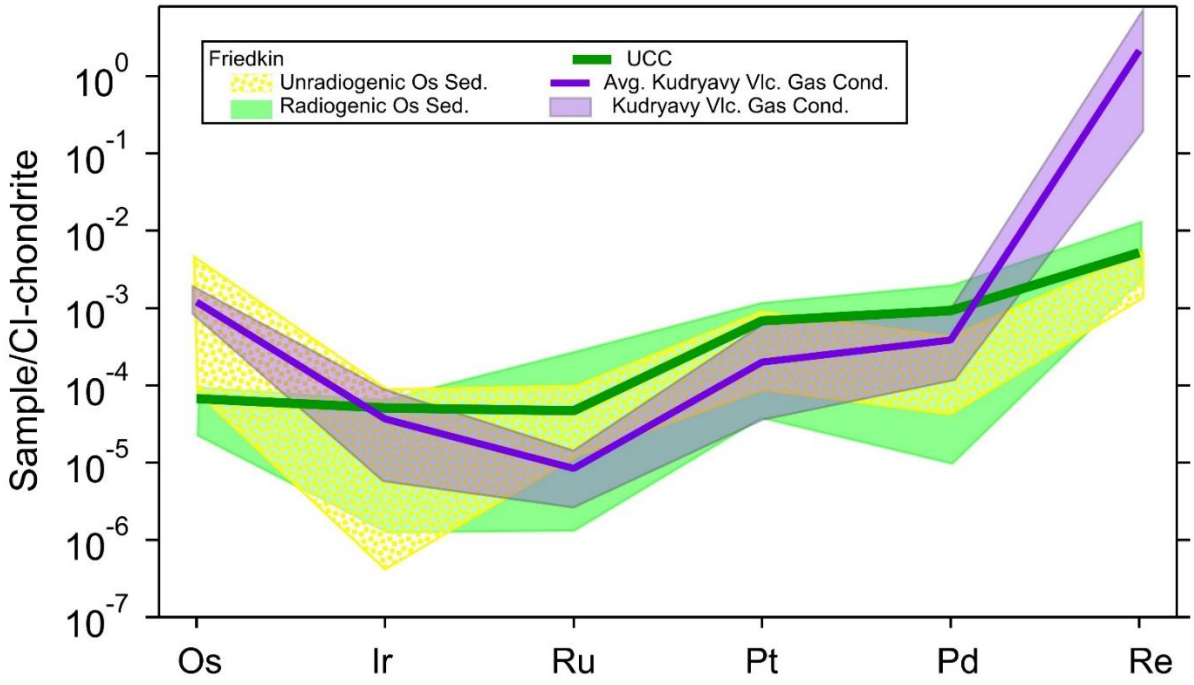

Figure 3.9 CI chondrite-normalized HSE patterns of all gas condensates and the average of the Kudryavy volcano gas condensates, Kurile Islands. UCC is short for upper continental crust (Esser and Turekian, 1993; Park et al., 2012). The HSE patterns for the Os isotope radiogenic and unradiogenic groups are in green shadow and yellow dotted pattern, respectively. All Kudryavy volcano gas condensates (abbreviated to Vlc. Gas Cond.) Kudryavy volcano gas condensates (Yudovskaya et al., 2008) are plotted as purple shadow whose average is presented as the dark purple line. Cl-chondrite values used for normalization are from Wasson and Kallemeyn, (1988).

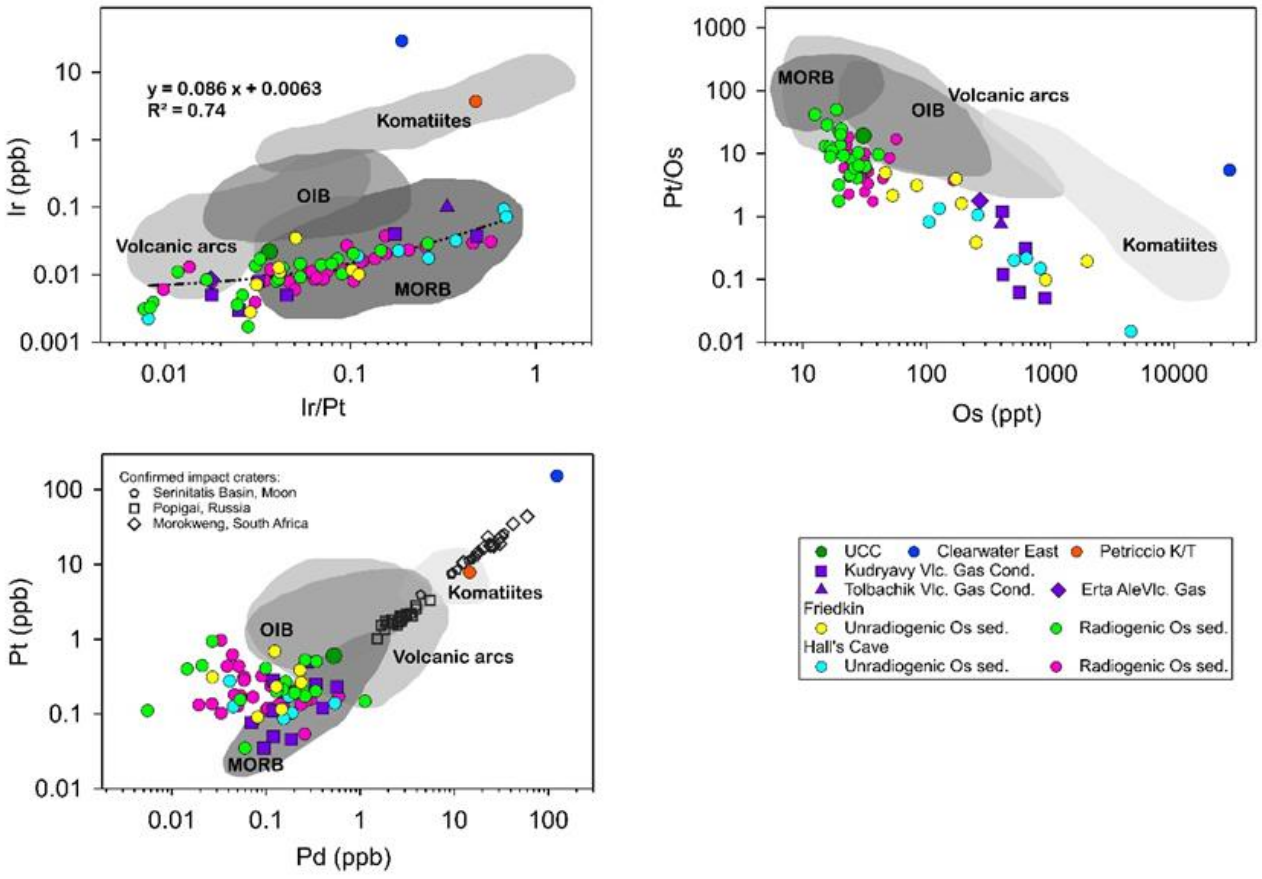

Figure 3.10 Binary plots of HSE elements and ratios for the Friedkin and Hall's Cave samples. Compared to upper continental crust (Esser and Turekian, 1993; Park et al., 2012), Clearwater East Impact melt rock, Canada (Evans et al., 1993; McDonald, 2002), Petriccio K/T boundary, Italy (Evans et al., 1993), Kudryavy volcano gas condensates, Kurile Islands (Yudovskaya et al., 2008), Tolbachik volcano gas condensate, Kamchatka (Chaplygin et al., 2016), Erta Ale volcano gas (abbreviated to Vlc. Gas), Ethiopia (Zelenski et al., 2013) and confirmed impact craters, Popigai, Russia (Tagle and Claeys, 2005), Morokweng, South Africa (McDonald et al., 2001), Serenitatis basin, Moon (Tagle, 2005), MORB (Bézos et al., 2005; Gannoun et al., 2007; Yang et al., 2014), OIB (Ireland et al., 2009; Day et al., 2010), Volcanic arcs (Woodland et al., 2002), komatiites (Puchtel et al., 2004, 2005, 2008; Connolly et al., 2011). (a) Ir versus Ir/Pt, (b) Pt/Os versus Os. (c) Pt versus Pd. See text for more information.

Friedkin site unradiogenic Os samples present Re abundances that do not match values previously measured in volcanic aerosols, albeit analyses of this kind are rare. This is also the case for the Halls Cave unradiogenic Os samples (Sun et al. 2020). The Kudryavy volcano gas

condensates have more than two orders of magnitude higher Re abundances than do UCC and Friedkin site sediments (Figure 3.9). A possible scenario is that the Re enrichment is not reflected at the Friedkin site, because HSE strongly fractionated during volatile phase transport and with aerosol condensation (Lassiter and Luhr, 2001). Rhenium and Os are the two HSE that show the highest enrichments in volcanic aerosols (Figure 3.9), such that these elements may quickly reach concentration levels, that would result in condensation into a solid phase. Depending on the conditions in the eruptive column, it is likely that HSE will condense into different phases and strongly fractionate from each other as the material is aerially transported away from the eruptive center. For example HSE-rich minerals have been identified in aerosol condensates forming at different temperatures, such as rhenite (ReS_2), K-Re-perrhenate, and those for Pt-Pd and Os alloys (Yudovskaya et al., 2008). From volcano to volcano, variability in cooling rates and dispersal may subsequently cause the variation in HSE content within the evolved aerosols (Yudovskaya et al., 2008; Zelenski et al., 2013; Chaplygin et al., 2016). Because Os and Re are the most enriched in aerosols by orders of magnitude (Figure 3.9), they will be the easiest to recognize in depositional sites at a distance from the eruptive centers. Hence, the observation that two depositional sites in central Texas show the highly similar Os enrichments but lack Re enrichments indicative of volcanic aerosols, is consistent with the volcanic source.

Volcanic eruptions often release volatiles such as CO_2, H_2O, SO_2, H_2S, HCl and HF exsolve from magma. The HSE will strongly partition to the vapor phase from the melt and adhere to volcanic aerosols in the eruption column because they have melt-vapor partition coefficients of 10^5 to 10^6 (Oppenheimer et al., 2011; Brenan et al., 2016; Yudovskaya et al., 2008; Gannoun et al., 2015). The HSE partitioning process may be augmented by an increasing

solubility of sulfur and an increasing oxidation state of the magma during decompression (Oppenheimer et al., 2011; Brenan et al., 2016). The distribution of HSE in volcanic aerosols with transport away from the eruptive center is related to the eruption magnitude. The higher a volcanic eruption plume rises in the troposphere, the further volcanic aerosols will be dispersed. Therefore, in very large eruptions, entrained aerosols of HSE can be transported and deposited > 1000 km from source (Watson et al., 2016).

3.5.3 Comparison of the Unradiogenic $^{187}Os/^{188}Os$ Time Horizons between Hall's Cave and Debra L. Friedkin site

Distant volcanic eruptions may provide the source material to yield periodically recurring HSE-fingerprint in distinct layers at the Friedkin site and Hall's Cave (Sun et al., 2020). Eruptions with magnitudes > 5 on Volcanic Explosivity Index (VEI) aerosols are dispersed in to the stratosphere and distribute on a global scale (Robock, 2000). In Figure 3.11, the modeled age values are relative to their differences from the corresponding Younger Dryas onset ages for comparison, 12.9 ka at Hall's Cave and 12.7 ka at the Friedkin site. The five unradiogenic Os horizons at Hall's Cave reflect cryptotephra with aerosol condensates (Figure 3.11). These are grouped into three volcanic mixing events that correlate well with known eruptions (Sun et al., 2020). At the Friedkin site, the seven unradiogenic Os horizons are identified in the sediment sequence (Figures 3.2 and 3.11). These are labeled as UR3-5, which correlate well with the UR3-5 peaks at Hall's Cave. UR4 at the Younger Dryas is a particularly strong match between sites.

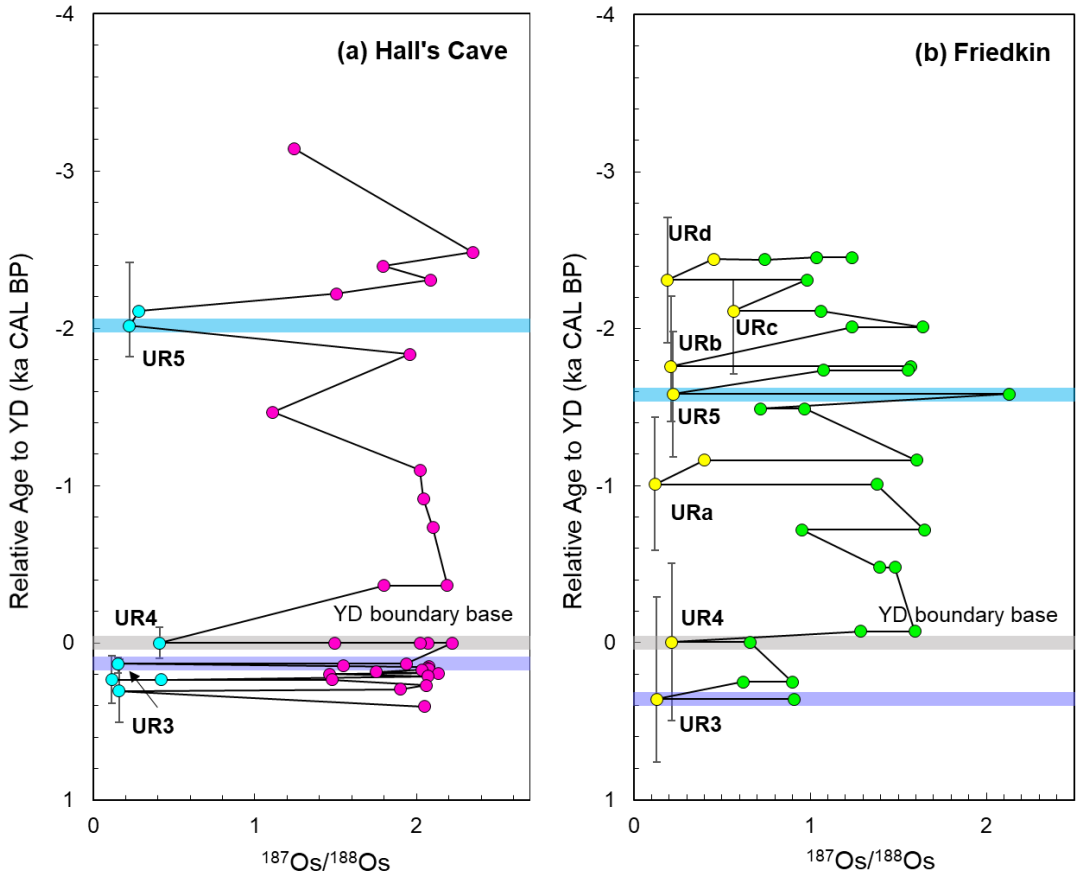

Figure 3.11 Correlation of unradiogenic Os isotope peaks detected at Hall's Cave and the Friedkin site. (a) Age model for Hall's Cave; (b) age model calculated by the OSL-16 column (Waters et al. 2012) at the Friedkin site. Age values are normalized by subtracting the corresponding Younger Dryas onset ages at each study site, 12.9 ka at Hall's Cave and 12.7 ka at the Friedkin site. The error bars represent calculated age range at each corresponding depth using Bayesian age model by OxCal version 4.2 (Bronk Ramsey, 2009). UR3, UR4 and UR5 peaks observed at Hall's Cave could be correlated with the same color-banded peaks UR3, UR4 and UR5 at the Friedkin site.

Six unradiogenic horizons do not match. Each unique horizon can be attributed to sampling at the Friedkin site. First, the samples collected from the section at the Friedkin site represent a shorter time interval of ~2000 years (10.1 to 13.1 ka) than at Hall's Cave of ~3700

years (9.7 to 13.4 ka). Hence, the two oldest unradiogenic Os peaks at Hall's Cave are older than the section at the Friedkin site. Four additional unradiogenic Os horizons are identified at the Friedkin site that within the same time interval as the sediments preserved at Hall's Cave (samples URa, URb, URc, URd in Figure 3.11 and Table 3.2). Sediments were collected with tighter spatial and temporal resolution at the Friedkin site. Equivalent unradiogenic horizons likely occur at Hall's Cave, but they were missed by coarser sampling strategy.

All the samples form a continuum of mixtures between the mantle-like component (i.e., cryptotephra and aerosol) and UCC (Figure 3.8). A cryptotephra should have broad distribution representing the age of eruption. However, isotopic enrichments may reflect the nugget effect and other diagenetic process. Nevertheless, at least three of the unradiogenic Os peaks correlate well between the two different sites that are located 240 km apart. Four unradiogenic Os horizons identified in the Friedkin site section remain unidentified in the Hall's Cave section.

The age versus $^{187}Os/^{188}Os$ and total Os diagrams (Figures 3.2 and 3.11), the representative modeled age of each sample was taken from the peak model age value in the probability density distribution using Bayesian analysis (Bronk Ramsey, 2008, 2013). The bandwidth of each modeled date at a given elevation in Figure 3.1 is used to generate age error bars for each sample at corresponding elevation in the $^{187}Os/^{188}Os$ and Os total abundances verse elevation profiles shown as Figure 3.2 and 3.11. The unradiogenic Os peaks, UR3, UR4 and UR5 at the Friedkin site section, are dated on average 13.1 ± 0.3 ka, 12.7 ± 0.5 ka and 11.1 ± 0.4 ka, respectively are in consecutive consistency with the UR3, UR4 and UR5 peaks at Hall's Cave site whose modeled ages are 13.1 ± 0.09 ka, 13.0 ± 0.1 ka and 10.9 ± 0.3 ka, respectively (Figures 3.11 and 3.12). Given the modeled age uncertainty, UR3 and UR4 may potentially represent an unradiogenic Os fluxing event sourced from the sulfur-rich phonolite magma

eruption from the Laacher See eruption of Eifel Volcano in Germany at 13.00 ± 0.10 ka (Ramsey et al., 2015; Table S5 in Sun et al., 2020). The large, VEI 6, Laacher See eruption is suggested to have induced aerosol cooling and long-lived amplified ocean circulation shifts and/or sea ice expansion over North Hemisphere at 13 ka (Schmincke et al., 1999; Baldini et al., 2018). The Laacher See eruption would have dispersed volcanic cryptotephra across the Northern Hemisphere. Importantly, the causality between a large volcanic eruption and the millennial-scale climate YD cooling event infers the influence of Laccher See eruption lasted ~200 years over North Atlantic region (Baldini et al., 2018).

The UR5 horizon at the Friedkin site profile with modeled age of 11.12 ± 0.42 ka or URb with modeled age of 10.94 ± 0.51 ka, may have been caused by the Fisher Tuff eruption from the Aleutian Arc at 10.66 ± 0.49 ka and/or the Lvinaya Past eruption from the Kuril Arc with eruption age of 10.48-10.78 ka (Bindeman et al., 2001; Stelling et al., 2005; Bazanova et al., 2016; Razzhigaeva et al., 2016; Smirnov et al., 2017; Sun et al., 2020, Table S5) or both eruptive events.

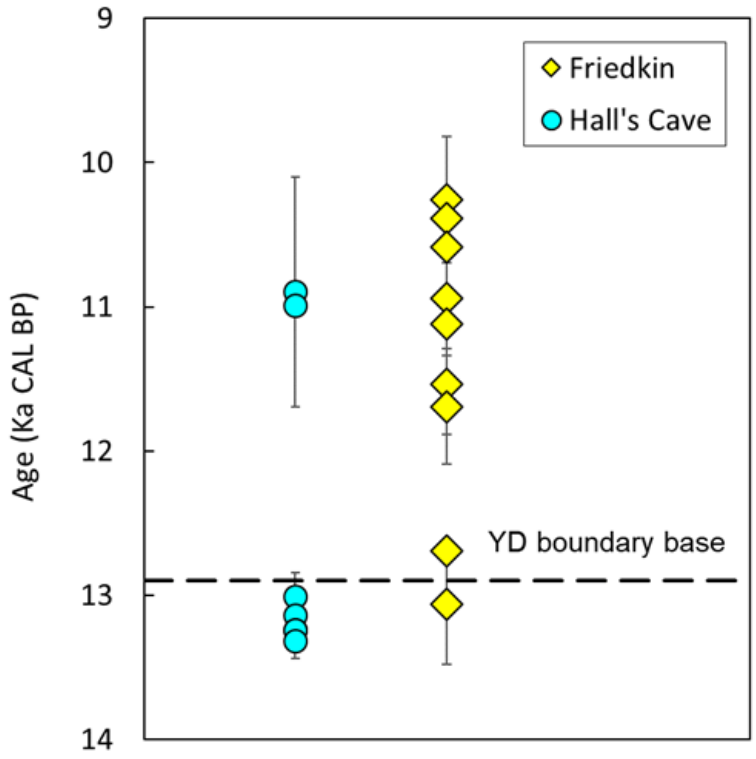

Figure 3.12 Age vs Age correlation of unradiogenic Os isotope peaks at Hall's Cave and the Friedkin sites. The age error bars are calculated based on the Bayesian age model by OxCal version 4.2 (Bronk Ramsey, 2009).

Among the Friedkin unradiogenic samples that do not specifically correlate to unradiogenic horizons at Hall's Cave, URa with a modeled age 11.69 ± 0.31 ka could potentially correlated with a distinct $^{187}Os/^{188}Os$ decrease to 1.11 at ca. 11.54 ka in between layers having $^{187}Os/^{188}Os$ ratios of 2.02 and 1.96, respectively at Hall's Cave (Figure 3.11). However, compared to the adjacent layers having $^{187}Os/^{188}Os$ of ~2, the ratio of 1.1 measured in this horizon could be considered as a significant decline and possible presence of the volcanic aerosol signature in diluted amounts for this sample. The distinct $^{187}Os/^{188}Os$ difference from 1.11 to ~2 may represent an unradiogenic $^{187}Os/^{188}Os$ input admixed into Hall's Cave local crustal materials

during this time. There is one possible Plinian volcanic eruption candidate for URa at the Friedkin site, and the possible decrease in $^{187}Os/^{188}Os$ at Hall's Cave. The Grímsvötn tephra series from Grimsvotn, Iceland occurred 12.26 to 11.41 ka (Jennings et al., 2014; Neave et al., 2015). Accordingly, six eruptions took place in the Grímsvötn volcanic system each ranging in volume from >1–30 km^3 and five of those dispersed westwards and one eruption directed eastward from the source vent (Jennings et al., 2014; Thordarson, 2014; Neave et al., 2015).

URc and URd at the Friedkin site are assigned an age of 10.59 ± 0.31 ka and 10.39 ± 0.42 ka, respectively. The possible tephra candidate for URc and URd is Longonot volcano, Kenya which erupted at 10.47 ± 0.21 ka which was a rather large event with a ~6.7 VEI (Clarke, 1990; Rogers et al., 2004; Macdonald and Scaillet, 2006). These two time horizons at the Friedkin site are not present at Hall's Cave sequence (Figure 3.11) possibly reflecting insufficient sampling between 116 and 131 cm at Hall's Cave which corresponds to ca. 9.8 to 10.5 ka (Sun et al., 2020), analyzed between depth of . There are three well-correlated layers between Hall's Cave and the Friedkin site which it is consistent with the proposed volcanic origin deduced from Os isotopic analysis.

3.5.4 Trace Element Test for a Volcanic Origin of Hall's Cave and Debra L. Friedkin site Os isotopic excursion

Siderophile elements such as Ni, Ir and Cr represent impactor-relevant elements that are characteristic of chondrite material relative to continental crust (Tagle and Hecht, 2006). Both Ir and Ni often exhibit similar local, geochemical relations in terrestrial crust following meteorite impacts (Paquay et al., 2009). In numerous craters, there is a clear positive correlation between Ni and Ir abundances (Figure 3.13), such as have been documented for Popigai crater, Siberia,

Morokweng crater, South Africa, Clearwater East impact structure, Canada and KT boundary from Stevens Klint, Caravaca (Palme et al., 1978; Alvarez et al., 1980; McDonald, 2002; Tagle and Claeys, 2005). In comparison, upper continental crust has much lower abundances of Ir and Ni with on average ~22 ppt and 26 ppm, respectively (Park et al., 2012; Gaschnig et al., 2016). In the impact YD study of Firestone et al., (2007), among previous impact evidence reported at multiple YD boundary sites across North America and Europe, Ir and Ni abundances in magnetic grains were elevated at YD boundary layers at sites across North America and Europe (Firestone et al., 2007). In the horizons below and above the YD, Ir and Ni were nearly undetectable. At five YD locales (Firestone et al., 2007), Blackwater Draw, NM, Wally's Beach, AB, Topper, SC, Lommel, Belgium YD the Ir-Ni abundances in magnetic grains have an inverse correlation, unlike those from five crater impactites that display a positive correlation in Figure 3.13.

The Ni abundances for sediment samples from the Friedkin site and Hall's Cave are between 14~44 ppm (Table 3.3). These values are similar to the average Ni abundance, 26 ppm in upper continental crust (Gaschnig et al., 2016). Both Ni and Ir do not show any significant enrichment above UCC at or near the YD boundary layer at both sites. Wu et al. (2013) also obtained UCC-like REE results for two magnetic spherules from the YD site at Melrose, PA. The REE abundances in the study are on the same order of magnitude with samples at the Friedkin and Hall's Cave sites.

The unradiogenic Os sediment groups at the Friedkin and Hall's Cave show a slightly negative coupling between Ir and Ni and deviate from the positive correlation of impact craters (Figure 3.13). Aerosol from the Erta Ale volcano, Africa has Ir of 8.5 ppt and Ni of 42 ppm which are similar to the Friedkin and Hall's Cave sediments (Zelenski et al., 2013). Gas condensates derived from aerosols from the new 2012-13 Tolbachik eruption have similar Ir

abundances of 0.1-0.23 ppb but three order of magnitude less Ni abundances, ranging from 33 to 36 ppb (Chaplygin et al., 2016). All samples from the Friedkin and Hall's Cave sites are consistent with upper continental crust values and volcanic aerosols and inconsistent with an admixture of impactites (Figure 3.13). In the Fur Formation of early Eocene age in Denmark, 34 volcanic ash layers were measured with UCC-like Ni and Ir abundances, with even larger variations in Ni and Ir, 3-155 ppm and 31-742 ppt, respectively (Schmitz and Asaro, 1996). The Ir and Ni data variation was associated with explosive volcanism during rifting of the Greenland-Eurasia a continent and subsequent sea-floor spreading in the northeastern North Atlantic (Schmitz and Asaro, 1996). Hence, at Friedkin and Hall's Cave sites, the Ir and Ni scattering may be analogically related to weathering and other post-depositional processes, the low abundances are consistent with terrestrial materials present (Figure 3.13).

In contrast to volatile-sensitive elements that are closely associated with iron or sulfide phases, lithophile elements such as Ti, Zr, Be, Hf, and Ta, generally occur in non-weathered silicate phases (Gluskoter, 1975; Moreno et al., 2008). These immobile trace elements indicate the Ti and Zr contents from horizons at the Friedkin and Hall's Cave sites plot within the field of Island Arc lavas (Figure 3.14) (Pearce, 1982), they are distinct from MORB and within-plate lavas from MORB and within-plate lavas. Therefore, the relatively large scatter for Ir versus Ni, compared to the linearly correlated Ti and Zr abundances, may have been due to their differences in stability and resistance to weathering and other post-depositional processes. The lithophile trace elements from the Friedkin site and Hall's Cave sediment are volcanic, which is consistent with origination from Plinian eruptions. Future research is needed to better understand the coupling or decoupling mechanisms within and against HSE and trace elements during the

volcanic emission processes and relation to the observed geochemical signature in Friedkin site, Hall's Cave and other sediments.

3.6 Conclusions

The Os abundances and $^{187}Os/^{188}Os$ ratios in sediment samples from the Friedkin site characteristically separate into radiogenic and unradiogenic groups. The unradiogenic samples with mantle-like $^{187}Os/^{188}Os$ ratios and Os enrichment were observed in seven different layers above, within, and below the YD basal boundary. The unradiogenic $^{187}Os/^{188}Os$ layers are consistent with mixing between Friedkin site sediment and a mantle-derived end-member with a range of $^{187}Os/^{188}Os$ ratios from 0.116 to 0.2. The radiogenic samples have $^{187}Os/^{188}Os$ ratios and low Os abundances that are typical for upper continental crust.

Mass balance models using a range of chondrite and iron meteorite indicates that extraterrestrial input does not explain the HSE abundance patterns for the samples from Friedkin site and Hall's Cave (Sun et al., 2020). These observations are inconsistent with the hypothesis that a bolide impact or airburst occurred at the start of the YD and triggered the global cooling event. At the Friedkin site and Hall's Cave, the bulk sediments with unradiogenic $^{187}Os/^{188}Os$ ratios and HSE systematics display similarities with volcanic aerosols (Yudovskaya et al., 2008; Zelenski et al., 2013; Chaplygin et al., 2016). Three horizons, including the YD boundary layer, can be correlated between the two localities based on their common chronostratigraphy and unradiogenic Os peaks. Relative to Hall's Cave section, the Friedkin site section has four additional, unmatched unradiogenic Os horizons. These unmatched horizons may lack correlation at Hall's Cave because of sampling resolution bias - coarser samples at Hall's Cave did not collect equivalent horizons. Alternatively, Os sample preparation resulted in bias from

the nugget effect, which is shown here by replicate measurements on samples from both locales. Future work will need to consider approaches that alleviate the bias issue, including analyzing multiple fractions of the same samples.

The trace element signatures of bulk sediments at the Friedkin and Hall's Cave sites are upper continental crust like. The Ir and Ni have relatively large abundance variations which could be caused by post-depositional disturbance including weathering. The Zr and Ti which are more resistant to weathering and other alteration processes after deposition show a significant linear correlation. The trace element abundances are most consistent with the volcanic origin for the $Os^{187}Os/^{188}$ ratio and HSE abundance anomaly observed at the Debra L. Friedkin and Hall's Cave sites during the YD cooling period.

The observed geochemical systematics in the unradiogenic Os horizons in the Friedkin and Hall's Cave sections suggest that the plausible mechanism for the YD cooling event is volcanic rather than extraterrestrial. These findings thus provide an interpretive perspective for future YD related studies to pinpoint the underlying originating mechanism(s). The results are inconsistent with the extraterrestrial hypothesis and support instead an episodic and volcanic origin for the observed geochemical anomalies at the Debra L. Friedkin and Hall's Cave sites, Texas

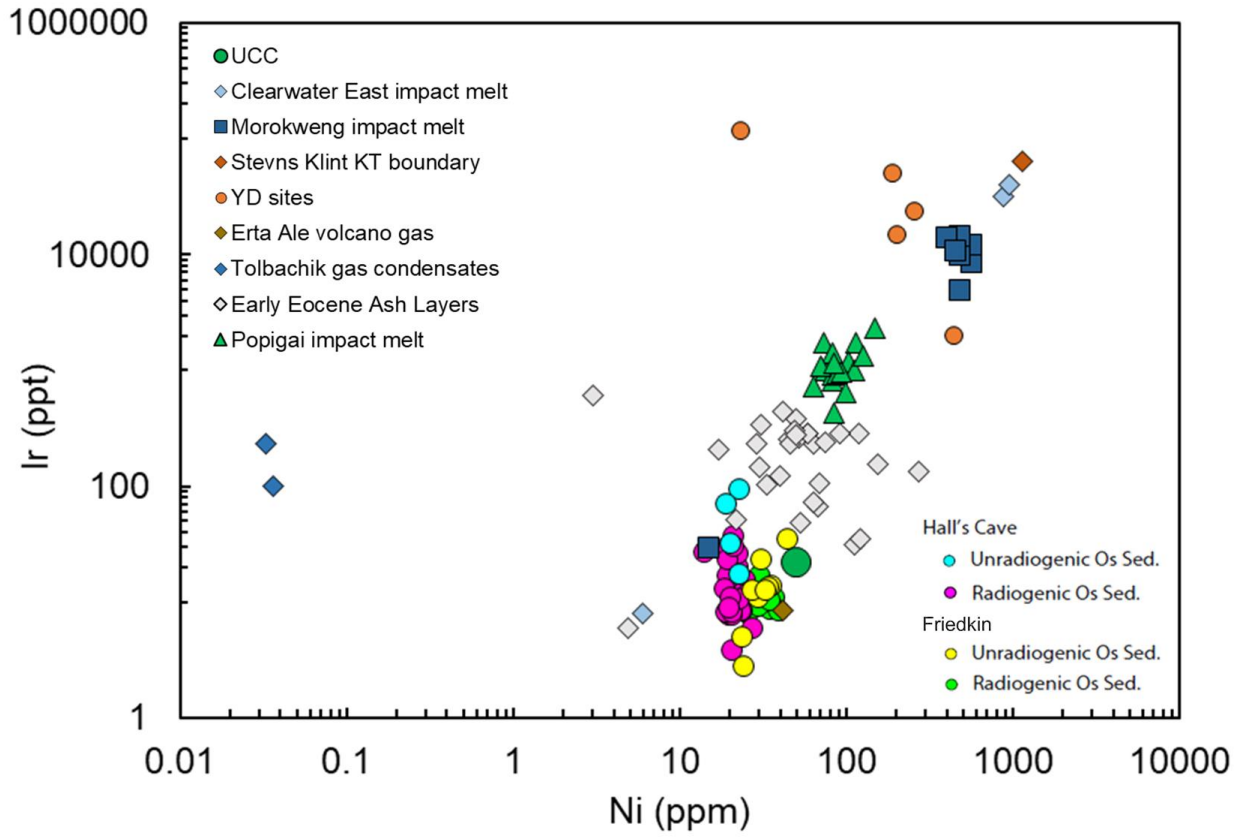

Figure 3.13 Ir-Ni results in the Friedkin and Hall's Cave sites. Magnetic grain Ni-Ir data are from Blackwater Draw, NM, Wally's Beach, AB, Topper, SC, Lommel, Belgium YD sites are from Firestone et al., (2007). Impact melt rock data sources are Popigai (Tagle and Claeys, 2005), Morokweng (McDonald, 2002), Clearwater East (Palme et al., 1978) and the Stevns Klint KT boundary (Alvarez et al., 1980). Erta Ale volcano gas and Tolbachik volcano gas condensate data are from Zelenski et al. (2013) and Chaplygin et al., (2016), respectively. Upper continental crust data source is Esser and Turekian, (1993), Park et al. (2012), and Gaschnig et al. (2016). The Early Eocene volcanic ash layers data are from early Eocene (Schmitz and Asaro, 1996).

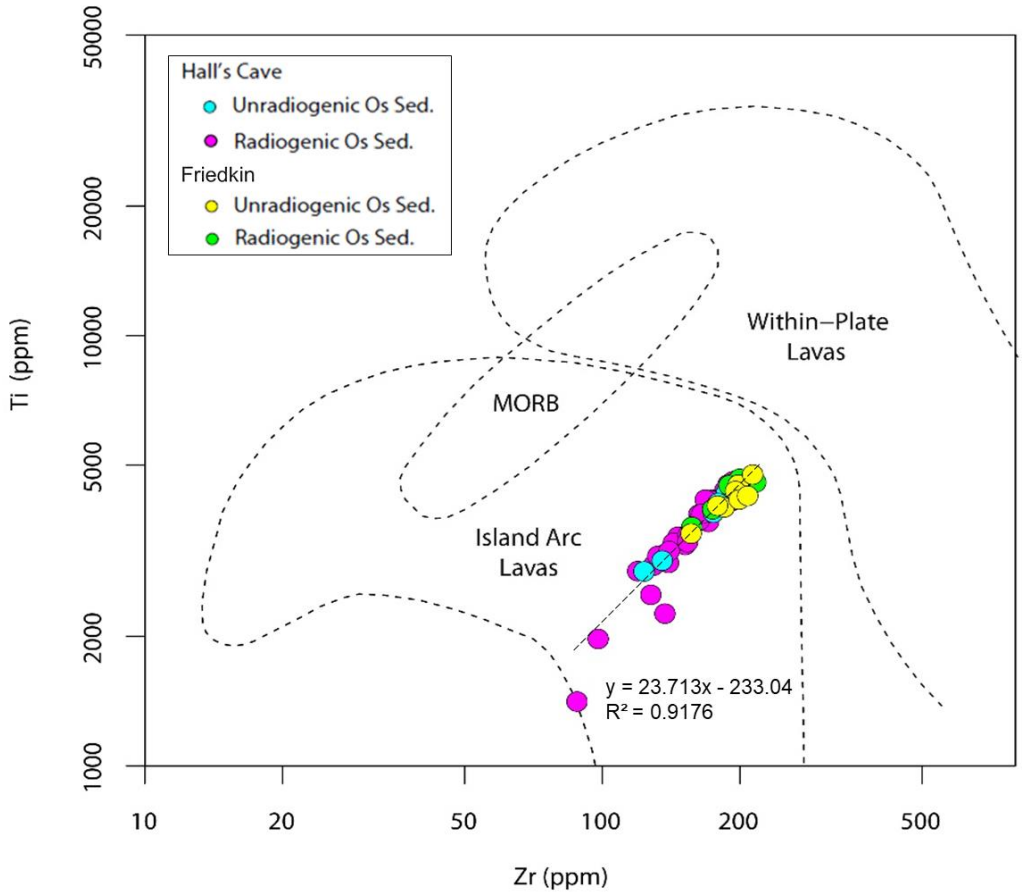

Figure 3.14 Hall's Cave and Friedkin site samples plotted in Ti vs Zr discrimination diagram of Pearce (1982) showing sample distribution in the domain of Island Arc Lavas.

Conclusions

This dissertation addresses two aspects of the application of Re-Os isotope system and/or HSE abundances, one is the use of Re-Os geochronology in dating geological processes, the other is the effects of different Earth components on Re-Os system and HSE abundances. The former aspect has extended Re-Os system to dating organic-rich sedimentary rocks and petroleum systems, the later aspect indicates that use of the combined approach is powerful in revealing the origin of the Re-Os isotopic ratios or HSE abundance anomalies.

In the first chapter, a suite of crude oils from Tarim Basin were analyzed for Re-Os isotopic composition. The $^{187}Os/^{188}Os$ ratios of the whole oils and asphaltene fractions show a large variation from 0.13-3.70. Three asphaltene samples and two whole oils display $^{187}Os/^{188}Os$ values of < 0.2, demonstrating a significant input from mantle fluids, which could be caused by Early Permian Tarim magmatism. In addition, the Re and Os isotope data of five Ordovician oils and one Triassic oil yield an Early Permian age 286.74 ± 2.34 Ma with MSWD = 2000, which agrees well with previous U–Pb zircon ages between 291 ± 4 and 272 ± 2 Ma using Tarim Flood Basalt rocks sampled in the Tabei uplift region. Five Ordovician oils yield a younger age of 227.20 ± 1.86 Ma with a smaller MSWD = 310. The much-improved regression suggest data scatter could be related to secondary alteration processes, such as TSR. The Ordovician and Triassic reservoirs currently have a thermal temperature of 100-140 °C which has reached the TSR temperature window. The 227 Ma age might represent post-Permian hydrothermal intrusion induced by the Tarim Flood Basalt, 290 Ma. The Re–Os elemental and isotopic results in crude oils from Tarim Basin has constrained the timing of petroleum events and traced the hydrothermal fluid disturbance to the petroleum systems.

In the second chapter, a well-dated sediment section at Hall's Cave, Texas, USA has been measured for $^{187}Os/^{188}Os$ ratios and HSE abundances to study the origin for the YD abrupt cooling event ca.12.9 ± 0.1 ka. The prevailing hypothesis for the YD cooling episode is that a bolide impact or airburst is responsible for the sudden climate change. In Hall's Cave, seven layers with unradiogenic $^{187}Os/^{188}Os$ ratios of 0.12 to 0.42 below, above, and within the YD basal boundary layer across a time interval of ~4,000 years. As the incremental mass balancing models show, the HSE pattern of the whole sample set could not be generated by mixing chondrites or iron meteorites with upper continental crust. Instead, gas condensates from three volcanoes have HSE abundance patterns and ratios that overlap with the Hall's Cave samples. Therefore, the most likely explanation for the HSE and Os isotope systematics of the unradiogenic Os samples is episodic, distant volcanic emissions in the Northern Hemisphere being preserved in Hall's Cave sediments at and near the onset of the Younger Dryas cooling period.

In the final chapter, a second sediment sequence at the Debra L. Friedkin site, Texas was sampled and analyzed for $^{187}Os/^{188}Os$ ratios and HSE abundances. This sediment column is well-dated with OSL ages. The Os isotope depth profiles at the Friedkin site also detected five unradiogenic Os layers above, within, and below the YD basal boundary layer. The chondrite-normalized HSE patterns resemble those from Hall's Cave, Texas. The new results independently confirm that the HSE abundances in the unradiogenic Os layers are likely a fingerprint of volcanic gas aerosols derived from large Plinian eruptions and not extra-terrestrial materials. In addition, for the Friedkin and Hall's Cave samples, the REE patterns and Ir, Ni, Ti and Zr abundances are also characterized are also characterized with terrestrial signatures as opposed to impact melt rocks. The age profile correlation between the two study sites, further

shows that three unradiogenic Os peaks overlap in time. The results are inconsistent with the extraterrestrial hypothesis and support instead an episodic and volcanic origin for the observed geochemical anomalies at the Debra L. Friedkin and Hall's Cave sites, Texas.

The outcome of the three chapters indicates that Re-Os geochronometer could not only date geological processes, but also serve as a useful aid to fingerprint mantle-derived flux to terrestrial settings, such as organic-rich materials, crude oils and unradiogenic sediments. Moreover, the observed geochemical approach used in the second and third chapter, indicates that possible impact makers could be also produced by volcanic emissions, the Os isotope and HSE should be coupled to help evaluate whether the underlying causing mechanism is bolide impact/air burst or terrestrial.

Bibliography:

Allègre C. J. and Luck J.-M. (1980) Osmium isotopes as petrogenetic and geological tracers. *Earth Planet. Sci. Lett.* **48**, 148–154.

Alley R. B. (2000) The Younger Dryas cold interval as viewed from central Greenland. *Quat. Sci. Rev.* **19**, 213–226.

Alley R. B. (2007) Wally Was Right: Predictive Ability of the North Atlantic "Conveyor Belt" Hypothesis for Abrupt Climate Change. *Annu. Rev. Earth Planet. Sci.* **35**, 241–272.

Alvarez L. W., Alvarez W., Asaro F. and Michel H. V. (1980) Extraterrestrial Cause for the Cretaceous-Tertiary Extinction. *Science* **208**, 1095–1108.

Anders E. and Grevesse N. (1989) Abundances of the elements: Meteoritic and solar. *Geochim. Cosmochim. Acta* **53**, 197–214.

Andrews J. T., Geirsdóttir A., Hardardóttir J., Principato S., Grönvold K., Kristjansdóttir G. B., Helgadóttir G., Drexler J. and Sveinbjörnsdóttir A. (2002) Distribution, sediment magnetism and geochemistry of the Saksunarvatn (10 180 ± 60 cal. yr BP) tephra in marine, lake, and terrestrial sediments, northwest Iceland. *J. Quat. Sci. Publ. Quat. Res. Assoc.* **17**, 731–745.

Arce J. L., Macías J. L. and Vázquez-Selem L. (2003) The 10.5 ka Plinian eruption of Nevado de Toluca volcano, Mexico: Stratigraphy and hazard implications. *Geol. Soc. Am. Bull.* **115**, 230–248.

Atwah I., Sweet S., Pantano J. and Knap A. (2019) Light Hydrocarbon Geochemistry: Insight into Mississippian Crude Oil Sources from the Anadarko Basin, Oklahoma, USA. *Geofluids* **2019**.

Baldini J. U. L., Brown R. J. and Mawdsley N. (2018) Evaluating the link between the sulfur-rich Laacher See volcanic eruption and the Younger Dryas climate anomaly. *Clim. Past* **14**, 969–990.

Barre A. B., Prinzhofer A. and Allegre C. J. (1995) Osmium isotopes in the organic matter of crude oil and asphaltenes. In *Terra Abstracts* p. 199.

Bazanova L. I., Melekestsev I. V., Ponomareva V. V., Dirksen O. V. and Dirksen V. G. (2016) Late Pleistocene and Holocene volcanic catastrophes in Kamchatka and in the Kuril Islands. Part 1. Types and classes of catastrophic eruptions as the leading components of volcanic catastrophism. *J. Volcanol. Seismol.* **10**, 151–169.

Becker H., Horan M. F., Walker R. J., Gao S., Lorand J.-P. and Rudnick R. L. (2006) Highly siderophile element composition of the Earth's primitive upper mantle: Constraints from new data on peridotite massifs and xenoliths. *Geochim. Cosmochim. Acta* **70**, 4528–4550.

Bézos A., Lorand J.-P., Humler E. and Gros M. (2005) Platinum-group element systematics in Mid-Oceanic Ridge basaltic glasses from the Pacific, Atlantic, and Indian Oceans. *Geochim. Cosmochim. Acta* **69**, 2613–2627.

Bindeman I. N., Fournelle J. H. and Valley J. W. (2001) Low-δ ^{18}O tephra from a compositionally zoned magma body: Fisher Caldera, Unimak Island, Aleutians. *J. Volcanol. Geotherm. Res.* **111**, 35–53.

Birck J. L., Barman M. R. and Capmas F. (1997) Re-Os Isotopic Measurements at the Femtomole Level in Natural Samples. *Geostand. Newsl.* **21**, 19–27.

Borg L. E., Brandon A. D., Clynne M. A. and Walker R. J. (2000) Re–Os isotopic systematics of primitive lavas from the Lassen region of the Cascade arc, California. *Earth Planet. Sci. Lett.* **177**, 301–317.

Bourne M. D., Feinberg J. M., Stafford T. W., Waters M. R., Lundelius E. and Forman S. L. (2016) High-intensity geomagnetic field 'spike' observed at ca. 3000 cal BP in Texas, USA. *Earth Planet. Sci. Lett.* **442**, 80–92.

Brakenridge G. R. (2011) Core-collapse supernovae and the Younger Dryas/terminal Rancholabrean extinctions. *Icarus* **215**, 101–106.

Brandon A. D., Humayun M., Puchtel I. S., Leya I. and Zolensky M. (2005) Osmium isotope evidence for an s-process carrier in primitive chondrites. *Science* **309**, 1233–1236.

Brandon A. D., Norman M. D., Walker R. J. and Morgan J. W. (1999) 186Os–187Os systematics of Hawaiian picrites. *Earth Planet. Sci. Lett.* **174**, 25–42.

Brandon A. D., Walker R. J., Morgan J. W. and Goles G. G. (2000) Re-Os isotopic evidence for early differentiation of the Martian mantle. *Geochim. Cosmochim. Acta* **64**, 4083–4095.

Brandon A. D., Walker R. J. and Puchtel I. S. (2006) Platinum–osmium isotope evolution of the Earth's mantle: Constraints from chondrites and Os-rich alloys. *Geochim. Cosmochim. Acta* **70**, 2093–2103.

Brauer A., Haug G. H., Dulski P., Sigman D. M. and Negendank J. F. W. (2008) An abrupt wind shift in western Europe at the onset of the Younger Dryas cold period. *Nat. Geosci.* **1**, 520–523.

Brenan J. M., Bennett N. R. and Zajacz Z. (2016) Experimental Results on Fractionation of the Highly Siderophile Elements (HSE) at Variable Pressures and Temperatures during Planetary and Magmatic Differentiation. *Rev. Mineral. Geochem.* **81**, 1–87.

Broecker W. S., Peteet D. M. and Rind D. (1985) Does the ocean–atmosphere system have more than one stable mode of operation? *Nature* **315**, 21–26.

Bronk Ramsey C. (2009) Bayesian Analysis of Radiocarbon Dates. *Radiocarbon* **51**, 337–360.

Bronk Ramsey C. (2008) Deposition models for chronological records. *Quat. Sci. Rev.* **27**, 42–60.

Bronk Ramsey C. (2013) OxCal ver. 4.2. 4 c14. arch. ox. ac. uk/oxcal. *OxCal Html*.

Cai C., Zhang C., Cai L., Wu G., Jiang L., Xu Z., Li K., Ma A. and Chen L. (2009) Origins of Palaeozoic oils in the Tarim Basin: Evidence from sulfur isotopes and biomarkers. *Chem. Geol.* **268**, 197–210.

Carlson A. E., Clark P. U., Haley B. A., Klinkhammer G. P., Simmons K., Brook E. J. and Meissner K. J. (2007) Geochemical proxies of North American freshwater routing during the Younger Dryas cold event. *Proc. Natl. Acad. Sci. U. S. A.* **104**, 6556–6561.

Chaplygin I. V., Lavrushin V. Y., Dubinina E. O., Bychkova Y. V., Inguaggiato S. and Yudovskaya M. A. (2016) Geochemistry of volcanic gas at the 2012–13 New Tolbachik eruption, Kamchatka. *J. Volcanol. Geotherm. Res.* **323**, 186–193.

Chen J., Xu Y. and Huang D. (2000) Geochemical Characteristics and Origin of Natural Gas in Tarim Basin, China. *AAPG Bull.* **84**, 591–606.

Chen M., Tian W., Suzuki K., Tejada M. L., Liu F.-L., Senda R., Wei C.-J., Chen B. and Chu Z.-Y. (2014) Peridotite and pyroxenite xenoliths from Tarim, NW China: Evidences for melt depletion and mantle refertilization in the mantle source region of the Tarim flood basalt. *Lithos* **204**.

Cheng H., Zhang H., Spötl C., Baker J., Sinha A., Li H., Bartolomé M., Moreno A., Kathayat G., Zhao J., Dong X., Li Y., Ning Y., Jia X., Zong B., Brahim Y. A., Pérez-Mejías C., Cai Y., Novello V. F., Cruz F. W., Severinghaus J. P., An Z. and Edwards R. L. (2020) Timing and structure of the Younger Dryas event and its underlying climate dynamics. *Proc. Natl. Acad. Sci.* **117**, 23408–23417.

Clarke M. C. (1990) Geological, Volcanological and Hydrogeological Controls on the Occurrence of Geothermal Activity in the Area Surrounding Lake Naivasha, Kenya: With Coloured 1: 250 000 Geological Maps. *Ministry of Energy.*

Cohen A. S., Coe A. L., Bartlett J. M. and Hawkesworth C. J. (1999) Precise Re–Os ages of organic-rich mudrocks and the Os isotope composition of Jurassic seawater. *Earth Planet. Sci. Lett.* **167**, 159–173.

Cohen A. S. and Waters F. G. (1996) Separation of osmium from geological materials by solvent extraction for analysis by thermal ionisation mass spectrometry. *Anal. Chim. Acta* **332**, 269–275.

Colodner D., Sachs J., Ravizza G., Turekian K., Edmond J. and Boyle E. (1993) The geochemical cycle of rhenium: a reconnaissance. *Earth Planet. Sci. Lett.* **117**, 205–221.

Condie K. C. (1993) Chemical composition and evolution of the upper continental crust: Contrasting results from surface samples and shales. *Chem. Geol.* **104**, 1–37.

Connolly B. D., Puchtel I. S., Walker R. J., Arevalo R., Piccoli P. M., Byerly G., Robin-Popieul C. and Arndt N. (2011) Highly siderophile element systematics of the 3.3Ga Weltevreden komatiites, South Africa: Implications for early Earth history. *Earth Planet. Sci. Lett.* **311**, 253–263.

Cook D. L., Walker R. J., Horan M. F., Wasson J. T. and Morgan J. W. (2004) Pt-Re-Os systematics of group IIAB and IIIAB iron meteorites. *Geochim. Cosmochim. Acta* **68**, 1413–1431.

Corrick A. J., Selby D., McKirdy D. M., Hall P. A., Gong S., Trefry C. and Ross A. S. (2019) Remotely constraining the temporal evolution of offshore oil systems. *Sci. Rep.* **9**, 1327.

Creaser R. A., Papanastassiou D. A. and Wasserburg G. J. (1991) Negative thermal ion mass spectrometry of osmium, rhenium and iridium. *Geochim. Cosmochim. Acta* **55**, 397–401.

Creaser R. A., Sannigrahi P., Chacko T. and Selby D. (2002) Further evaluation of the Re-Os geochronometer in organic-rich sedimentary rocks: a test of hydrocarbon maturation effects in the Exshaw Formation, Western Canada Sedimentary Basin. *Geochim. Cosmochim. Acta* **66**, 3441–3452.

Cukur D., Horozal S., Kim D. C., Lee G. H., Han H. C. and Kang M. H. (2010) The distribution and characteristics of the igneous complexes in the northern East China Sea Shelf Basin and their implications for hydrocarbon potential. *Mar. Geophys. Res.* **31**, 299–313.

Cumming V. M., Selby D. and Lillis P. G. (2012) Re–Os geochronology of the lacustrine Green River Formation: Insights into direct depositional dating of lacustrine successions, Re–Os systematics and paleocontinental weathering. *Earth Planet. Sci. Lett.* **359–360**, 194–205.

Cumming V. M., Selby D., Lillis P. G. and Lewan M. D. (2014) Re–Os geochronology and Os isotope fingerprinting of petroleum sourced from a Type I lacustrine kerogen: Insights from the natural Green River petroleum system in the Uinta Basin and hydrous pyrolysis experiments. *Geochim. Cosmochim. Acta* **138**, 32–56.

Daulton T. L., Amari S., Scott A. C., Hardiman M., Pinter N. and Anderson R. S. (2017) Comprehensive analysis of nanodiamond evidence relating to the Younger Dryas Impact Hypothesis. *J. Quat. Sci.* **32**, 7–34.

Daulton T. L., Pinter N. and Scott A. C. (2010) No evidence of nanodiamonds in Younger–Dryas sediments to support an impact event. *Proc. Natl. Acad. Sci.* **107**, 16043–16047.

Day J. M. D. (2013) Hotspot volcanism and highly siderophile elements. *Chem. Geol.* **341**, 50–74.

Day James M.D., Brandon A. D. and Walker R. J. (2016) Highly Siderophile Elements in Earth, Mars, the Moon, and Asteroids. *Rev. Mineral. Geochem.* **81**, 161–238.

Day James M. D., Waters C. L., Schaefer B. F., Walker R. J. and Turner S. (2016) Use of Hydrofluoric Acid Desilicification in the Determination of Highly Siderophile Element Abundances and Re-Pt-Os Isotope Systematics in Mafic-Ultramafic Rocks. *Geostand. Geoanalytical Res.* **40**, 49–65.

Day J. M., Walker R. J., James O. B. and Puchtel I. S. (2010) Osmium isotope and highly siderophile element systematics of the lunar crust. *Earth Planet. Sci. Lett.* **289**, 595–605.

Deino A. L., Orsi G., de Vita S. and Piochi M. (2004) The age of the Neapolitan Yellow Tuff caldera-forming eruption (Campi Flegrei caldera–Italy) assessed by $^{40}Ar/^{39}Ar$ dating method. *J. Volcanol. Geotherm. Res.* **133**, 157–170.

DiMarzio J. M., Georgiev S. V., Stein H. J. and Hannah J. L. (2018) Residency of rhenium and osmium in a heavy crude oil. *Geochim. Cosmochim. Acta* **220**, 180–200.

Driese S. G., Nordt L. C., Waters M. R. and Keene J. L. (2013) Analysis of Site Formation History and Potential Disturbance of Stratigraphic Context in Vertisols at the Debra L. Friedkin Archaeological Site in Central Texas, USA. *Geoarchaeology* **28**, 221–248.

Esser B. K. and Turekian K. K. (1993) The osmium isotopic composition of the continental crust. *Geochim. Cosmochim. Acta* **57**, 3093–3104.

Evans N. J., Gregoire D. C., grieve R. A. F., Goodfellow W. D. and veizer J. (1993) Use of platinum-group elements for impactor identification: Terrestrial impact craters and Cretaceous-Tertiary boundary. *Geochim. Cosmochim. Acta* **57**, 3737–3748.

Finlay A. J., Selby D. and Osborne M. J. (2011) Re-Os geochronology and fingerprinting of United Kingdom Atlantic margin oil: Temporal implications for regional petroleum systems. *Geology* **39**, 475–478.

Finlay A. J., Selby D., Osborne M. J. and Finucane D. (2010) Fault-charged mantle-fluid contamination of United Kingdom North Sea oils: Insights from Re-Os isotopes. *Geology* **38**, 979–982.

Firestone R. B., West A., Kennett J. P., Becker L., Bunch T. E., Revay Z. S., Schultz P. H., Belgya T., Kennett D. J., Erlandson J. M., Dickenson O. J., Goodyear A. C., Harris R. S., Howard G. A., Kloosterman J. B., Lechler P., Mayewski P. A., Montgomery J., Poreda R., Darrah T., Hee S. S. Q., Smith A. R., Stich A., Topping W., Wittke J. H. and Wolbach W. S. (2007) Evidence for an extraterrestrial impact 12,900 years ago that contributed to the megafaunal extinctions and the Younger Dryas cooling. *Proc. Natl. Acad. Sci.* **104**, 16016–16021.

Fischer-Gödde M., Becker H. and Wombacher F. (2010) Rhodium, gold and other highly siderophile element abundances in chondritic meteorites. *Geochim. Cosmochim. Acta* **74**, 356–379.

Forman S. L. and Waters M. R. (2016) Optically Stimulated Luminescence Dating and the Peopling of the Americas. *PaleoAmerica* **2**, 6–10.

Foster J. G., Lambert D. D., Frick L. R. and Maas R. (1996) Re–Os isotopic evidence for genesis of Archaean nickel ores from uncontaminated komatiites. *Nature* **382**, 703–706.

Gannoun A., Burton K. W., Day J. M. D., Harvey J., Schiano P. and Parkinson I. (2016) Highly Siderophile Element and Os Isotope Systematics of Volcanic Rocks at Divergent and Convergent Plate Boundaries and in Intraplate Settings. *Rev. Mineral. Geochem.* **81**, 651–724.

Gannoun A., Burton K. W., Parkinson I. J., Alard O., Schiano P. and Thomas L. E. (2007) The scale and origin of the osmium isotope variations in mid-ocean ridge basalts. *Earth Planet. Sci. Lett.* **259**, 541–556.

Gannoun A., Vlastélic I. and Schiano P. (2015) Escape of unradiogenic osmium during sub-aerial lava degassing: Evidence from fumarolic deposits, Piton de la Fournaise, Réunion Island. *Geochim. Cosmochim. Acta* **166**, 312–326.

Gao Y., Huang J., Casey J. F. and Banerjee N. R. (2009) Data report: trace element geochemistry of oceanic crust formed at superfast-spreading ridge, Hole 1256D. *Proceedings of the Integrated Ocean Drilling Program* **309**, 312.

Gao Z., Tian W., Wang L., Shi Y. and Pan M. (2017) Emplacement of intrusions of the Tarim Flood Basalt Province and their impacts on oil and gas reservoirs: A 3D seismic reflection study in Yingmaili fields, Tarim Basin, northwest China. *Interpretation* **5**, SK51–SK63.

Gardner J. E., Carey S. and Sigurdsson H. (1998) Plinian eruptions at Glacier Peak and Newberry volcanoes, United States: Implications for volcanic hazards in the Cascade Range. *Geol. Soc. Am. Bull.* **110**, 173–187.

Gaschnig R. M., Rudnick R. L., McDonough W. F., Kaufman A. J., Valley J. W., Hu Z., Gao S. and Beck M. L. (2016) Compositional evolution of the upper continental crust through time, as constrained by ancient glacial diamictites. *Geochim. Cosmochim. Acta* **186**, 316–343.

Ge X., Shen C., Selby D., Deng D. and Mei L. (2016) Apatite fission-track and Re-Os geochronology of the Xuefeng uplift, China: Temporal implications for dry gas associated hydrocarbon systems. *Geology* **44**, 491–494.

Gelinas A., Kring D. A., Zurcher L., Urrutia-Fucugauchi J., Morton O. and Walker R. J. (2004) Osmium isotope constraints on the proportion of bolide component in Chicxulub impact melt rocks. *Meteorit. Planet. Sci.* **39**, 1003–1008.

Georgiev S. V., Stein H. J., Hannah J. L., Galimberti R., Nali M., Yang G. and Zimmerman A. (2016) Re–Os dating of maltenes and asphaltenes within single samples of crude oil. *Geochim. Cosmochim. Acta* **179**, 53–75.

Georgiev S. V., Stein H. J., Yang G., Hannah J. L., Böttcher M. E., Grice K., Holman A. I., Turgeon S., Simonsen S. and Cloquet C. (2020) Late Permian–Early Triassic environmental changes recorded by multi-isotope (Re-Os-N-Hg) data and trace metal distribution from the Hovea-3 section, Western Australia. *Gondwana Res.* **88**, 353–372.

Gluskoter H. J. (1975) Mineral Matter and Trace Elements in Coal. In *Trace Elements in Fuel* Advances in Chemistry. American Chemical Society **1**, 1–22.

Goderis S., Brandon A. D., Mayer B. and Humayun M. (2017) Osmium isotopic homogeneity in the CK carbonaceous chondrites. *Geochim. Cosmochim. Acta* **216**, 8–27.

Graf H.-F. and Timmreck C. (2001) A general climate model simulation of the aerosol radiative effects of the Laacher See eruption (10,900 B.C.). *J. Geophys. Res. Atmospheres* **106**, 14747–14756.

Gromet L. P., Haskin L. A., Korotev R. L. and Dymek R. F. (1984) The "North American shale composite": Its compilation, major and trace element characteristics. *Geochim. Cosmochim. Acta* **48**, 2469–2482.

Guthrie R. D. (2006) New carbon dates link climatic change with human colonization and Pleistocene extinctions. *Nature* **441**, 207–209.

Harms E. and Schmincke H.-U. (2000) Volatile composition of the phonolitic Laacher See magma (12,900 yr BP): implications for syn-eruptive degassing of S, F, Cl and H_2O. *Contrib. Mineral. Petrol.* **138**, 84–98.

Hart S. R. and Ravizza G. E. (1996) Os partitioning between phases in lherzolite and basalt. *Geophys. Monogr.-Am. Geophys. Union* **95**, 123–134.

Henley R. W. and Berger B. R. (2013) Nature's refineries — Metals and metalloids in arc volcanoes. *Earth-Sci. Rev.* **125**, 146–170.

Hirt B., Tilton G. R., Herr E. and Hoffmeister W. (1963) The half-life of Re 187. *Earth Sci. Meteorit. Ed J Geiss Goldberg*, 273–280.

van Hoesel A., Hoek W. Z., Pennock G. M. and Drury M. R. (2014) The Younger Dryas impact hypothesis: a critical review. *Quat. Sci. Rev.* **83**, 95–114.

Holford S. P., Schofield N., Jackson C.-L., Magee C., Green P. F. and Duddy I. R. (2013) Impacts of igneous intrusions on source reservoir potential in prospective sedimentary basins along the western Australian continental margin. *West Australia Basins Symposium* **August 2013**.

Holford S., Schofield N., MacDonald J., Duddy I. and Green P. (2012) Seismic analysis of igneous systems in sedimentary basins and their impacts on hydrocarbon prospectivity: examples from the southern Australian margin. *APPEA J.* **52**, 229–252.

Horan M. F., Morgan J. W., Walker R. J. and Grossman J. N. (1992) Rhenium-Osmium Isotope Constraints on the Age of Iron Meteorites. *Science* **255**, 1118–1121.

Horan M., Walker R. J., Morgan J. W., Grossman J. and Rubin A. (2003) Highly siderophile elements in chondrites. *Chem. Geol.* **196**, 27–42.

Hurtig N. C., Georgiev S. V., Stein H. J. and Hannah J. L. (2019) Re-Os systematics in petroleum during water-oil interaction: The effects of oil chemistry. *Geochim. Cosmochim. Acta* **247**, 142–161.

Ireland T. J., Walker R. J. and Garcia M. O. (2009) Highly siderophile element and ^{187}Os isotope systematics of Hawaiian picrites: Implications for parental melt composition and source heterogeneity. *Chem. Geol.* **260**, 112–128.

Jennings A., Thordarson T., Zalzal K., Stoner J., Hayward C., Geirsdóttir Á. and Miller G. (2014) Holocene tephra from Iceland and Alaska in SE Greenland Shelf Sediments. *Geol. Soc. Lond. Spec. Publ.* **398**, SP398.6.

Jia W., Xiao Z., Yu C. and Peng P. (2010) Molecular and isotopic compositions of bitumens in Silurian tar sands from the Tarim Basin, NW China: Characterizing biodegradation and hydrocarbon charging in an old composite basin. *Mar. Pet. Geol.* **27**, 13–25.

Kastning E. H. (1987) Solution-subsidence-collapse in central Texas: Ordovician to Quaternary. In *Multidisciplinary conference on sinkholes and the environmental impacts of karst. **2***, 41–46.

Kendall Brian, Creaser R. A., Gordon G. W. and Anbar A. D. (2009) Re–Os and Mo isotope systematics of black shales from the Middle Proterozoic Velkerri and Wollogorang Formations, McArthur Basin, northern Australia. *Geochim. Cosmochim. Acta* **73**, 2534–2558.

Kendall B., Creaser R. A. and Selby D. (2009) ^{187}Re- ^{187}Os geochronology of Precambrian organic-rich sedimentary rocks. *Geol. Soc. Spec. Publ.* **326**, 85–107.

Kennett Douglas J., Kennett J. P., West A., West G. J., Bunch T. E., Culleton B. J., Erlandson J. M., Hee S. S. Q., Johnson J. R., Mercer C., Shen F., Sellers M., Stafford Jr. T. W., Stich A., Weaver J. C., Wittke J. H. and Wolbach W. S. (2009a) Shock-synthesized hexagonal

diamonds in Younger Dryas boundary sediments. *Proc. Natl. Acad. Sci.* **106**, 12623–12628.

Kennett D. J., Kennett J. P., West A., Mercer C., Hee S. S. Q., Bement L., Bunch T. E., Sellers M. and Wolbach W. S. (2009b) Nanodiamonds in the Younger Dryas Boundary Sediment Layer. *Science* **323**, 94–94.

Kim G. B., Cronin S. J., Yoon W. S. and Sohn Y. K. (2014) Post 19 ka BP eruptive history of Ulleung Island, Korea, inferred from an intra-caldera pyroclastic sequence. *Bull. Volcanol.* **76**, 802.

Kinzie C. R., Que Hee S. S., Stich A., Tague K. A., Mercer C., Razink J. J., Kennett D. J., DeCarli P. S., Bunch T. E., Wittke J. H., Israde-Alcántara I., Bischoff J. L., Goodyear A. C., Tankersley K. B., Kimbel D. R., Culleton B. J., Erlandson J. M., Stafford T. W., Kloosterman J. B., Moore A. M. T., Firestone R. B., Aura Tortosa J. E., Jordá Pardo J. F., West A., Kennett J. P. and Wolbach W. S. (2014) Nanodiamond-Rich Layer across Three Continents Consistent with Major Cosmic Impact at 12,800 Cal BP. *J. Geol.* **122**, 475–506.

Kjær K. H., Larsen N. K., Binder T., Bjørk A. A., Eisen O., Fahnestock M. A., Funder S., Garde A. A., Haack H., Helm V., Houmark-Nielsen M., Kjeldsen K. K., Khan S. A., Machguth H., McDonald I., Morlighem M., Mouginot J., Paden J. D., Waight T. E., Weikusat C., Willerslev E. and MacGregor J. A. (2018) A large impact crater beneath Hiawatha Glacier in northwest Greenland. *Sci. Adv.* **4**, eaar8173.

Krähenbühl U., Geissbühler M., Bühler F., Eberhardt P. and Finnegan D. L. (1992) Osmium isotopes in the aerosols of the mantle volcano Mauna Loa. *Earth Planet. Sci. Lett.* **110**, 95–98.

Kuehn S. C., Froese D. G., Carrara P. E., Foit F. F., Pearce N. J. and Rotheisler P. (2009) Major- and trace-element characterization, expanded distribution, and a new chronology for the latest Pleistocene Glacier Peak tephras in western North America. *Quat. Res.* **71**, 201–216.

Lassiter J. C. and Luhr J. F. (2001) Osmium abundance and isotope variations in mafic Mexican volcanic rocks: Evidence for crustal contamination and constraints on the geochemical behavior of osmium during partial melting and fractional crystallization. *Geochem. Geophys. Geosystems* **2**.

Lee K.-Y. (1985) Geology of the Tarim Basin with special emphasis on petroleum deposits, Xinjiang Uygur Zizhiqu, Northwest China. *US Geological Survey*.

Levasseur S., Birck J.-L. and Allègre C. J. (1998) Direct Measurement of Femtomoles of Osmium and the $^{187}Os/^{186}Os$ Ratio in Seawater. *Science* **282**, 272–274.

Li D., Liang D., Jia C., Wang G., Wu Q. and He D. (1996) Hydrocarbon accumulation in the Tarim Basin, China. *AAPG Bull.* **80**.

Li Z., Yang S., Chen H., Langmuir C. H., Yu X., Lin X. and Li Y. (2008) Chronology and geochemistry of Taxinan hasalts from the Tarim basin: Evidence for Permian plume magmatism. *Acta Petrologica Sinica.* **24**, 959-970.

Lillis P. G. and Selby D. (2013) Evaluation of the rhenium–osmium geochronometer in the Phosphoria petroleum system, Bighorn Basin of Wyoming and Montana, USA. *Geochim. Cosmochim. Acta* **118**, 312–330.

Lindquist A. K., Feinberg J. M. and Waters M. R. (2011) Rock magnetic properties of a soil developed on an alluvial deposit at Buttermilk Creek, Texas, USA. *Geochem. Geophys. Geosystems.* **12**, 1-11.

Liu J. (2017) Re-Os Systematics of Crude Oil and Re-Os Petroleum System Geochronology. Ph. D. thesis, Durham University.

Liu J. and Selby D. (2018) A Matrix-Matched Reference Material for Validating Petroleum Re-Os Measurements. *Geostand. Geoanalytical Res.* **42**, 97–113.

Liu Q., Dai J., Li J. and Zhou Q. (2008) Hydrogen isotope composition of natural gases from the Tarim Basin and its indication of depositional environments of the source rocks. *Sci. China Ser. Earth Sci.* **51**, 300–311.

Liu Q., Zhijun J., Jianfa C., Krooss B. M. and Qin S. (2012) Origin of nitrogen molecules in natural gas and implications for the high risk of N_2 exploration in Tarim Basin, NW China. *J. Pet. Sci. Eng.* **81**, 112–121.

Lohne Ø. S., Mangerud J. A. N. and Birks H. H. (2014) IntCal13 calibrated ages of the Vedde and Saksunarvatn ashes and the Younger Dryas boundaries from Kråkenes, western Norway. *J. Quat. Sci.* **29**, 506–507.

Lu X. X., Fan Q., Zhao F., Wang Q., Xie Q. and Yang H. (2007) The Silurian play in the Tazhong Uplift, Tarim Basin, northwestern China. *Mar. Pet. Geol.* **24**, 189–198.

Luck J. M. and Turekian K. K. (1983) Osmium-187/Osmium-186 in Manganese Nodules and the Cretaceous-Tertiary Boundary. *Science* **222**, 613–615.

Luck J.-M., Birck J.-L. and Allegre C.-J. (1980) 187 Re– 187 Os systematics in meteorites: early chronology of the Solar System and age of the Galaxy. *Nature* **283**, 256–259.

Macdonald R. and Scaillet B. (2006) The central Kenya peralkaline province: insights into the evolution of peralkaline salic magmas. *Lithos* **91**, 59–73.

Machel H. G. (2001) Bacterial and thermochemical sulfate reduction in diagenetic settings — old and new insights. *Sediment. Geol.* **140**, 143–175.

Mahdaoui F., Michels R., Reisberg L., Pujol M. and Poirier Y. (2015) Behavior of Re and Os during contact between an aqueous solution and oil: Consequences for the application of the Re–Os geochronometer to petroleum. *Geochim. Cosmochim. Acta* **158**, 1–21.

Mahdaoui F., Reisberg L., Michels R., Hautevelle Y., Poirier Y. and Girard J.-P. (2013) Effect of the progressive precipitation of petroleum asphaltenes on the Re–Os radioisotope system. *Chem. Geol.* **358**, 90–100.

Markey R., Stein H. and Morgan J. (1998) Highly precise Re–Os dating for molybdenite using alkaline fusion and NTIMS. *Talanta* **45**, 935–946.

McDonald I. (2002) Clearwater East impact structure: A re-interpretation of the projectile type using new platinum-group element data from meteorites. *Meteorit. Planet. Sci.* **37**, 459–464.

McDonald I., Andreoli M. A. G., Hart R. J. and Tredoux M. (2001) Platinum-group elements in the Morokweng impact structure, South Africa: Evidence for the impact of a large ordinary chondrite projectile at the Jurassic-Cretaceous boundary. *Geochim. Cosmochim. Acta* **65**, 299–309.

McDonough W. F. and Sun S. -s. (1995) The composition of the Earth. *Chem. Geol.* **120**, 223–253.

McManus J. F., Francois R., Gherardi J.-M., Keigwin L. D. and Brown-Leger S. (2004) Collapse and rapid resumption of Atlantic meridional circulation linked to deglacial climate changes. *Nature* **428**, 834–837.

Meisel T., Walker R. J. and Morgan J. W. (1996) The osmium isotopic composition of the Earth's primitive upper mantle. *Nature* **383**, 517–520.

Moore C. R., Brooks M. J., Goodyear A. C., Ferguson T. A., Perrotti A. G., Mitra S., Listecki A. M., King B. C., Mallinson D. J., Lane C. S., Kapp J. D., West A., Carlson D. L., Wolbach W. S., Them T. R., Harris M. S. and Pyne-O'Donnell S. (2019) Sediment Cores from White Pond, South Carolina, contain a Platinum Anomaly, Pyrogenic Carbon Peak, and Coprophilous Spore Decline at 12.8 ka. *Sci. Rep.* **9**, 15121.

Moore C. R., West A., LeCompte M. A., Brooks M. J., Daniel I. R., Goodyear A. C., Ferguson T. A., Ivester A. H., Feathers J. K., Kennett J. P., Tankersley K. B., Adedeji A. V. and Bunch T. E. (2017) Widespread platinum anomaly documented at the Younger Dryas onset in North American sedimentary sequences. *Sci. Rep.* **7**, 44031.

Morelli R. M., Bell C. C., Creaser R. A. and Simonetti A. (2010) Constraints on the genesis of gold mineralization at the Homestake Gold Deposit, Black Hills, South Dakota from rhenium–osmium sulfide geochronology. *Miner. Deposita* **45**, 461–480.

Moreno T., Amato F., Querol X., Alastuey A. and Gibbons W. (2008) Trace element fractionation processes in resuspended mineral aerosols extracted from Australian continental surface materials. *Soil Res.* **46**, 128–140.

Morgan J. W. (1986) Ultramafic xenoliths: Clues to Earth's late accretionary history. *J. Geophys. Res. Solid Earth* **91**, 12375–12387.

Mullineaux D. R. (1996) Pre-1980 tephra-fall deposits erupted from Mount St. Helens, Washington. *US Geological Survey* **1563**.

Neave D. A., Maclennan J., Thordarson T. and Hartley M. E. (2015) The evolution and storage of primitive melts in the Eastern Volcanic Zone of Iceland: the 10 ka Grímsvötn tephra series (i.e. the Saksunarvatn ash). *Contrib. Mineral. Petrol.* **170**, 21.

Nelson W. R., Furman T., van Keken P. E., Shirey S. B. and Hanan B. B. (2012) OsHf isotopic insight into mantle plume dynamics beneath the East African Rift System. *Chem. Geol.* **320–321**, 66–79.

Oppenheimer C., Scaillet B. and Martin R. S. (2011) Sulfur Degassing From Volcanoes: Source Conditions, Surveillance, Plume Chemistry and Earth System Impacts. *Rev. Mineral. Geochem.* **73**, 363–421.

Orr W. L. (1974) Changes in Sulfur Content and Isotopic Ratios of Sulfur during Petroleum Maturation—Study of Big Horn Basin Paleozoic Oils. *AAPG Bull.* **58**, 2295–2318.

Palme H., Janssens M.-J., Takahashi H., Anders E. and Hertogen J. (1978) Meteoritic material at five large impact craters. *Geochim. Cosmochim. Acta* **42**, 313–323.

Paquay F. S., Goderis S., Ravizza G., Vanhaeck F., Boyd M., Surovell T. A., Holliday V. T., Haynes C. V. and Claeys P. (2009) Absence of geochemical evidence for an impact event at the Bølling–Allerød/Younger Dryas transition. *Proc. Natl. Acad. Sci.* **106**, 21505–21510.

Park J.-W., Hu Z., Gao S., Campbell I. H. and Gong H. (2012) Platinum group element abundances in the upper continental crust revisited – New constraints from analyses of Chinese loess. *Geochim. Cosmochim. Acta* **93**, 63–76.

Pearce J. A. (1982) Trace element characteristics of lavas from destructive plate boundaries. *Andesites* **8**, 525–548.

Pearson D. G., Carlson R. W., Shirey S. B., Boyd F. R. and Nixon P. H. (1995) Stabilisation of Archaean lithospheric mantle: A ReOs isotope study of peridotite xenoliths from the Kaapvaal craton. *Earth Planet. Sci. Lett.* **134**, 341–357.

Pearson D. G., Irvine G. J., Ionov D. A., Boyd F. R. and Dreibus G. E. (2004) Re–Os isotope systematics and platinum group element fractionation during mantle melt extraction: a study of massif and xenolith peridotite suites. *Chem. Geol.* **208**, 29–59.

Petaev M. I., Huang S., Jacobsen S. B. and Zindler A. (2013) Large Pt anomaly in the Greenland ice core points to a cataclysm at the onset of Younger Dryas. *Proc. Natl. Acad. Sci.* **110**, 12917–12920.

Petaev M. I. and Jacobsen S. B. (2004) Differentiation of metal-rich meteoritic parent bodies: I. Measurements of PGEs, Re, Mo, W, and Au in meteoritic Fe-Ni metal. *Meteorit. Planet. Sci.* **39**, 1685–1697.

Petrini R., Forte C., Contin G., Pinzino C. and Orsi G. (1999) Structure of volcanic glasses from the NMR-EPR perspective: a preliminary application to the Neapolitan Yellow Tuff. *Bull. Volcanol.* **60**, 425–431.

Peucker-Ehrenbrink B., Hanghoj K., Atwood T. and Kelemen P. B. (2012) Rhenium-osmium isotope systematics and platinum group element concentrations in oceanic crust. *Geology* **40**, 199–202.

Peucker-Ehrenbrink B. and Jahn B. (2001) Rhenium-osmium isotope systematics and platinum group element concentrations: Loess and the upper continental crust. *Geochem. Geophys. Geosystems* **2**.

Pirajno F., Seltmann R. and Yang Y. (2011) A review of mineral systems and associated tectonic settings of northern Xinjiang, NW China. *Geosci. Front.* **2**, 157–185.

Poirier A. (2006) Re–Os and Pb isotope systematics in reduced fjord sediments from Saanich Inlet (Western Canada). *Earth Planet. Sci. Lett.* **249**, 119–131.

Puchtel I. S., Brandon A. D., Humayun M. and Walker R. J. (2005) Evidence for the early differentiation of the core from Pt–Re–Os isotope systematics of 2.8-Ga komatiites. *Earth Planet. Sci. Lett.* **237**, 118–134.

Puchtel I. S. and Humayun M. (2001) Platinum group element fractionation in a komatiitic basalt lava lake. *Geochim. Cosmochim. Acta* **65**, 2979–2993.

Puchtel I. S., Humayun M., Campbell A. J., Sproule R. A. and Lesher C. M. (2004) Platinum group element geochemistry of komatiites from the Alexo and Pyke Hill areas, Ontario, Canada. *Geochim. Cosmochim. Acta* **68**, 1361–1383.

Puchtel I. S., Walker R. J., James O. B. and Kring D. A. (2008) Osmium isotope and highly siderophile element systematics of lunar impact melt breccias: implications for the late accretion history of the Moon and Earth. *Geochim. Cosmochim. Acta* **72**, 3022–3042.

Pyne-O'Donnell S. D. F., Cwynar L. C., Jensen B. J. L., Vincent J. H., Kuehn S. C., Spear R. and Froese D. G. (2016) West Coast volcanic ashes provide a new continental-scale Lateglacial isochron. *Quat. Sci. Rev.* **C**, 16–25.

Ramsey C. B., Albert P. G., Blockley S. P., Hardiman M., Housley R. A., Lane C. S., Lee S., Matthews I. P., Smith V. C. and Lowe J. J. (2015) Improved age estimates for key Late Quaternary European tephra horizons in the RESET lattice. *Quat. Sci. Rev.* **118**, 18–32.

Ravizza G. and Turekian K. K. (1989) Application of the ^{187}Re-^{187}Os system to black shale geochronometry. *Geochim. Cosmochim. Acta* **53**, 3257–3262.

Ravizza G., Turekian K. K. and Hay B. J. (1991) The geochemistry of rhenium and osmium in recent sediments from the Black Sea. *Geochim. Cosmochim. Acta* **55**, 3741–3752.

Razzhigaeva N. G., Matsumoto A. and Nakagawa M. (2016) Age, source, and distribution of Holocene tephra in the southern Kurile Islands: evaluation of Holocene eruptive activities in the southern Kurile arc. *Quat. Int.* **397**, 63–78.

Reisberg L., Alard O., Lorand J.-P. and Ohnenstetter M. (2004) Highly siderophile element behavior in high temperature processes. *Chem. Geol.* **208**, 1–4.

Robock A. (2000) Volcanic eruptions and climate. *Rev. Geophys.* **38**, 191–219.

Rogers N. W., Evans P. J., Blake S., Scott S. C. and Hawkesworth C. J. (2004) Rates and timescales of fractional crystallization from ^{238}U–^{230}Th–^{226}Ra disequilibria in trachyte lavas from Longonot volcano, Kenya. *J. Petrol.* **45**, 1747–1776.

Rooney A. D., Selby D., Houzay J.-P. and Renne P. R. (2010) Re–Os geochronology of a Mesoproterozoic sedimentary succession, Taoudeni basin, Mauritania: Implications for basin-wide correlations and Re–Os organic-rich sediments systematics. *Earth Planet. Sci. Lett.* **289**, 486–496.

Rooney A. D., Selby D., Lewan M. D., Lillis P. G. and Houzay J.-P. (2012) Evaluating Re–Os systematics in organic-rich sedimentary rocks in response to petroleum generation using hydrous pyrolysis experiments. *Geochim. Cosmochim. Acta* **77**, 275–291.

Sai Y., Jin K., Luo M., Tian H., Li J. and Liu J. (2020) Recent progress on the research of Re–Os geochronology and Re–Os elemental and isotopic systematics in petroleum systems. *J. Nat. Gas Geosci.* **5**, 355–365.

Schmincke H.-U., Park C. and Harms E. (1999) Evolution and environmental impacts of the eruption of Laacher See Volcano (Germany) 12,900 a BP. *Quat. Int.* **61**, 61–72.

Schmitz B. and Asaro F. (1996) Iridium geochemistry of volcanic ash layers from the early Eocene rifting of the northeastern North Atlantic and some other Phanerozoic events. *Geol. Soc. Am. Bull.* **108**, 489–504.

Schutter S. R. (2003) Occurrences of hydrocarbons in and around igneous rocks. *Geol. Soc. Lond. Spec. Publ.* **214**, 35–68.

Scott A. C., Pinter N., Collinson M. E., Hardiman M., Anderson R. S., Brain A. P. R., Smith S. Y., Marone F. and Stampanoni M. (2010) Fungus, not comet or catastrophe, accounts for carbonaceous spherules in the Younger Dryas "impact layer." *Geophys. Res. Lett.* **37**.

Selby D. (2005) Direct Radiometric Dating of Hydrocarbon Deposits Using Rhenium-Osmium Isotopes. *Science* **308**, 1293–1295.

Selby D. and Creaser R. A. (2005) Direct radiometric dating of the Devonian-Mississippian time-scale boundary using the Re-Os black shale geochronometer. *Geology* **33**, 545.

Selby D., Creaser R. A. and Fowler M. G. (2007) Re–Os elemental and isotopic systematics in crude oils. *Geochim. Cosmochim. Acta* **71**, 378–386.

Sen I. S. and Peucker-Ehrenbrink B. (2014) Determination of Osmium Concentrations and 187Os/188Os of Crude Oils and Source Rocks by Coupling High-Pressure, High-Temperature Digestion with Sparging OsO_4 into a Multicollector Inductively Coupled Plasma Mass Spectrometer. *Anal. Chem.* **86**, 2982–2988.

Severinghaus J. P., Sowers T., Brook E. J., Alley R. B. and Bender M. L. (1998) Timing of abrupt climate change at the end of the Younger Dryas interval from thermally fractionated gases in polar ice. *Nature* **391**, 141.

Shen J. J., Papanastassiou D. A. and Wasserburg G. J. (1996) Precise Re-Os determinations and systematics of iron meteorites. *Geochim. Cosmochim. Acta* **60**, 2887–2900.

Shiihara M., Torii M., Okuno M., Domitsu H., Nakamura T., Kim K.-H., Moriwaki H. and Oda M. (2011) Revised stratigraphy of Holocene tephras on Ulleung Island, South Korea, and possible correlatives for the U-Oki tephra. *Quat. Int.* **246**, 222–232.

Shirey S. B. and Walker R. J. (1995) Carius Tube Digestion for Low-Blank Rhenium-Osmium Analysis. *Anal. Chem.* **67**, 2136–2141.

Shirey S. B. and Walker R. J. (1998) The Re-Os Isotope System in Cosmochemistry and High-Temperature Geochemistry. *Annu. Rev. Earth Planet. Sci.* **26**, 423–500.

Smirnov S. Z., Rybin A. V., Sokolova E. N., Kuzmin D. V., Degterev A. V. and Timina T. Y. (2017) Felsic magmas of the caldera-forming eruptions on the Iturup Island: the first results of studies of melt inclusions in phenocrysts from pumices of the Lvinaya Past and Vetrovoy Isthmus calderas. *Russ. J. Pac. Geol.* **11**, 46–63.

Smoliar M. I., Walker R. J. and Morgan J. W. (1996) Re-Os Ages of Group IIA, IIIA, IVA, and IVB Iron Meteorites. *Science* **271**, 1099–1102.

Stafford, Jr. T. W., Lundelius E., Kennett J., Kennett D. J., West A. and Wolbach W. S. (2009) Testing Younger Dryas ET Impact (YDB) Evidence at Hall's Cave, Texas. *AGU Fall Meet. Abstr.* **33**, PP33B-08.

Stein H. J., Markey R. J., Morgan J. W., Hannah J. L. and Scherstén A. (2001) The remarkable Re–Os chronometer in molybdenite: how and why it works. *Terra Nova* **13**, 479–486.

Stelling P., Gardner J. E. and Begét J. (2005) Eruptive history of Fisher caldera, Alaska, USA. *J. Volcanol. Geotherm. Res.* **139**, 163–183.

Sun J., Zhang L., Deng C. and Zhu R. (2008) Evidence for enhanced aridity in the Tarim Basin of China since 5.3Ma. *Quat. Sci. Rev.* **27**, 1012–1023.

Sun N., Brandon A. D., Forman S. L., Waters M. R. and Befus K. S. (2020) Volcanic origin for Younger Dryas geochemical anomalies ca. 12,900 cal B.P. *Sci. Adv.* **6**, eaax8587.

Surovell T. A., Holliday V. T., Gingerich J. A. M., Ketron C., Haynes C. V., Hilman I., Wagner D. P., Johnson E. and Claeys P. (2009) An independent evaluation of the Younger Dryas extraterrestrial impact hypothesis. *Proc. Natl. Acad. Sci.* **106**, 18155–18158.

Tagle R. (2005) LL-Ordinary Chondrite Impact on the Moon: Results from the 3.9 Ga Impact Melt at the Landing Site of Apollo 17. *36th Annual Lunar and Planetary Science Conference* **March 2005**.

Tagle R. and Claeys P. (2005) An ordinary chondrite impactor for the Popigai crater, Siberia. *Geochim. Cosmochim. Acta* **69**, 2877–2889.

Tagle R. and Hecht L. (2006) Geochemical identification of projectiles in impact rocks. *Meteorit. Planet. Sci.* **41**, 1721–1735.

Tarasov L. and Peltier W. R. (2005) Arctic freshwater forcing of the Younger Dryas cold reversal. *Nature* **435**, 662–665.

Thordarson T. (2014) The widespread ~10ka Saksunarvatn tephra is not a product single eruption. *AGU Fall Meet. Abstr.* **24**, V24B-04.

Tian W., Campbell I. H., Allen C. M., Guan P., Pan W., Chen M., Yu H. and Zhu W. (2010) The Tarim picrite–basalt–rhyolite suite, a Permian flood basalt from northwest China with contrasting rhyolites produced by fractional crystallization and anatexis. *Contrib. Mineral. Petrol.* **160**, 407–425.

Timmreck C., Graf H.-F. and Feichter J. (1999) Simulation of Mt. Pinatubo Volcanic Aerosol with the Hamburg Climate Model ECHAM4. *Theor. Appl. Climatol.* **62**, 85–108.

Tomlinson E. L., Thordarson T., Lane C. S., Smith V. C., Manning C. J., Müller W. and Menzies M. A. (2012) Petrogenesis of the Sólheimar ignimbrite (Katla, Iceland): Implications for tephrostratigraphy. *Geochim. Cosmochim. Acta* **86**, 318–337.

Toomey R. S. (1993) Late Pleistocene and Holocene faunal and environmental changes at Hall's Cave, Kerr County, Texas. Ph. D. Thesis, The University of Texas at Austin.

Vermeesch P. (2018) IsoplotR: A free and open toolbox for geochronology. *Geosci. Front.* **9**, 1479–1493.

Völkening J., Walczyk T. and G. Heumann K. (1991) Osmium isotope ratio determinations by negative thermal ionization mass spectrometry. *Int. J. Mass Spectrom. Ion Process.* **105**, 147–159.

Walker R. J., Horan M. F., Morgan J. W., Becker H., Grossman J. N. and Rubin A. E. (2002) Comparative ^{187}Re-^{187}Os systematics of chondrites: Implications regarding early solar system processes. *Geochim. Cosmochim. Acta* **66**, 4187–4201.

Walker R. J., McDonough W. F., Honesto J., Chabot N. L., McCoy T. J., Ash R. D. and Bellucci J. J. (2008) Modeling fractional crystallization of group IVB iron meteorites. *Geochim. Cosmochim. Acta* **72**, 2198–2216.

Walker R. J., Morgan J. W., Horan M. F., Czamanske G. K., Krogstad E. J., Fedorenko V. A. and Kunilov V. E. (1994) Re-Os isotopic evidence for an enriched-mantle source for the Noril'sk-type, ore-bearing intrusions, Siberia. *Geochim. Cosmochim. Acta* **58**, 4179–4197.

Wang L., Jiang W. Y., Jiang D. B., Zou Y. F., Liu Y. Y., Zhang E. L., Hao Q. Z., Zhang D. G., Zhang D. T., Peng Z. Y., Xu B., Yang X. D. and Lu H. Y. (2018) Prolonged Heavy Snowfall During the Younger Dryas. *J. Geophys. Res. Atmospheres* **123**, 13,748-13,762.

Wang L., Tian W., Shi Y. and Guan P. (2015) Volcanic structure of the Tarim flood basalt revealed through 3-D seismological imaging. *Sci. Bull.* **60**, 1448–1456.

Wang Q. M., Nishidai T. and Coward M. P. (1992) The Tarim Basin, Nw China: Formation and Aspects of Petroleum Geology. *J. Pet. Geol.* **15**, 5–34.

Wasson J. T. and Kallemeyn G. W. (1988) Compositions of chondrites. *Phil Trans R Soc Lond A* **325**, 535–544.

Waters M. R., Forman S. L., Jennings T. A., Nordt L. C., Driese S. G., Feinberg J. M., Keene J. L., Halligan J., Lindquist A., Pierson J., Hallmark C. T., Collins M. B. and Wiederhold J. E. (2011) The Buttermilk Creek Complex and the Origins of Clovis at the Debra L. Friedkin Site, Texas. *Science* **331**, 1599–1603.

Waters M. R., Keene J. L., Forman S. L., Prewitt E. R., Carlson D. L. and Wiederhold J. E. (2018) Pre-Clovis projectile points at the Debra L. Friedkin site, Texas—Implications for the Late Pleistocene peopling of the Americas. *Sci. Adv.* **4**, eaat4505.

Waters M. R., Stafford T. W. and Carlson D. L. (2020) The age of Clovis—13,050 to 12,750 cal yr B.P. *Sci. Adv.* **6**, eaaz0455.

Waters M. and Stafford T. (2014) The First Americans: A Review of the Evidence for the Late-Pleistocene Peopling of the Americas. In pp. 541–560.

Watson E. J., Swindles G. T., Stevenson J. A., Savov I. and Lawson I. T. (2016) The transport of Icelandic volcanic ash: Insights from northern European cryptotephra records. *J. Geophys. Res. Solid Earth* **121**, 7177–7192.

White W. M. (2007) Chapter 8: Radiogenic Isotope Geochemistry. , 313–360.

Wittke J. H., Weaver J. C., Bunch T. E., Kennett J. P., Kennett D. J., Moore A. M. T., Hillman G. C., Tankersley K. B., Goodyear A. C., Moore C. R., Daniel I. R., Ray J. H., Lopinot N. H., Ferraro D., Israde-Alcántara I., Bischoff J. L., DeCarli P. S., Hermes R. E., Kloosterman J. B., Revay Z., Howard G. A., Kimbel D. R., Kletetschka G., Nabelek L., Lipo C. P., Sakai S., West A. and Firestone R. B. (2013) Evidence for deposition of 10 million tonnes of impact spherules across four continents 12,800 y ago. *Proc. Natl. Acad. Sci.* **110**, E2088–E2097.

Wong C. I., Banner J. L. and Musgrove M. (2015) Holocene climate variability in Texas, USA: An integration of existing paleoclimate data and modeling with a new, high-resolution speleothem record. *Quat. Sci. Rev.* **127**, 155–173.

Woodland S. J., Pearson D. G. and Thirlwall M. F. (2002) A Platinum Group Element and Re–Os Isotope Investigation of Siderophile Element Recycling in Subduction Zones: Comparison of Grenada, Lesser Antilles Arc, and the Izu–Bonin Arc. *J. Petrol.* **43**, 171–198.

Wu J., Li Z. and Wang X. (2016) Comment on "Behavior of Re and Os during contact between an aqueous solution and oil: Consequences for the application of the Re–Os geochronometer to petroleum" [Geochim. Cosmochim. Acta 158 (2015) 1–21]. *Geochim. Cosmochim. Acta* **186**, 344–347.

Wu N., Cai Z., Yang H., Wang Z., Liu X. and Han J. (2013) Hydrocarbon charging of the Ordovician reservoirs in Tahe-Lunnan area, China. *Sci. China Earth Sci.* **56**, 763–772.

Wu Y., Sharma M., LeCompte M. A., Demitroff M. N. and Landis J. D. (2013) Origin and provenance of spherules and magnetic grains at the Younger Dryas boundary. *Proc. Natl. Acad. Sci.* **110**, E3557–E3566.

Xia L., Xu X., Li X., Ma Z. and Xia Z. (2012) Reassessment of petrogenesis of Carboniferous–Early Permian rift-related volcanic rocks in the Chinese Tianshan and its neighboring areas. *Geosci. Front.* **3**, 445–471.

Xiao Z. Y., Lu Y. H., Sang H., Pan Z. Z. and Li Y. F. (2005) A typical Cambrian oil reservoir: origin of oil reservoir in Well TZ62, Tarim Basin. *Geochimica* **34**, 155–160.

Xu G., Hannah J. L., Stein H. J., Bingen B., Yang G., Zimmerman A., Weitschat W., Mørk A. and Weiss H. M. (2009) Re–Os geochronology of Arctic black shales to evaluate the Anisian–Ladinian boundary and global faunal correlations. *Earth Planet. Sci. Lett.* **288**, 581–587.

Xu Y.-G., Wei X., Luo Z.-Y., Liu H.-Q. and Cao J. (2014) The Early Permian Tarim Large Igneous Province: Main characteristics and a plume incubation model. *Lithos* **204**, 20–35.

Yamashita Y., Takahashi Y., Haba H., Enomoto S. and Shimizu H. (2007) Comparison of reductive accumulation of Re and Os in seawater–sediment systems. *Geochim. Cosmochim. Acta* **71**, 3458–3475.

Yang A. Y., Zhou M.-F., Zhao T.-P., Deng X.-G., Qi L. and Xu J.-F. (2014) Chalcophile elemental compositions of MORBs from the ultraslow-spreading Southwest Indian Ridge and controls of lithospheric structure on S-saturated differentiation. *Chem. Geol.* **382**, 1–13.

Yang S.-F., Li Z., Chen H., Santosh M., Dong C.-W. and Yu X. (2007) Permian bimodal dyke of Tarim Basin, NW China: Geochemical characteristics and tectonic implications. *Gondwana Res.* **12**, 113–120.

York D., Evensen N. M., Martínez M. L. and De Basabe Delgado J. (2004) Unified equations for the slope, intercept, and standard errors of the best straight line. *Am. J. Phys.* **72**, 367–375.

Yu B., Dong H., E. W., Cheng J. and Lin C. (2004) Re-Os and Nd isotopes of black shales at the bottom of the Lower Cambrian from the northern Tarim Platform and their comparison with those from the Yangtze Platform. *Sci. China Ser. -Earth Sci.* **47**, 47–97.

Yu B., Dong H., Widom E., Chen J. and Lin C. (2009) Geochemistry of basal Cambrian black shales and cherts from the Northern Tarim Basin, Northwest China: Implications for depositional setting and tectonic history. *J. Asian Earth Sci.* **34**, 418–436.

Yu S., Pan C., Wang J., Jin X., Jiang L., Liu D., Lü X., Qin J., Qian Y., Ding Y. and Chen H. (2012) Correlation of crude oils and oil components from reservoirs and source rocks using carbon isotopic compositions of individual n-alkanes in the Tazhong and Tabei Uplift of the Tarim Basin, China. *Org. Geochem.* **52**, 67–80.

Yu X., Yang S.-F., Chen H.-L., Chen Z.-Q., Li Z.-L., Batt G. E. and Li Y.-Q. (2011) Permian flood basalts from the Tarim Basin, Northwest China: SHRIMP zircon U–Pb dating and geochemical characteristics. *Gondwana Res.* **20**, 485–497.

Yudovskaya M. A., Tessalina S., Distler V. V., Chaplygin I. V., Chugaev A. V. and Dikov Y. P. (2008) Behavior of highly-siderophile elements during magma degassing: A case study at the Kudryavy volcano. *Chem. Geol.* **248**, 318–341.

Zelenski M. E., Fischer T. P., de Moor J. M., Marty B., Zimmermann L., Ayalew D., Nekrasov A. N. and Karandashev V. K. (2013) Trace elements in the gas emissions from the Erta Ale volcano, Afar, Ethiopia. *Chem. Geol.* **357**, 95–116.

Zhan Z.-W., Tian Y., Zou Y.-R., Liao Z. and Peng P. (2016) De-convoluting crude oil mixtures from Palaeozoic reservoirs in the Tabei Uplift, Tarim Basin, China. *Org. Geochem.* **97**, 78–94.

Zhang D., Zhang Z., Huang H., Encarnación J., Zhou N. and Ding X. (2014) Platinum-group elemental and Re–Os isotopic geochemistry of the Wajilitag and Puchang Fe–Ti–V oxide deposits, northwestern Tarim Large Igneous Province. *Ore Geol. Rev.* **57**, 589–601.

Zhang Z., Zhi X., Chen L., Saunders A. D. and Reichow M. K. (2008) Re–Os isotopic compositions of picrites from the Emeishan flood basalt province, China. *Earth Planet. Sci. Lett.* **276**, 30–39.

Zhu G., Zhang S., Su J., Huang H., Yang H., Gu L., Zhang B. and Zhu Y. (2012) The occurrence of ultra-deep heavy oils in the Tabei Uplift of the Tarim Basin, NW China. *Org. Geochem.* **52**, 88–102.

Zhu G., Zhang S., Su J., Zhang B., Yang H., Zhu Y. and Gu L. (2013) Alteration and multi-stage accumulation of oil and gas in the Ordovician of the Tabei Uplift, Tarim Basin, NW China: Implications for genetic origin of the diverse hydrocarbons. *Mar. Pet. Geol.* **46**, 234–250.

Zhu X., Chen J., Wu J., Wang Y., Zhang B., Zhang K. and He L. (2017) Carbon isotopic compositions and origin of Paleozoic crude oil in the platform region of Tarim Basin, NW China. *Pet. Explor. Dev.* **44**, 1053–1060.